SYNTHESIS, CHARACTERIZATION AND APPLICATION OF HETERO ATOM DOPED MESOPOROUS TiO_2

A THESIS SUBMITTED TO THE
UNIVERSITY OF PUNE
FOR THE DEGREE OF
DOCTOR OF PHILOSOPHY
IN CHEMISTRY

BY
K. SIVARANJANI

CATALYSIS DIVISION
NATIONAL CHEMICAL LABORATORY
PUNE 411 008
INDIA

Dr. CHINNAKONDA S. GOPINATH
(RESEARCH GUIDE)
October 2012

DECLARATION BY RESEARCH SCHOLAR

I hereby declare that the thesis “**Synthesis, Characterization and Application of Hetero Atom Doped Mesoporous TiO_2”** submitted for the degree of Doctor of Philosophy to the University of Pune has been carried out by me at the Catalysis and Inorganic Chemistry Division, National Chemical Laboratory, Pune – 411 008, India, under the supervision of Dr. Chinnakonda S. Gopinath. Such material as has been obtained by other sources has been duly acknowledged in this thesis. I declare that the present work or any part thereof has not been submitted to any other University for the award of any other degree or diploma.

Date: October 01, 2012 **K. Sivaranjani**

Catalysis Division,
National Chemical Laboratory,
Pune 411 008,
Maharashtra,
India

CERTIFICATE BY RESEARCH GUIDE

This is to certify that the work incorporated in the thesis entitled, “**Synthesis, Characterization and Application of Hetero Atom Doped Mesoporous TiO_2”** submitted by **K. Sivaranjani,** for the Degree of **Doctor of Philosophy,** was carried out by the candidate under my supervision in the Catalysis Division, National Chemical Laboratory, Pune – 411 008, India. Such material as has been obtained from other sources has been duly acknowledged in the thesis. To the best of my knowledge, the present work or any part thereof has not been submitted to any other University for the award of any other degree or diploma.

Date: October 01, 2012
Catalysis Division
National Chemical Laboratory,
Pune 411 008,
Maharashtra,
India

Dr. C. S. Gopinath
(Research Supervisor)

Dedicated to my
beloved Family and my
lovely Husband

Acknowledgement

It is my great pleasure to acknowledge my research supervisor Dr. C. S. Gopinath who introduced me to a fascinating realm of chemistry. I am deeply indebted to him for his invaluable guidance and unconditional support. His constant inspiration and constructive criticism helped me a lot to focus my views in proper perspective. His tireless attitude has been an impetus for me throughout the course of study. He gave me the freedom to think, and work; and I shall cherish my learning experience under his guidance. I take this opportunity to express my deepest sense of gratitude and reverence towards him for guiding me in the right direction throughout the course of this work.

My honest thanks go to Dr. S. Sivaram and Dr. Sourav Pal, erstwhile and current Directors, NCL, providing me the opportunity to accomplish my research work in this prestigious and well-equipped laboratory. I would like to thank Dr A.P.Singh Head, catalysis division, for providing me all the divisional facilities required for my research work. A special note of thanks to Dr. Srinivas, Dr. Satyanarayana, Dr. Raja, Dr. Vinod, Dr. Nandini Devi, Ms. Violet Samuel, Mr. Jha, Mr. Gaikwad, and Mrs. Rupali Waichal for their help and support in scientific and technical matters. I'm grateful to Dr. S.B. Ogale and Dr. Sreekumar for their keen interest and collaboration.

It gives me great pleasure to thank my labmates Dr. Maitri, Dr. Nagaraj, Edwin, Rajambal, Kanak, Thushara, Sanjay, Devaraj, Anjani, Khiru, Pradnya, Dr. Naveen, Jino, Lakshmi, Akrati, Amit, Sanjini, Anju for their helpful hand and making the lab feel like a family. Without their support it would not have been possible to complete this task. PhD life is difficult without friends and I would like to thank all my divisional friends Ashok, Rajesh, Hanumant, Soumya, Jijil, Shruti, Mandakini, Sreekuttan, Sreedhala, Vyshak, Sunil, Vaibhav, Jitendra, Anuj, Nishita for their co-operation, invaluable help and moral support. With much appreciation, I would like to admire all of my tamil friends in NCL and outside; for their kind support during my difficult times and it is not just possible to acknowledge all of them in few words for their timely and invaluable help throughout my life.

I have no words to thank my parents and my brother (Babu) for their love and affection. It gives me great pleasure to thank them for their love, moral support, blessings, care and constant encouragement that they have shown to me. I am very much indebted to them.

A very special appreciation is due to my lovely husband "Senthil" (my M.Sc classmate) not only for his constant encouragement but also for his endless care, *unconditional love and understanding throughout. I wouldn't have overcome all the hurdles to achieve any goal without his care and love. He is the one who is the backbone of my achievement. These few words are only a small fraction of my enormous sense of love, appreciation and thanks.*

I would like to express my heartiest thanks to Mrs. C. G. Jothimoni, Karthik and Ishwarya for their kindness and affection and for never letting me feel that I am away from my home.

Finally, my thanks are due to CSIR, Government of India, for awarding me the research fellowship. At last I like to express my gratitude to god almighty for his grace.

Pune ***Sivaranjani***
October 2012

Table of contents

Chapter 1: Introduction

Chapter 2: Experimental Methods

Chapter 3: Characterization and Application of $TiO_{2-x}N_x$ in Photocatalysis and DSSC

Part A: Characterization of $TiO_{2-x}N_x$

Part B: Photocatalytic and Photovoltaic applications of $TiO_{2-x}N_x$

Chapter 4: Characterization and Application of nano Au/$TiO_{2-x}N_x$ composites in Solar H_2 Generation

Chapter 5: Characterization and Application of $Ti_{1-x}V_xO_2$ in Oxidative Dehydrogenation of Ethylbenze to Styrene

Chapter 6: Conclusions and Future Outlook

List of Publications

Abbreviations

BE	Binding Energy

BET	Braunauer-Emmett-Teller
BJH	Barrett–Joyner–Halenda
CB	Conduction Band
CVD	Chemical Vapor Deposition
CS	Combustion Synthesis
DSSC	Dye Sensitized Solar Cell
EB	Ethylbenzene
EDAX	Energy Dispersive Analysis of X-rays
EINP	Electrically interconnected nanoparticles
EIS	Electrochemical impedance spectroscopy
FF	Fill factor
GC	Gas Chromatography
LUMO	Lowest Unoccupied Molecular Orbital
MOCVD	Metal Organic Chemical Vapor Deposition
NP	Nanoparticles
ODH	Oxidative Dehydrogenation
PLD	Pulsed Laser Deposition
PL	Photoluminescence
SEM	Scanning Electron Microscopy
SCM	Solution Combustion Method
SC	Semiconductor
SHS	Selfpropagating Hightemperature Synthesis
TG	Thermo Gravimetry
TEM	Transmission Electron Microscopy
VB	Valence Band
WSR	Water Splitting reactions
WHSV	Weight Hour Space Velocity
XRF	X-ray Fluorescence
PXRD	Powder X-ray Diffraction
XPS	X-ray Photoelectron Spectroscopy

Chapter 1

Introduction

1. Introduction

1.1. Heterogeneous catalysis

Modern chemical technology is wholly based on heterogeneous catalysis. Heterogeneous catalyst can either be metal (noble/non-noble/transition), semiconductor or metal oxides which may be crystalline or amorphous in nature. Each type has its own merits and demerits to specific application. Numerous chemical reactions are facilitated by catalysts. The study of heterogeneous catalysis dates back to the early 1800s. Faraday was one of the first to examine the ability of platinum to facilitate oxidation reactions. Many other catalytic processes were subsequently developed that facilitated hydrogenation, dehydrogenation, isomerization, and polymerization reactions. All these catalytic reactions played a key role in the development of the industrial revolution. [1] Sulfuric acid synthesis (Contact process), ammonia synthesis (Haber-Bosch process), nitric acid synthesis (Ostwald process), hydrogen production by steam reforming, ethylene oxide synthesis, hydrogen cyanide synthesis (Andrussov oxidation), olefin polymerization (Ziegler-Natta polymerization), desulfurization of petroleum (hydrodesulfurization) are some of the important industrial process. [2]

In this century it is very difficult to imagine our world without the fruits of heterogeneous catalysis. Unfortunately industrial developments further leads to serious environmental pollution. Catalysis is a key technology [3] to achieve the objectives of sustainable (green) chemistry, but an innovative effort is necessary in the design of new catalysts and catalytic technologies (including reactor engineering) and also in reconsidering all chemical production processes with the objective of developing small and delocalized plants for on-site production.

1.2. Titanium dioxide (TiO_2)

Metal oxides are one of the important classes of materials used in the field of catalysis. Among all metal oxides, transition metal oxides are commonly used as catalysts or catalytic supports in heterogeneous catalysis because of their interesting acid–base and redox properties. [4] The unique property of transition metals arises mainly due to its vacant d orbitals. [5] Among all transition metal oxides, titanium dioxide plays one of the most prominent roles due to its promising electrochemical properties, high chemical stability and being commercially available and non-toxic nature. Due to its high refractive index, it has been extensively used in a variety of applications, such as white pigment in paints, cosmetics and toothpastes. [6] Recently the role of titania in the field of photocatalysis, photovoltaics and more recently as electrode material in lithium ion batteries is innumerable.

1.3. Structure of Titania

Titanium dioxide has three different crystal structures: rutile, anatase, and brookite. In all three structures there are three titanium atoms present around each oxygen atom and six oxygen atoms are there around each titanium atom. [7]

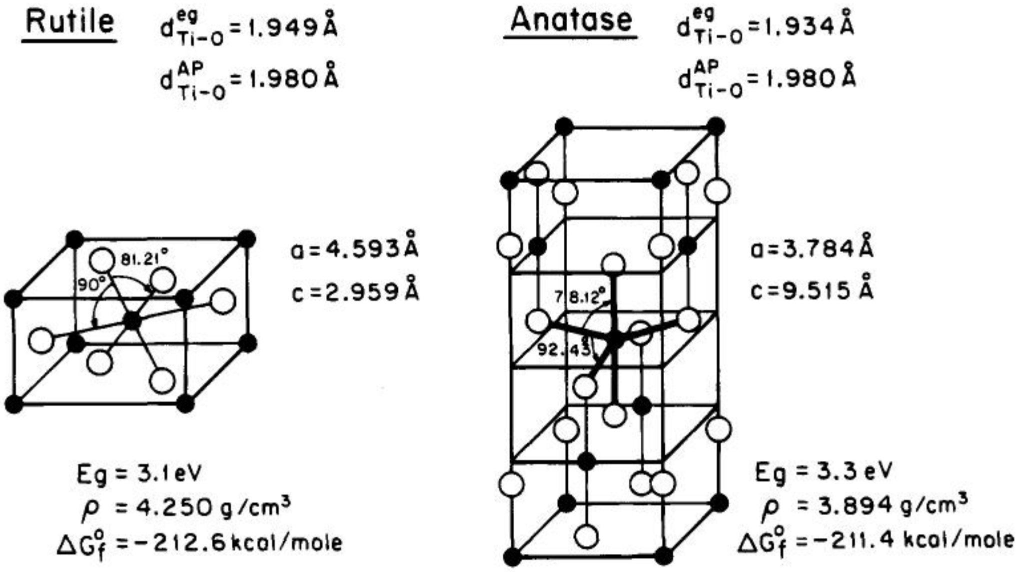

Figure 1: Unit cell structure of (a) Rutile (b) Anatase TiO_2

The oxygen atoms around each titanium atom form a distorted octahedron. The distortion is maximum in brookite, the least stable and least common crystal structure. The structure of rutile and anatase can be described in terms of chains of TiO_6 octahedra. The two crystal structures differ by the distortion of each octahedron and by the assembly pattern of the octahedra chains. Figure 1 shows the unit cell structures of the rutile and anatase crystals. [8] Each Ti^{4+} ion is surrounded by an octahedron of six O^{2-} ions. The octahedron in rutile is not regular, showing a slight orthorhombic distortion. The octahedron in anatase is significantly distorted so that its symmetry is lower than orthorhombic. The Ti-Ti distances in anatase are greater (3.79 and 3.04 Å vs 3.57 and 2.96 Å in rutile) whereas the Ti-O distances are shorter than in rutile (1.934 and 1.980 Å in anatase vs 1.949 and 1.980 A in rutile). [9] In the rutile structure each octahedron is in contact with 10 neighbour octahedrons (two sharing edge oxygen pairs and eight sharing corner oxygen atoms) while in the anatase structure each octahedron is in contact with eight neighbors (four sharing an edge and four sharing a corner). These differences in lattice structures cause different mass densities and electronic band structures between the two forms of TiO_2.

1.4. Principles of Photocatalysis

Photocatalysis is nothing but the reaction assisted by photons with a catalyst. A material which can be capable of promoting both oxidation and reduction reactions can act as photocatalyst. Typical photocatalytic process can be divided into three types; (i) Photodecomposition of water (ii) Photocatalytic formation of organic compounds and (iii) Photocatalysis in pollution abatement. Among all available materials, semiconductors are suitable materials to act as a photocatalyst. Irradiation of the catalyst with sufficient energy of photons (which should be equal or greater than the band gap energy) will excite electrons from the filled valence band (VB) to the empty conduction band (CB). In the next step, the charge carriers produced should diffuse to the surface without recombination. Further this photo induced electrons will transfer to the pre adsorbed organic or inorganic species and reduce that species. The electron transfer process is more efficient if the species are pre adsorbed on the surface. [10] Hence at the surface, the semiconductor can donate electrons to reduce an electron acceptor (usually oxygen in an aerated solution) in turn holes will migrate to the surface where an electron from a donor species (usually from water molecules or from alcohol) can combine with the surface hole oxidizing the donor species. The rate of the charge transfer processes for electrons and holes depends upon the respective positions of the band edges for the conduction and valence bands and the redox potential levels of the adsorbate species. Electron and hole recombination is detrimental to the efficiency of a semiconductor photocatalyst. Modifications to semiconductor surfaces such as addition of metals, dopants, or combinations with other semiconductors are beneficial in decreasing the electron and hole recombination rate and thereby increasing the quantum yield of the photocatalytic process. [8]

1.5. Doping in Titania

Titania is one of the most studied semiconductor materials for photocatalysis and it is accepted to be the best due to its chemical stability towards photocorrosion and holes produced by photons in titania have high oxidizing ability. The effective photocatalytic activity of titania was first discovered by Honda-Fujishima in 1972. [11] They had successfully demonstrated the photoinduced decomposition of water on TiO_2 electrodes. After that report, there has been increasing interest in environmental applications such as self cleaning of tiles, glasses, and windows. Titanium dioxide represents an effective photocatalyst for water and air purification and for self-cleaning surfaces. Additionally, it can be used as antibacterial agent because of strong oxidation activity and super hydrophilicity. [12] However; the major limitation is that, it is not active in visible light. Through doping with anions and/or cations, the electronic property of titania can be modified, and visible light absorption could be introduced. In order to get more active visible light photocatalyst, doping should satisfy the following conditions, (1) Doping ion should produce electronic states near to the VB or CB level of TiO_2 which leads to band gap reduction and hence visible light absorption. (2) The CB minimum (CBM) including impurity states should be as high as that of TiO_2 or at more negative potential than the H_2/H_2O level to ensure its photoreduction activity. (3) The acceptor/donor states in the bandgap should overlap sufficiently with the band states of TiO_2 to transfer photoexcited carriers to reactive sites at the catalyst surface within their life time. [13] The photocatalytic activity of doped TiO_2 appears to be a complex function of the dopant concentration, the energy level of dopants within the TiO_2 lattice, doped metal ions d-electronic configurations and their oxidation states, the type of defects (substitutional or interstitial) in the host lattice and the lifetime of charge carriers. [14]

1.5.1. Cation doping

Metal ion doping in TiO_2 produces localized energy levels in the forbidden gap (between CB and VB) of TiO_2. The electron transfer from these new energy levels to CB allows TiO_2 to absorb visible light photons.

In 1994 Choi et al,[15] reported the photocatalytic activity of 21 different metal ions doped quantum sized TiO_2 for the oxidation of $CHCl_3$ as well as for the reduction of CCl_4. It is interesting to note that all the dopants with d^5 (Fe^{3+}, Ru^{3+}, and Os^{3+}) and d^1 electronic configurations (V^{4+} and Mo^{5+}) enhanced the photoreactivity of TiO_2 for both oxidation and reduction.

In 2000, Anpo et al reported the second generation titanium oxide photocatalysts (visible light active TiO_2) prepared by an advanced high-voltage metal ion-implantation method. [16] The metal ions can be incorporated into TiO_2 by bombarding the TiO_2 substrate with high energy metal ions. High acceleration energy (150 – 200 keV) was applied in order to incorporate the metal ions (especially Cr and V ions) into the deep bulk of the TiO_2, and then calcined in oxygen at 450-475°C. These photocatalysts worked effectively for the decomposition of NO into N_2 and O_2 under visible light ($\lambda > 450$ nm). [17] The same method was successfully used to dope a series of transition metals, such as V, Cr, Ni, Mn and Fe. [18]

A series of vanadium-doped TiO_2 photocatalysts were prepared through modified sol-gel methods by Wu et al. [19] In this method, anatase phase of titania was maintained after calcination at 400^0C. Obtained vanadium-doped TiO_2 shows a red-shift in the UV-vis spectra and the presence of V^{4+} instead of V^{5+} was proved by XAS (X-ray absorption spectroscopy) analysis. This V-doped TiO_2 material shows higher activity in the photodegradation of dyes under visible light than pure TiO_2.

In 2004, Hegde [20] et al prepared series of different metal ions (W, V, Ce, Zr, Fe and Cu ions) doped nanocrystalline titania by simple solution combustion method using glycine as a fuel. The structural studies indicate that the solid solution formation was limited to a narrow range of concentrations of the dopant ions. The degradation rate of 4-nitrophenol with these metal doped titania catalysts were lesser than pure titania under both UV and solar light exposure. This decrease in the activity is mainly due to the mid gap states formed by the doped metal ions which are acting as a recombination centre for photo generated charge carriers.

In 2008, Tyagi et al [21] synthesized anatase titania with up to 10 mol % vanadium doping by sol-gel route. They evaluate photocatalytic behavior of these catalysts by the photo-oxidation of ethylene using sunlight-type excitation. Vanadium doping led to a red shift in the UV-visible absorbance spectra compared to pristine titania, thus enhancing the absorption in the visible region. Among all 5 mol % V doped TiO_2 shows excellent activity for the photo oxidation.

Though cation doping gives visible light absorption to the pristine titania, there are some limitations are also associated with cation doping. Mainly thermal stability is very low for metal ion doped TiO_2, charge carrier recombination centers are getting increased due to the metal ion doping, moreover metal ion doping mostly requires expensive ion-implantation facility. Due to the above reasons anion doping serves better than cation doping.

1.5.2. Anion doping

Unlike metal ions, energy state of doped non-metal ion (anions) hybridize well with the VB states of the semiconductor oxide material, and either shift the VB upward or broaden the VB thus reducing the overall band gap. [22] Anion doping with either of the following N^{3-}, C^{4-}, and S^{2-}, is one of the methods to reduce the band gap and bring absorption into the visible light regime. Among all, nitrogen doping gives promising results because 2p states of N will sufficiently overlap with the O 2p states which reduce the band gap effectively. S doping shows similar band gap narrowing, but due to its large ionic radius it is very difficult to incorporate S in TiO_2 lattice. C and P doping gives states deep in the band gap which will act as recombination centers. [13] Hence among the anions N^{3-} found to be the best candidate to make titania into visible light active photocatalyst.

Accidentally, nitric oxide (NO) type species doped titania was prepared by Sato [23] in 1986 with visible light absorption. They calcined the commercially available $Ti(OH)_4$ at 400^0C which results in yellow powder. This yellow coloration is mainly attributed to the presence of small amount of NH_4Cl present in the commercial powder which further oxidized to NO_x at temperatures above 300^0C. This volatile impurity NO_x acts as dopant and brings visible light absorption.

In 2001, Asahi et al [13] prepared nitrogen doped titania films by sputtering titania targets using a N_2/Ar gas mixture followed by annealing at 550^0C in N_2 gas for 4h. Resulting

N doped TiO_2 film has visible light absorption upto 500 nm. This N doped TiO_2 shows better activity than pure TiO_2 for methylene blue decomposition at different cut off wavelengths. Through XPS they have demonstrated that the nitride type of nitrogen (substituted nitrogen) is responsible for the band gap reduction and visible light absorption.

N-doped TiO_2 was also prepared through a wet chemical method by Sathish et al [24, 25]. Indeed a band gap reduction to an extent of 0.13 eV was also demonstrated. Here authors proved that the band gap reduction is mainly due to the sustitutional doping of N in titania latttice which gives promissing route to prepare visible light active photocatalyst. Moreover the presence of N-Ti-O linkage is proved by XPS results.

In 2009, Liu et al [26] prepared homogeneous nitrogen doped layered titanates and showed its high photocatalytic activity for the degradation of rhodamine G dye. Commonly N doping in crystalline materials ends up with inhomogeneous doping which gives limited visible light absorption with more recombination centers. In this work, layered structure facillitates nitridation process which leads to the preparation of homogeneous nitrogen doped layered titania materias. Reduction in the band gap due to N doping is proved by both UV-vis and valence band spectroscopy.

In 2007 Kisch et al [27] prepared low-band gap nitrogen doped titania photocatalyst by calcining titanium hydroxide and urea at 400°C. Unlike previously known nitrogen-doped titania (which exhibits a strong band-to-band absorption in the ultraviolet and only a weak shoulder in the visible), these new materials shows an intense band-to-band absorption in the range of 400-500 nm. The superior visible-light activity of these new photocatalysts is demonstrated by their ability to induce the mineralization of hydroquinone, trichloroethylene, and formic acid. Air pollutants like acetaldehyde, benzene, and carbon monoxide are also degraded. Unmodified titania exhibited only a very low activity under identical experimental conditions.

1.6. Importance of nano composites with metal nanostructures

Generally in TiO_2 based photocatalysis, recombination is the major limitation. So in order to improve the photocatalytic activity, the recombination of charge carriers should be restricted. For this purpose, the excited electrons in the CB of TiO_2 must be separated spatially from the holes in the VB. A very promising approach is incorporation of noble metal nanoparticles (NPs) with large work function (i.e., high electronegativity) on TiO_2 which enhances the charge separation due to the interfacial electron transfer from semiconductors to metals. [28] Interestingly nano Au or Ag deposition on titania brings more visible light absorption through surface plasmon resonance (SPR) which is caused by the collective oscillation of free conductive electrons induced by the electric field of the incident light. [29] The resonating frequency is different for different metals according to their electronic structure. For example, gold, silver and copper nanostructures exhibit resonance in visible region, where Pb, In, Hg, Sn and Cd exhibit resonance in UV region.[30] The resonating wavelength and SPR intensity strongly depends on the size and shape of nanoparticles, and composition. These noble metal clusters on titania acts as an electron sink by selectively storing electrons thus reducing the recombination probability.

1.6.1. Composite with Nano gold

Haruta et al [31] prepared Au/TiO_2 and Pt/TiO_2 photocatalysts by using TiO_2 powders in aqueous suspensions containing $HAuCl_4.4H_2O$ or $H_2PtCl_6.6H_2O$ by deposition-precipitation (DP), impregnation (IMP), photodeposition (FD) and, in the case of Au, by mixing TiO_2 with colloidal gold suspensions (MIX) and showed its photocatalytic activity towards H_2 generation from aqueous ethanol solution. They found out that the activity of Au/TiO_2 catalysts strongly depend on the method of preparation and decreased in the order

Au-TiO_2-FD>Au-TiO_2-DP>Au-TiO_2-IMP> Au-TiO_2-MIX. The activities of the platinum samples were less sensitive to the preparation method and decreased in the order Pt-TiO_2-FD > Pt-TiO_2-DP~ Pt-TiO_2 -IMP.

Recently Idriss et al [32] has studied the role of the noble metal particle size and the TiO_2 polymorph on photocatalytic hydrogen generation reaction using ethanol as sacrificial agent and he proved that the photocatalytic activity is independent of the gold cluster size between 3 and 12 nm, and Au/anatase gives two orders of magnitude higher rate of H_2 production than on rutile titania.

In 2003, Kamat et al [33] demonstrated improved charge separation in semiconductor-metal systems through Fermi level calculation. TiO_2 nanoparticles exhibit blue coloration due to UV irradiation because of the storage of electrons within the particles and upon contact with gold nanoparticles, there is partial disappearance of the blue color. This disappearance is mainly due to the transfer of stored electrons from TiO_2 to Au nanoparticles. The charge distribution between the semiconductor and metal nanoparticles causes the Fermi level to shift to more negative potentials. They employed C_{60}/C_{60}^- as a probe-redox couple, to calculate the apparent Fermi levels of TiO_2 and Au/TiO_2 nanoparticles. A Fermi level shift of -22 meV observed for the Au-TiO_2 nanocomposite is indicative of improved charge separation in semiconductor-metal systems and this charge separation is useful for improving the efficiency of photocatalyst.

Subramanian et al has demonstrated [34] higher negative potential shift has been observed with E_F of Au-TiO_2 with decreasing gold particle size. Hence the resulting composite materials are more reductive than the pure TiO_2 and enhance the photocatalytic activity. Li et al prepared the mesoporous Au/TiO_2 nanocomposites using P123 as a template and demonstrated its high photocatalytic activity towards phenol degradation under visible light. [35]

Recently Chen et al, studied the rate enhancement of hydrogen generation due to the SPR of gold nano particles. [36] Theoretical calculations by Graciani et al, have shown that the Au preadsorption on TiO_2 surfaces significantly increases the amount of doped N in the oxide. [37] They also demonstrated that the Au/TiN_xO_{2-y} system was more active for the dissociation of water than TiO_2, Au/TiO_2, or TiO_{2-y}. In 2010, Alvaro et al [38] synthesised mesoporous Au/TiO_2 catalysts by one step sol gel method and showed its visible light photocatalytic activity for the decontamination of the chemical warfare agent Soman.

Wu et al [39] prepared Au/N-TiO_2 by hydrolysis of titanium sulphate and ammonia followed by Au deposition-precipitation method. The photocatalytic activities of the catalysts were evaluated for degradation of methyl orange (MO) under visible light and UV light irradiation. It was found that the Au/N-TiO_2 catalyst shows much higher photocatalytic activity than N-doped TiO_2 under both UV and visible light irradiation. They proved the decrease in the charge-carrier recombination probability after gold deposition on N-TiO_2 through photoluminescence (PL) spectra which increases the photocatalytic activity significantly. Inspite of above reports, the mechanistic aspects of Au/TiO_2 system is less understood, especailly about the key aspect of integration of nano Au with titania has been addressed by very few. [33, 34]

1.7. Role of Mesoporosity

Recently, porous materials received significant attention from photocatalysis researchers. These porous materials have many advantages to be used as catalytic material, such as high surface area, less diffusional barriers for reactants and products etc. High surface area will result in more number of reactive sites as well as it helps us to harvest maximum light energy. Though charge carriers can be formed at the bulk of the semiconductor they recombine readily since the distance from the bulk to the reaction centre is greater than the electron diffusion length. Rate of recombination of charge carriers is significantly reduced with porous materials. It is mainly due to the fast diffusion of charge carriers to the surface. Mesoporous titania with visible light absorption is expected to show wide application as a highly efficient photocatalyst. [40] Generally, ordered mesoporous TiO_2 is prepared by a surfactant templated route, [41,42] and final materials obtained after calcinations around 450^0C which leads to big particles with very long diffusion lengths for charge carriers. In general, ordered mesoporous materials show high surface area and the majority of active sites are present on the surface of porous channels. Hence the reactants have to diffuse further in order to interact with these active sites. However, in contrast to the above, disordered wormhole mesoporous materials [43, 44] exhibit smaller diffusion lengths due to the pseudo-three-dimensional (*p*3D) nature of the pores compared to regular mesopores aiding rapid transport of photogenerated electrons to the anode surface. [45] This is because of the smaller mesochannel depth (<5-10 nm) and the nature of the electrically interconnected nanoparticles (EINP). These may aptly be called *pseudo* three-dimensional (p3D) materials. Also the reactants and products can easily diffuse in/outof the active sites, which increases the selectivity and yield of the desired product and hence the rate of the reaction.

Mesoporous Nb_2O_5, synthesized via an evaporation-induced self-assembly method, demonstrated a photocatalytic activity 20 times higher for hydrogen evolution than a bulk Nb_2O_5 without any porosity. [46] Noda et al. demonstrated that the high photocatalytic activity of crystallized mesoporous Ta_2O_5, for overall water splitting. They attributed that the activity is mainly due to the efficient transfer of the excited electrons and holes from bulk to the surface through the thin-walled crystalline phase. [47]

1.8. Preparation of doped Titania

Various methods are available for the preparation of TiO_2-based photocatalysts, such as ion-assisted sputtering, plasma, ion-implantation, chemical vapour deposition (CVD), co precipitation, sol-gel, combustion method and hydrothermal methods are some of the important methods adopted to prepare visible light active TiO_2 based photocatalysts.

1.8.1. Co precipitation

Co-precipitation method is one of the successful techniques for synthesizing ultrafine ceramic powders having narrow particle size distribution. This method offers some advantages such as (i) Simple and rapid preparation (ii) Easy control of particle size, morphology and composition. (iii) Various possibilities to modify the particle surface state and overall homogeneity.[48] This method is more advantageous than wet chemical techniques such as sol-gel, hydrothermal and colloid emulsions which are time consuming and involve highly unstable alkoxides and difficult to maintain reaction conditions.

1.8.2. Sol-gel method

Sol–gel technology has been in existence as from as long ago as the mid-1800s, and was used almost a century later by Schott Glass Company (Jena, Germany). [49] The method is a homogeneous process which results in a continuous transformation of solution into a hydrated solid precursor (hydrogel). The method is based on the hydrolysis and gelation (for instance by controlled addition of water) of alkoxides or other reactive compounds in alcoholic solution. Synthesis of nanosize crystallized powder of high purity at relatively low temperature, possibility of stoichiometry controlling process, preparation of composite materials, and production of homogeneous materials are some of advantages related with sol gel method of preparation. [50] These advantages have driven many researchers to the use sol gel method for the preparation of TiO_2-based photocatalysts.

1.8.3. Hydrothermal synthesis

Hydrothermal synthesis involves the chemical reaction of materials in aqueous solution heated (usually above boiling point) in a sealed vessel. This method is very useful to prepare various metal oxides in nano sizes, layered materials and many other carbon based nano structures especially nano tubes, nano ribbons etc. There is no need for post-heat treatment for hydrothermal synthesis which further reduces the aggregation and results in nanoparticles. Controllable of particle size and relatively cheap raw materials are the main advantages of this method. Preparation of metal oxides with different shapes (rods, tubes, flowers, etc) is possible by using this method.

1.8.4. Combustion synthesis

Combustion synthesis (CS) is an effective, low-cost method for the production of various industrially useful materials. It is an exothermic reaction and occurs with the evolution of heat and light. For any combustion, fuel and oxidizer are required. When the mixture of fuel and oxidizer are ignited, combustion takes place. For the combustion synthesis of oxides, metal nitrates are used as oxidizer, and common fuels are hydrazine based compounds or urea or glycine. Depending on the type of the precursors, as well as on conditions used for the process, two types of reaction modes are adopted *ie* self-propagating high temperature synthesis (SHS) mode where the reaction initiates locally and follows a wave-like propagation through the medium, and volume combustion synthesis (VCS) where the reactants are heated uniformly and reaction occurs simultaneously throughout the mixture. Owing to the above-mentioned advantages, this process has been widely used for preparation of variety of advanced materials. [51] This process not only yields nanosize oxide materials but also allows uniform (homogeneous) doping of trace amounts of metal/non metal ions in a single step.

1.8.5. Chemical vapour deposition

In CVD, powders and microcrystalline products are prepared from reactants in the vapor phase, and then can be deposited on a substrate to form single crystal films for devices. Volatile starting materials are heated to form vapours, then mixed at a suitable temperature and transported to the substrate by carrier gas. Typical starting materials include hydrides, halides, and organometallic compounds, since these tend to be volatile. When an organometallic precursor is used, it is called MOCVD (metal organic chemical vapor deposition).

1.8.6. Ion implantation method

Ion implantation is a low-temperature technique for the introduction of impurities (dopants) into semiconductors and offers more flexibility than diffusion. In ion implantation, dopant atoms are volatilized, ionized, accelerated, separated by the mass-to-charge ratios, and directed to the target. The atoms enter into the crystal lattice, collide with the host atoms, lose energy, and finally come to rest at some depth within the solid. The average penetration depth is determined by the dopant, substrate materials, and acceleration energy. Ion implantation energies range from several hundred to several million electron volts, resulting in ion distributions with average depths from < 10 nm to 10 µ. Doses range from 10^{11} atoms/cm^2 for threshold adjustment to 10^{18} atoms/cm^2 for buried dielectric formation. The technique is best suited to materials like semiconductors where small numbers of implanted particles can cause major changes in the material's electrical or physical properties.

1.8.7 Scope of Combustion Synthesis over Conventional Routes

For the production of many advanced materials, the combustion method proves to be an energy-efficient, simple process. This process is preferred for its additional characteristic features such as (i) rapid heating rates, (ii) high temperature, (iii) short reaction time, (iv) use of relatively simple equipment, and (v) formation of products with virtually any size and shape etc. Thus, this process leads to the formation of final products with higher order of purity and better mechanical properties. [52] The high exothermicity of the combustion reaction within a short duration of time is considered as an advantage to design the final phase composition. Due to the high-temperature process, only the thermodynamically stable phases can be prepared. However, controlling the rapid heating and cooling rates enables to obtain metastable materials with new and unique properties. Due to the above advantages, combustion process finds applications in ceramic reinforcements, hydrogen storage, catalytic materials, high temperature superconductors and friction materials.

Lanthanum manganite-lanthanum cobaltite solid solutions ($LaMn_{1-x}Co_xO_3$), candidates of cathode material for solid oxide fuel were successfully prepared by a low temperature initiated solution combustion process using corresponding metal nitrates and tetraformal trisazine. [53] Hegde et al proved that even the noble metals like Pt, Pd and Au could be advantageously dispersed in ionic form over ceria lattice by combustion method, [54] thereby promoting the catalytic activity. Praseodymium-doped ceria red pigments, $Ce_{1-x}Pr_xO_{2-\delta}$, (x=0–0.5) have been prepared by the thermal decomposition of the redox compound $Ce_{1-x}Pr_x(N_2H_3COO)_3.3H_2O$ as well as by the combustion of aqueous solutions containing cerous nitrate, praseodymium nitrate and oxalyl dihydrazide (ODH) /ammonium acetate. [55] The use of ammonium acetate as fuel controls the combustion reaction and yields particles in the range of 7–12 nm.The combustion process not only eliminates the use of mineralisers but also yields voluminous fine particle products in short time. The process appears to be energetically economic and attractive. Interestingly, no phase separation was observed on sintering the solid solutions with higher Pr substitution in CeO_2 indicating the novelty of the combustion process. Nagaveni et al prepared various first row transition metal ions doped nano size titania by solution combustion method using glycine as a fuel. [20] In overall perspective, combustion synthesis is found to be a novel route for preparation of catalytic materials with improved properties. Exploring this route will further enable to obtain a wealth of information that could be advantageous for designing new catalytic materials with greater efficiency. Hence, in the present study novel synthesis procedure for the preparation of N, V, N and Au codoped TiO_2 has been explored.

1.9. Dye Sensitized Solar Cells

Photovoltaics is perhaps the most attractive mode of light harvesting because of the electrically driven power systems, devices, and gadgets of the modern world. Traditionally, the vehicle for photovoltaic device is silicon; however, the same is very expensive and has availability issues. More recently attention is, therefore, focused on newer and novel alternatives to silicon based solar cells. Among these is the dye-sensitized solar cell (DSSC) using titania, which represents a potentially scalable and economically viable option. In 1991, O'Regan and Grätzel [56] first reported the dye sensitized nanocrystalline TiO_2 solar cell (DSSC) with an efficiency of 11% under simulated solar light. Since then, extensive researches have continued to increase the power conversion efficiency (PCE) of DSSC by using various metal oxide semiconductors such as TiO_2, ZnO, SnO_2, Nb_2O_5, $SrTiO_3$ as photoelectrode materials to achieve a reasonable efficiency with low cost. [57] The wide band gap ($E_g > 3$ eV) metal oxide semiconductors, those are having suitable band position relative to sensitizer molecule has been employed as a photoanode for the fabrication of DSSCs. The high surface area of nanoporous metal oxides facilitates the improvement of light absorption with improved dye loading for better performance of DSSC.

The heart of the system is mesoporous semiconducting metal oxide film that is placed in contact with redox electrolyte. A monolayer of the sensitizer (typically bipyridine ruthenium complexes) is attached to the surface of the nanocrystalline metal oxide film in DSSC. DSSC is understood as general electron transport mechanism, where the photoexcited dye injects the electron to the CB of the metal oxides from its LUMO level. A platinized cathode is employed to collect the electrons from the conduction band of metal oxide anode and to catalyze the redox couple *viz.* I^-/I_3^- regeneration reaction. The redox couple of the electrolyte also reduces the oxidized dye. The iodide regenerated, in turn, by the reduction of triiodide at the cathode, with the circuit being completed via electron movement through the external load. The voltage generated under illumination is the difference between the Fermi level of the electron in metal oxide and the redox potential of the electrolyte. Overall, the device generated electric power from sunlight without suffering any enduring chemical conversion.

The photovoltaic parameters of DSSCs are open circuit potential (V_{oc}), short circuit current (I_{sc}), fill factor (FF), and efficiency (η). Short circuit current density (J_{sc}) is the photocurrent per unit active area (A) of the photoelectrode when the applied potential across the DSSCs is zero.

$$Jsc = Isc/A.$$

J_{sc} is effectively dependent on the efficiency of charge injection from the excited dye to the CB of metal oxide. The electron injection efficiency of some widely used metal oxides is found to be the following order: $TiO_2 > Nb_2O_5 > SnO_2 \sim ZnO$. Increase of the back electron transfer and charge recombination is responsible for poor FF.

$$FF(\%) = I_{max} X V_{max} / I_{sc} X V_{oc}$$

Finally, comparing the ratios of total power output (P_{out}) with the solar power input (P_{in}), efficiency (η) can be measured.

$$\text{Efficiency } \eta = J_{sc} V_{oc} FF / P_{in}$$

TiO_2 with anatase nanocrystalline form has been explored extensively in DSSCs photoelectrode due to its suitable band position, high surface area for improved dye loading, and facile synthesis procedure. The electronic state of Ti in TiO_2 is Ti^{4+} ($3d^0$), in which the valence band of TiO_2 is composed of the hybridized 2p orbital of oxygen and the 3d orbital of Ti, while the CB is completely composed of pure 3d orbital of Ti. Hence, the different parity of VB and the CB of TiO_2 decreases the transition of electrons to the VB; consequently, it decreases the electron hole (e^--h^+) recombination probability. Among the polymorphs of TiO_2, it is well known that rutile is the most stable and common form. However, the Fermi level of anatase is 100 mV higher than that of rutile, which leads to higher open circuit potential (V_{oc}). Moreover, the greater surface area of anatase is responsible for efficient dye loading which further leads to higher photocurrent, consequently, higher photovoltaic performance. Brookite is less prominent for DSSC due to its complicated and difficult synthesis process. It is noted that the oxygen vacancies and the titanium interstitials as well as the decreased recombination probability with increased surface area makes TiO_2 an attractive materials for the application in DSSCs**.**

The efficiency of carrier transport and the rate of electron-hole recombination are the two major competing factors [58] that determine the η of any SC. Since grain boundaries hinder transport and enhance recombination, [59] it is highly desirable to have an EINP material in a high surface area framework, such as a mesoporous system, to render high efficiency. DSSC materials are expected to have high surface area since it affects the amount of dye loading and hence the photocurrent and η. Recombination is also less in nanocrystalline TiO_2 compared to bulk and/or nanoparticle TiO_2 with a more amorphous nature. A combination of nanocrystallinity, high surface area in a disordered mesoporous framework, and EINP structure in a single material is expected to increase the carrier transport and hence influence η for a DSSC.

Recently many efforts have been taken to prepare crystalline mesoporous titania. In 2001, Gedanken et al synthesized mesoporous titania by sonochemical method and showed very low efficiency around 1.5%. [60] In 2005, Huang et al prepared mesoporous titania through surfactant templated route and achieved 1.3% efficiency and then by adopting a two step calcinations procedure they achieved around 5% efficiency.[61]

In 2009, Wang et al prepared both ordered bodycentered orthorhombic and disordered wormlike mesoporous titania by supramolecular-templated method and got efficiency around 4.5 and 3.6% respectively. [62] Recently Liu et al prepared the same by facile solvothermal method and reported the efficiency around 1.5 %. [63] Sung et al prepared highly ordered mesoporous Al_2O_3/TiO_2 using P123 template and obtained DSSC efficiency above 6 %. [64] They claimed that alumina coating on mesoporous titania inhibits the charge recombination process and increases both V_{oc} and fillfactor. Hence there are constant efforts are going on in order to make new materials which gives high efficiency in DSSC.

1.10. Oxidative dehydrogenation of Ethylbenzene

Oxidative dehydrogenation (ODH) of ethylbenzene (EB) to styrene is one of the commercially important reactions. Styrene is mainly used in the production of polystyrene and several copolymers. At present, bulk styrene monomer is produced through dehydrogenation of EB on Fe–K–Cr oxide-based catalysts with superheated steam at 700˚C. [65] This dehydrogenation is endothermic in nature (ΔH = 124.85 kJ mol^{-1}), and highly energy intensive process. [65] Although hydrogen is available as a side product, steam-based processes utilize a large amount of latent heat and they pose thermodynamic limitations. Also coke formation on the catalyst leads to severe catalyst deactivation. Moreover, EB conversion of less than 50% was achieved per pass. Hence there are constant efforts are going on to develop alternate catalysts to produce styrene, especially by ODH. [66, 67] Unlike dehydrogenation, ODH is an exothermic reaction and hence the reactions can be carried out at relatively lower temperatures than the conventional endothermic dehydrogenation reactions. Exothermicity also allows the heat energy to be tapped for other applications. Design of new catalysts which gives reasonable conversion with maximum selectivity for this ODH reaction is one of the challenges in the field of heterogeneous catalysis.

In 2005, Shiju et al [68] prepared a series of vanadia-alumina catalysts with different vanadia contents by a wet impregnation method. They found out that the nature of the VO*x* species depends on the vanadia loading and the predominant species are monomeric vanadia at lower loadings, two-dimensional polyvanadates at intermediate loadings, and bulk-like V_2O_5 and $AlVO_4$ at higher loadings. They achieved around 45% styrene yield with 10 wt% V loading using N_2O as the oxidant at 500˚C. Schlögl et al [69] synthesized onion-like carbon material and explored the same for ODH of EB at 520˚C using O_2 and achieved around 62% styrene yield with 68% selectivity.

Drago et al [70] also developed novel carbon-based catalysts with ultrahigh surface area and this catalyst gives extraordinary conversion of around 80% with over 90% selectivity to styrene in a single pass at 350^0C. Hence they proposed that the carbonaceous overlayer observed in many inorganic oxide systems is the true catalyst, and that the surface structure of this carbon is the key to the catalytic activity. Kustrowski et al [71] used many different catalytic systems for ODH of EB reaction. They have also synthesised VOx supported on SBA-15 and performed EB ODH by using N_2O as an oxidant. [72] Recently Liu et al [73] demonstrated around 60% EB conversion and high selectivity with $V_2O_5/Ce_{0.6}Zr_{0.4}O_2\text{-}Al_2O_3$ using CO_2 as an oxidant at 550˚C. Generally for ODH reactions, activity mainly depends on the type of vanadia species and the nature of the support used for the reaction. Titania is an excellent heterogeneous catalyst-support material. Moreover if titania can be stabilised in the thermodynamically stable rutile phase, it would be advantageous to exothermic ODH reactions. [74] EB to styrene ODH is, generally, carried out at high temperature (>500˚C) on supported catalysts, which leads to segregation and agglomeration of active phase. Especially, this is true with V-based catalysts. It is also well known that isolated VO*x* species are active for partial oxidation and polymeric $(VO_x)_n$ species totally oxidises organic moieties and compounds to CO_2. This can be avoided by introducing V into the lattice framework of oxide support material. Lattice incorporation of vanadium has more advantages and it is unlikely to segregate out from the TiO_2 lattice as a result of high temperature or exothermic nature of ODH reaction. Further, this will increase the monomeric or isolated VO_x species in the lattice, which in turn will enhance the activity of ODH reactions. Indeed this concept has not been proposed and evaluated for any ODH reactions. Therefore a simple method to prepare crystalline supports with high surface area along with lattice incorporation of active species is of high relevance.

1.11. Objectives of the Thesis

A survey of literature reports since past few decades reveals that titania is one of the best UV active photocatalyst for many photocatalytic degradation reactions as well as for water splitting reactions. It is well established that doping of anions especially nitrogen reduces the band gap effectively and makes titania into a visible light active photocatalyst. There are many literature reports are available in this area. But only few reports talks about the rate of recombination of charge carriers in those modified N-TiO_2. In order to make best visible light active photocatalyst, both electronic properties as well as textural properties should be tuned in such a way that produced charge carriers have to diffuse very fast and reaches the surface within their life time. Until now only very few reports are combining these aspects in titania.

Mesoporous titania shows better photocatalytic activity than bulk TiO_2. It is mainly attributed to the high surface are of mesoporous materials. As already discussed, pseudo 3D mesoporous materials are having very less diffusional lengths when compared to ordered mesoporous materials. Hence the photogenerated charge carriers reach the surface very quickly. Moreover amorphous materials have large number of defects when compared to crystalline materials. So if we prepare EINP of titania with high surface area the charge carriers will move to the surface without much recombination which in turn increases the efficiency of the photocatalyst. Therefore apart from visible light absorption, Pseudo 3D mesoporous nature, high surface area and electrically interconnected nanocrystalline particles are necessary requirement for getting best active visible light photocatalyst. This aspect has not been explored.

Making nano composites with noble metal clusters is also one of the methods to reduce the recombination probability. Especially Au, Ag noble metal clusters will increase the visible light absorption through its SPR process. Combining pseudo three dimensional $TiO_{2-x}N_x$ with nano gold clusters is possibly the best way to make highly active visible light catalyst for H_2 generation reaction. In these composite materials recombination probability is greatly reduced by nano Au metal clusters. These Au nanoparticles are acting as an electron sink as well as site for proton reduction to hydrogen. The synthesis of nanogold clusters on multifunctional, nanocrystalline and disordered mesoporous $TiO_{2-x}N_x$ by one pot tandem solution combustion method (SCM) has not been pursued extensively.

Moreover vanadium doped titania is an efficient oxidation catalyst in many industrial process especially in oxidative dehydrogenation reactions. Supported vanadium can adopt different structures (isolated vanadium species, polymeric-type species and bulk vanadium oxides) on the support. Isolated vanadium species are responsible for selective oxidation reactions. The method of preparation, type of starting materials, calcination temperature, nature of titania support, additives/impurities and the acid base properties of the support affects the structure of vanadium species in turn affects the catalytic activity. Incorporating active species such as V into TiO_2 lattice gives isolated V species and avoids aggregation during the reaction even at high temperature. This concept has not been explored previously. Simple solution Combustion synthesis helps us to incorporate Vanadium into TiO_2 lattice.

Taking into consideration the above mentioned issues, a stepwise systematic approach to explore those above problems is the main objective of this thesis.

- To prepare and characterize nitrogen doped, nanocrystalline, pseudo three dimensional mesoporous TiO_2 by SCM and to explore it's photocatalytic activity for dye degradation and selective oxidation reactions. These materials are also explored as anode materials in DSSC. The work should also bring out the discussion about the effect of textural properties on the photocatalytic and photovoltaic activity of the materials.
- To prepare and characterize nanogold clusters on multifunctional, nanocrystalline, disordered mesoporous $TiO_{2-x}N_x$ (Au-NT) by one pot tandem SCM. These composite materials exhibit visible light photocatalytic activity and H_2 generation from aqueous methanol has been demonstrated.
- To prepare and characterize mesoporous $Ti_{1-x}V_xO_2$ by simple SCM and explored those materials for oxidative dehydrogenation of EB to styrene at reasonably lower temperature $\leq 500^0$C. Catalytic activity of the spent catalysts has also been checked. Characterization of the spent catalyst is also carried out in order to understand the structure-activity relationship.

1.12. Outline of the Thesis

Chapter 1 presents a brief introduction about the fruits of heterogeneous catalysis in the modern world. Also this chapter describes the importance of TiO_2 in Photocatalysis, photovoltaics and selective oxidation reactions. Present status of cation and anion doping in TiO_2 is also explained briefly in this chapter. It also explains about the importance of composite materials in photocatalysis. Moreover the need of introducing mesoporosity in titania for various applications is also discussed in this chapter. Finally objectives of this thesis also briefly mentioned in this chapter.

Chapter 2 deals with the preparation of mesoporous $TiO_{2-x}N_x$, $Ti_{1-x}V_xO_2$, nano $Au/TiO_{2-x}N_x$ materials by simple solution combustion method (SCM). Also this chapter describes the details of the catalytic activity studies. This chapter briefly describes the working principle of various physico-chemical methods such as X-ray diffraction (XRD), energy dispersive analysis of x-rays (EDAX), N_2 adsorption-desorption isotherm studies, transmission electron microscopy (TEM), Raman spectroscopy, UV-Visible spectroscopy, photoluminescence (PL) and X-ray photoelectron spectroscopy (XPS) and impedance spectroscopy etc.

Chapter 3 is divided into **Part A** and **Part B**. **Part A** presents thorough characterisation results of series of $TiO_{2-x}N_x$ materials. Through various physico-chemical, spectroscopic and microscopic methods, the textural and electronic properties of $TiO_{2-x}N_x$ material is discussed. The effect of urea/Ti ratio on the properties of $TiO_{2-x}N_x$ materials is also discussed. **Part B** deals with the application of $TiO_{2-x}N_x$ materials for various reactions such as rhodamine B degradation, photocatalytic oxidation of p-anisyl alcohol and also in DSSC.

Chapter 4 presents detailed characterization results of nano $Au/TiO_{2-x}N_x$ composite materials. Charge recombination probability is greatly reduced by nano Au metal clusters is demonstrated by various techniques. High activity of these composite materials is supported by H_2 generation from aqueous methanol under visible light.

Chapter 5 deals with the detail characterization of series of $Ti_{1-x}V_xO_2$ material with different V concentration. Lattice incorporation of active species is proved by various techniques like XRD, Raman and FT-IR techniques. Oxidative dehydrogenation of EB to styrene is successfully carried out by $Ti_{1-x}V_xO_2$ at low temperature around 500^0C. Spent catalysts are analyzed thoroughly in order to understand the structure activity relationship. These catalysts can be easily regenerated after the reaction by simple calcinations.

Chapter 6 summarizes the conclusions derived based on the observation and results obtain from the entire study. At the end scope of further research work in the area of the present study have also been pointed out.

1.13. References

1. B. Lindströma, L. J. Pettersson. *cat tech.* **7** (2003) 130.
2. G. Ertl, H. Knozinger and J. Weitkamp, *Handbook of Heterogeneous Catalysis,*Vol. **1** Wiley- VCH, Weinheim, 1997.
3. G. Centi, S. Perathoner, *Catal. Today* **77** (2003) 287.
4. T. Fröschl, U. Hörmann, P. Kubiak, G. Kucerova , M. Pfanzelt, C. K. Weiss, R. J. Behm, N. Husing, U. Kaiser, K. Landfesterd, M. Wohlfahrt-Mehrensc. *Chem. Soc. Rev*. **41** **(**2012) 5313.
5. J.E. Huheey, E.A. Keiter, R. L. Keiter, "*Inorganic Chemistry- Principles of Structure and Reactivity,* Pearson Education, Fourth Edition.
6. K. Hashimoto, H. Irie, A. Fujishima Japanese Journal Of Applied Physics **44** (2005) 8269.
7. R. Jelks, "Titanium: Its Occurrence, Chemistry, and Technology: Ronald Pmss. New York. 1949. pp. 401-404.452-456.472.
8. **A.** L. Linsebigler, G. Lu, J. T. Yates, Jr. *Chem. Rev.***, 95** (1995) 735**.**
9. J.K. Burdett, T. Hughbands, J.M. Gordon, J.W. Richardson, J.V. Smith, J. V. *J. Am. Chem. Soc.* 109 (1987) 3639.
10. R.W. Matthews, J. *Catal.* **113** (1988) 549.
11. A. Fujishima, K. Honda, *Nature* **238** (1972) 37.
12. A. Fujishima, T. N. Rao, D. A. Tryk, **1** (2000) 1.
13. R. Asahi, T. Morikawa, T. Ohwaki, K. Aoki and Y. Taga, *Science,* **293 (**2001) 269.
14. A. Zaleska, Recent Patents on Engineering, **2** (2008) 157.

15. W.Choi, A. Termin M.R. Hoffmann. *Angew. Chem. Int. Ed*. **33** (1994) 1091.
16. M. Anpo and M. Takeuchi, *J. Catal*., **216** (2003) 505.
17. M. Anpo, *Pure Appl Chem* **72** (2000) 1787.
18. H. Yamashita, M. Harada, J. Misaka, M. Takeuchi, K. Ikeue, M. Anpo photocatalysts. J *Photochem Photobiol A*; **148** (2002) 257.
19. J. C.-S. Wu, C-H Chen. *J. Photochem. Photobiol*., *A* **163** (2004) 509.
20. K. Nagaveni, M.S. Hegde and M. Giridhar, *J. Phys. Chem. B,* **108** (2004) 20204.
21. K. Bhattacharyya, S. Varma, A.K. Tripathi, S.R. Bharadwaj, A.K. Tyagi, *J. Phys. Chem. C,* **112** (2008) 19102.
22. X. Chen, S. Shen, L. Guo, S. S. Mao *Chem. Rev.* **110** (2010) 6503.
23. S. Sato, *Chem. Phys. Lett.*, , **123** (1986) 126.
24. M. Sathish, B. Viswanathan, R.P. Viswanath and C.S. Gopinath, *Chem. Mater.*, **17** (2005) 6349.
25. M. Sathish, R. P. Viswanath and C. S. Gopinath, *J. Nanosci. Nanotech.* **9** (2009) 423.
26. G. Liu, L. Wang, C. Sun, X. Yan, X. Wang, Z. Chen, S. C. Smith, H-M. Cheng, G. Q. Lu, *Chem. Mater* **21** (2009) 1266.
27. H. Kisch, S. Sakthivel, M. Janczarek, D. Mitoraj, *J. Phys. Chem. C*, **111** (2007) 11445.
28. S.C. Waren, E. Thimsen, *Energy Environ. Sci*. **5** (2012) 5133.
29. B. Juluri, M. Lu, Y. B. Zheng, T.J. Huang, L. Jensen, L. *J. Phys. Chem. C. **113*** (**2009)** 18499.
30. S. Linic, P. Christopher, D.B. Ingram, *Nat. Mater*, **10** (2011) 911.
31. G.R. Bamwenda, S. Tsubota, T. Nakamura, M. Haruta, *J. Photochem. Photobiol., A* 89 (1995) 177.
32. M. Murdoch, G.I.N. Waterhouse, M.A. Nadeem, J.B. Metson, M.A. Keane, R.F. Howe, J. Llorca, H. Idriss. *Nat. Chem.* **3** (2011) 489.

33. M. Jakob H. Levanon, P. V. Kamat *Nano Lett.,* **3** (2003) 353.
34. V. Subramanian, E.E. Wolf, P.V. Kamat, *J. Am. Chem. Soc*. **126** (2003) 4943.
35. H. Li, Z. Bian, J. Zhu, Y. Huo, H. Li, Y. Lu. *J. Am. Chem. Soc* **129** (2007) 4538.
36. J-J. Chen, J. C. S. Wu, P. C. Wu, and D. P. Tsai. *J. Phys. Chem. C* **115** (2011)210**.**
37. J. Graciani, A. Nambu, J. Evans, J. A. Rodriguez, and J. F. Sanz.. *J. Am. Chem. Soc* 130 (2008) 12056.
38. M. Alvaroa, B. Cojocarub, A.A. Ismailc, N. Petread, B. Ferrera, F. A. Harrazc, V. I. Parvulescub, H. Garcia, *Appl. Catal. B: Environ.* **99** (2010) 191.
39. Y. Wu, H. Liu, J. Zhang, and F. Chen. 2009. *J. Phys. Chem. C* **113** (2009)14689.
40. B. Chi, L. Zhao, and J. Tetsuro *J. Phys. Chem. C,* **111** (2007) 6189.
41. S. Basu, M. Mapa, C.S. Gopinath, M. Doble, S. Bhaduri and G.K. Lahiri, *J. Catal.* **239** (2006) 154.
42. S.B. Waghmode, R. Vetrivel, S.G. Hegde, C.S. Gopinath and S. Sivasanker, *J. Phys. Chem. B,* **107** (2003) 8517.
43. S.S. Kim, T.R. Pauly and T. Pinnavaia, *Chem. Commun*. (2000) 835.
44. Z. Zhang and T. Pinnavaia, *J. Am. Chem. Soc.* **124** (2002) 12294.
45. B. Naik, K. M. Parida, and C.S. Gopinath *J. Phys. Chem. C***, 114** (2010) 19473.
46. X. Chen, T. Yu, X. Fan, H. Zhang, Z. Li, J. Ye, Z. Zou, Z. *Appl. Surf. Sci.*, **253** (2007) 8500.
47. Y. Noda, B. Lee, K. Domen, J.N. Kondo, *Chem. Mater.*, 20, (2008) 5361.
48. S.P. Gaikwad, S.R. Dhage, H.S. Potdar, V. Samuel, V. Ravi, J. Electroceram. 14 (2005) 83.
49. C.J. Brinker, G.W. Scherer, Sol-gel Science: The Physics and Chemistry of Sol-gel Processing, Academic Press, Boston, MA, 1990.
50. U.G. Akpan, B.H. Hameed *App. Catal. A: General* **375** (2010) 1.

51. S. T. Aruna, A. S. Mukasyan, *Curr. Opin. Solid State Mater. Sci.* **12** (2008) 44.
52. J. J. Moore and H. J. Feng, *Prog. Mater. Sci*. **39** (1995) 243. (b) A. G. Merzhenov, *J. Mater. Chem*. **14** (2004) 1779.
53. S.T. Aruna, M. Muthuraman, K.C. Patil, *Mater. Res. Bull*.**35** (2000) 289.
54. P. Bera, K. C. Patil, V. Jayaram, G. N. Subbanna, and M. S. Hegde *J. Catal.***196** (2000) 293.
55. S.T. Aruna, S. Ghosh, K.C. Patil, Int. J. Inorg. Mater. **3** (2001) 387.
56. B. O'Regan, M. Grätzel, *Nature*, **353** (1991) 737.
57. J-J. Lee, M. M. Rahman, S.Sarker, N.C. Deb Nath,A.J. S. Ahammad and J. K. Lee Advances in Composite Materials for Medicine and Nanotechnology 181-210, chapter 7.
58. M. Grätzel, *Nature*, , **414** (2001) 338.
59. Snaith,H.J. *Adv. Funct. Mater*., **20** (2010) 13.
60. Y-Q. Wang, S-G. Chen, X-H. Tang, O. Palchik, A. Zaban, Y. Koltypin, Gedanke *J. Mater. Chem.*, **11** (2011) 521.
61. K. Hou, B. Tian, F. Li, Z. Bian, D. Zhao, C. Huang, *J. Mater. Chem.*, **15** (2005) 2414.
62. Y. Zhang, Z. Xie, J. Wang, *ACS Appl. Mater. Interfaces*, **12** (2009) 2789.
63. L. Li, C-Y. Liu, *J. Phys. Chem. C*, **114** (2010) 1444.
64. J-Y. Kim, S. H. Kang, H. S. Kim, and Y-E. Sung, *Langmuir* **26** (2010) 2864.
65. K.K. Kearby, in: P.H. Emmett (Ed.), Catalysis, vol. 3, Reinhold, New York, 1955, Chapter 10.
66. F. Cavani, F. Tifiro, *Appl. Catal. A:Gen.* **133** (1995) 219.
67. Y. Sakurai, T. Suzaki, N-O. Ikenaga, T. Suzuki, *Appl. Catal. A:Gen.* **192** (2000) 281.
68. N.R. Shiju, M. Anilkumar, S.P. Mirajkar, C.S. Gopinath, B.S. Rao, C,V. Satyanarayana, *J. Catal*., **230** (2005) 484.

69. N. Keller, N.I. Maksimova, V.V. Roddatic, M. Schur, G. Mestl, Y.V. Butenko, V. Kuznestsov, R. Schlogl, *Angew. Chem. Int. Ed.*, **41** (2002) 1885.

70. (a) R.S. Drago, K. Jurczyk, *Appl. Catal. A:Gen.*, **112** (1994)117; (b) G.C. Grunewald, R.S. Drago, *J. Mol. Catal.*, **58** (1990) 227.

71. T. Badstube, H. Papp, P. Kustrowski, R. Dziembaj, *Catal.Lett.* **55** (1998) 169.

72. P.Kustrowski, Y.Segura, L. Chmielarz, J. Surman, R. Dziembaj, P.Cool, *Catal. Today*, **114 (**2006) 307.

73. Z. W. Liu, C. Wang, W.B.Fan, Z.T.Liu, Q.Q. Hao, X. Long, J.Lu, J.G.Wang, Z.F.Qin, D.S.Su, *ChemSusChem*, **4** (2011) 341.

74. W.E. Slinkard, P.B. De Groot *J. Catal*.**, 68** (1981) 423.

Chapter 2

Experimental Methods

2. Experimental Methods

Development of new materials with unique properties is entirely based on the synthetic procedures followed for the preparation of such materials. The catalytic properties of heterogeneous catalysts are strongly affected by every step of the preparation together with the quality of the raw materials. [1] Usually it requires complex procedures. However, in the present case, solution combustion method (SCM) has been employed to prepare novel TiO_2 based materials. Success of the present materials preparation was due to favourable reaction condition produced by the reactant itself, such as in situ generation of ammonia from the decomposition of urea. Interestingly, in these SCM prepared TiO_2 materials, *pseudo* 3D mesoporosity is achieved without using any templates. Introduction and theory of various physical, structural and spectroscopic characterization techniques employed in the characterization of TiO_2 based materials in the investigation has also been desired.

2.1. Catalyst Preparation

In this thesis, we followed a simple SCM technique [2] in order to prepare disordered mesoporous, heteroatoms incorporated in the lattice framework of TiO_2. This is an alternative synthetic method for producing a wide variety of simple and complex inorganic materials having excellent physicochemical properties. The method is gaining more interest for the preparation of variety of materials, such as, nitrides, carbides, many composite materials and to enhance metal ion distribution on oxides etc. Furthermore, it is characterized by fast heating rates, high-reaction temperatures, and short reaction times. [3] Owing to high exothermicity of the system, combustion temperature rapidly reaches to high temperatures (higher than furnace temperature for few seconds) and converts the precursor material to fine crystallites of the desired complex oxide. Of course the maximum temperature reached under SCM conditions strongly dependent on metal nitrate, reactant. While 1:1 ratio of

$Zn(NO_3)_2$:urea shows a maximum furnace T around 700^0C, titanium counterpart shows no significant increase in furnace T.

2.1.1 Aspect of Nitrogen Doped TiO_2 Synthesis ($TiO_{2-x}N_x$)

Nitrogen doped mesoporous TiO_2 is prepared through SCM [4-6] which is a simple process and it requires a short reaction time (usually less than one minute) and cheap starting materials. All the chemicals employed were of analytical grade and used as such without any further purification. Titanium nitrate (Sigma-Aldrich) as Ti precursor and urea (Merck) as fuel were used. Equimolar amount of (0.02 mol) titanyl nitrate and urea (1:1 molar ratio) were taken in a 250 ml beaker with 10 ml water and introduced into a muffle furnace maintained at 400^0C. Water evaporation takes place in the first few minutes, followed by smoldering type combustion that occurs in the next 1-2 min. Solid products were obtained within ten min. Series of $TiO_{2-x}N_x$ materials were prepared by changing the fuel/oxidizer ratio from 1, 3, 5, 7, 9, and 10. Crystalline phases, crystallinity and textural properties of the final product (anatase/rutile) are controlled by altering the oxidizer to fuel ratio. [7]

For evaluating the relative exothermicity of combustion reactions involving different fuels, a simplified theoretical approach has been considered. The following combustion reactions that are balanced to give pure TiO_2 have been considered. The combustion synthesis can be expressed (but over simplified) as follows:

$$(NH_2)_2CO + TiO(NO_3)_2 \rightarrow TiO_{2-x}N_x \qquad (2.1)$$

$$TiO(NO_3)_2 + (\varphi)\ (NH_2)_2CO + [1.5\varphi-2.5]\ O_2 \rightarrow TiO_2 + (1+\varphi)N_2 + \varphi CO_2 + 2H_2O \qquad (2.2)$$

In the above equations, φ = ratio between fuel and metal nitrate, when φ = stoichiometric ratio of the initial reaction mixture, it does not require atmospheric oxygen for complete oxidation of fuel. In this case, $\varphi = 1.67$ corresponds to the situation of an 'equivalent stoichiometric ratio', which implies that the oxygen content of titanyl nitrate can be completely reacted to oxidize/consume urea exactly. As a result, TiO_2, CO_2, H_2O, N_2 and oxides of nitrogen can be formed directly from the reaction between fuel and oxidizer without the necessity of getting oxygen from outside. For φ> 1.67 (<1.67) implies fuel rich (lean) conditions. Depending on the fuel to metal nitrate ratio, structural phase and properties of $TiO_{2-x}N_x$ material varies. Maximum temperature generated under combustion conditions is strongly dependent on the fuel to oxidizer ratio.

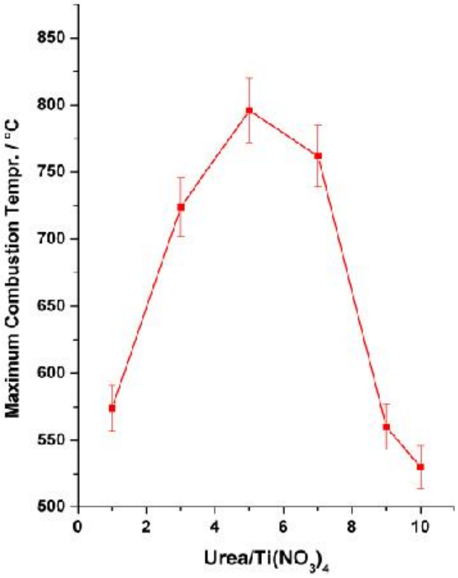

Figure 2.1: Maximum combustion temperature expected (it is from calculations) for various urea/titanyl nitrate ratios.

When the above ratio is less than or equal to the stoichiometry value (1.67) less combustion temperature (500–600^{0}C) was observed due to flameless or smoldering type combustion. [8–10] When the urea/oxidizer ratio is higher than the stoichiometry value, a voluminous type of combustion occurs and hence a high temperature (700–800^{0}C) is generated. Further increase in the fuel content again leads to flameless combustion due to low concentration of oxidizer. In this case, the combustion reaction is partly supported by the ambient air and the reaction rate is limited by the diffusion of oxygen. Therefore only intermediate ratios of urea/titanium nitrate have more rutile content, due to combustion temperatures close to 800^{0}C.

Smoldering combustion occurs when urea/Ti ratio is either low or high. Unlike voluminous combustion, this smoldering combustion is a slow process and also in this case combustion temperature is not increasing rapidly. This situation is very much favourable for growth of nanoparticles. Moreover, lot of gaseous by-products such as CO_2, NH_3 and NO_2 are produced during this smoldering combustion. Hence, these gases prevent the grain growth [11] of titania particles. Also these gases prevent dense packing of the particle and results in anatase phase with disordered porosity.

Main purpose of employing urea as fuel is to avoid any carbon impurities. During the combustion process, in situ generation of NH_3 occurs due to urea decomposition, and this acts as nitrogen source as well as creating a reduction atmosphere. Nascent nano titanium-oxo clusters (Ti_xO_y, $x/y > 1$) grow to bigger clusters/particles in the ammonia atmosphere; these clusters are bound to have many defects and ammonia being a highly electron donating compound finds interacting with the above defects rich clusters easy. This interaction results in N-doped TiO_2 with novel properties.

It is to be noted that the thermal decomposition of urea leads to ammonia and CO_2, in the presence of metal oxide and water vapour. [12] Indeed it is the same principle employed in selective catalytic decomposition of NO_x with urea solution [12] in the present generation automotive catalysts employed in diesel operated vehicles in Europe. The above urea decomposition concept is successfully utilized in our preparation method. Further, this procedure leaves no trace of any organic impurities on the resulting $TiO_{2-x}N_x$ materials under the present experimental conditions, by the very nature of complete conversion of urea to ammonia and CO_2.

2.1.2. Nitrogen and Au Co-doped TiO_2 (nano Au-$TiO_{2-x}N_x$)

Nano Au clusters on mesoporous $TiO_{2-x}N_x$ (Au-NT) composites were prepared by the above mentioned simple SCM method. [13] All the chemicals employed were of analytical grade and used as such without any further purification. Titanium nitrate (Sigma-Aldrich) as Ti precursor, gold (III) chloride (Sigma-Aldrich) as gold precursor and urea (Merck) as fuel were used. Required quantity of aqueous titanyl nitrate, gold chloride and urea were taken in a 250 ml beaker and introduced into a muffle furnace maintained at 400^0C. Water evaporation takes place in the first few minutes, followed by smoldering type combustion that occurs in the next 1-2 min. Solid products were obtained within ten min. Series of nano gold on nitrogen doped mesoporous titania (xAu-NT) composite materials were prepared by changing the Au/Ti molar ratio from 0 to 0.3 with fixed (urea/$Ti(NO_3)_4$) fuel/oxidizer ratio equal to 10. [13] In xAu-NT, x stands for nominal Au atom %. During combustion process, in situ generation of NH_3 occurs due to urea decomposition, and this acts as nitrogen source as well as creates a reduction atmosphere to reduce Au^{3+} to Au clusters.

2.1.3. Vanadium doped TiO_2 ($Ti_{1-x}V_xO_2$)

$Ti_{1-x}V_xO_2$ materials were prepared by SCM method. All the chemicals employed were of analytical grade and used as such without any further purification. Titanyl nitrate (Sigma-Aldrich) as Ti precursor, ammonium meta vanadate (Sigma–Aldrich) as vanadium precursor and urea (Merck) as a fuel were used as such. All TVx materials were prepared with 1:1 molar ratio of urea to metal ions (Ti + V). x in TVx indicating the nominal vanadium atom percentage. Aqueous solution of the desired amount of titanyl nitrate, ammonium meta vanadate and urea were taken in a 250 ml beaker and introduced into a muffle furnace maintained at 400°C. Water evaporates in the first few minutes followed by smoldering type combustion that occurs and continues for about 1 min. Solid products were obtained within 15 min of total preparation time. A series of catalysts were prepared by changing the nominal vanadium content from 2 to 15 atom%. [14]

2.2. Method of Catalytic Activity Studies

2.2.1. Rhodamine B Degradation

Photocatalytic activity of disordered mesoporous $TiO_{2-x}N_x$ materials were analyzed by Rhodamine-B (RhB) degradation under direct sunlight as well as by photocatalytic reactor (double jacketed borosil reactor that was equipped with a 125W W lamp) with visible light (>420 nm). This reaction was mainly to screen all the materials to find the most active catalyst. 100 mg of catalyst was dispersed in 100 ppm aqueous solution of RhB dye in a 250 ml beaker. Several such beakers were kept under direct sunlight up to 7 h from 10 am on typical sunny days. The extent of dye degradation was analyzed by an ultraviolet visible (UV-vis) spectrophotometer (Shimadzu, Model UV-2500PC). Degradation of RhB was followed with 532 nm band in the absorption spectrum as a function of light exposure time.

2.2.2. Photocatalytic Oxidation of p-anisyl alcohol

Photocatalytic oxidation of aqueous p-anisyl alcohol was also carried out under direct sunlight as well as with laboratory sources (>420 nm) in aqueous solution with $TiO_{2-x}N_x$ catalyst. Photocatalytic oxidation of p-anisyl alcohol was also carried out without $TiO_{2-x}N_x$. Product formation was analyzed by both UV-vis spectrophotometer and gas chromatograph (GC) equipment (Agilent, Model 6890 J- 413) that consisted of a HP-5.5% phenyl methyl siloxane capillary column and flame ionization detector (FID). A similar oxidation trend was observed in direct sunlight as well as with laboratory visible light source.

2.2.3. Photocatalytic Water Splitting Reaction

Visible light driven water splitting reactions were carried out in order to prove the photocatalytic activity worthiness of the materials. The reaction was carried out at ambient conditions using a borosil photoreactor of ca. 50 ml capacity, equipped with a port for the withdrawal of gas samples at regular intervals. For each experiment, 50 mg of fresh catalyst was dispersed in 40 ml water and 10 ml methanol to serve as sacrificial reagent. 125 W white light source was used as irradiation source. The lamp was positioned at 8 cm away from the reaction cell. The experiments were conducted at neutral pH. Hydrogen evolved was sampled and analyzed periodically on a gas chromatograph (Chemito, model-8610, Porapak-Q column, thermal conductivity detector at 353 K).

2.2.4. Vapour Phase Oxidative dehydrogenation of Ethylbenzene

Vapor phase experiments were performed at atmospheric pressure in a fixed bed, vertical, down-flow, integral glass reactor placed inside a double-zone furnace (Geomechanique, France). Fresh catalyst was charged each time at the center of the reactor in such a way that the catalyst was sandwiched between the layers of inert porcelain beads. Catalyst and porcelain beads are separated by glass wool. The upper portion of the reactor served as a vaporizer cum pre-heater. All heating and temperature measurements were carried out using ‘Aplab’ temperature controller and indicator instruments. A K-type thermocouple was positioned at the center of the catalyst bed to monitor the exact temperature of the catalyst. The reactant mixture was fed into the reactor using a syringe pump (Braun, Germany) at a desired flow rate. Reaction products were collected from a condenser fixed below the reactor and circulated with ice cold water. Products were analyzed using gas chromatography (GC) equipment (Agilent, Model 6890 J-413) that consist of a HP 5.5% phenyl methyl siloxane capillary column that was equipped with flame ionization detection (FID).

Vapor phase oxidative dehydrogenation of EB was carried out using 1 g of catalyst with particle size up to 10 mesh. The reactant (EB) was fed using a syringe pump at a weight hourly space velocity (WHSV) of 2. Oxygen is used as an oxidant. 40 ml min^{-1} is fixed as an optimum flow rate of oxygen. We deliberately used molecular O_2 in order to increase the reaction rate, minimize coke deposition as well as to inhibit catalyst deactivation. The reproducibility for different products was checked experimentally, and the measurements were repeated three times with a relative error of ± 2% for high conversion/selectivity measurements and ± 5% for low conversion/selectivity measurements. The thermal process without catalysts was negligible in all the cases. Catalyst regeneration activity is monitored after calcining the spent catalysts by simply passing oxygen for 20 min at 500°C. Little amount of coke deposited during the reaction can be burnt off by oxygen.

2.2.5. Photovoltaic Measurements

The doctor blade method was used to fabricate meso-UTx films with the thickness around ~12 μm. In order to sensitize, these films were impregnated with 0.5 mM N719 dye in ethanol for 24 h at room temperature. Coated films were washed with ethanol. [15] J-V characteristics were measured under irradiation with 100 mW/cm^2 (450 W xenon lamp, Oriel Instruments), 1 sun AM 1.5, simulated sunlight as a solar simulator. The current was measured using a Kiethley 2400 source. The electrolyte used was 0.6 M 1,2 dimethyl 3-propyl imidazolium iodide, 0.1 M LiI, 0.05 M I2, and 0.5 M 4-tert-butylpyridine in acetonitrile.

2.2.6. Impedance Measurements:

The impedance measurements of all materials were performed in order to check the resistance at different interfaces in the solar cell assembly. The frequency range chosen for the measurement was from 10^{-2} Hz to 106 Hz with AC amplitude of 10 mV. The impedance spectrum of DSSC mainly consists of 3 semicircles attributed to the interface between Pt|electrolyte (Z1), TiO_2|dye|electrolyte (Z2), and diffusion of I_3^- (Z3) in the electrolyte, respectively. The resistance elements R1, R2, and R3 are described as the real part of Z1, Z2, and Z3, respectively. The resistance element R_h in the high frequency range over 1 MHz is influenced by the sheet resistance of transparent conducting oxide (TCO) and the contact resistance between the TCO and TiO_2. The former is the main factor in R_h, as the value of R_h

increases in direct proportion to the sheet resistance of TCO. The impedance measurements were made at room temperature using Autolab PGSTAT30 (Eco-Chemie).

2.2.7. Photoelectrochemical measurements (PEC)

The photoelectrochemical properties of all materials were measured by linear sweep voltametry (LSV) using Autolab PGSTAT30 (Eco-Chemie) instrument in a conventional three-electrode test cell with platinum wire and a platinum foil as the reference and counter electrodes, respectively, in 1 M NaOH solution at ambient conditions. For preparing the working electrode, the FTO plates are washed thoroughly with acetone and IPA after that catalyst slurry made by 5 mg catalyst in 1 ml of isopropanol was drop casted on the electrode surface and dried at room temperature for overnight. This electrode was used as the working electrode for all the electrochemical studies. Lamp used - 400 W medium pressure Hg vapor UV lamp.

2.3. Physicochemical Characterization

2.3.1. Introduction

Thorough physicochemical characterization is major aspect to understand any material including catalyst. Diffraction, spectroscopy, microscopy, and methods based on adsorption and desorption are the routine material characterization techniques. It gives information about phase structure, crystallinity, crystallite size, optical properties, surface structure, textural properties, nature of active sites, morphology, particle size, acidity and other characteristic features. It also gives better knowledge about the nature and chemical state of dopant. Further, the structure-activity relationship is understood by these techniques which help us to improve the activity of the catalyst for various applications. A number of analytical techniques have been used to characterize catalysts, which include X-ray diffraction analysis (XRD), Raman spectroscopy, FT-IR, surface area and pore volume measurements, Transmission electron microscopy (TEM), UV-visible spectroscopy, Energy dispersive X-ray (EDX) analysis, X-ray photoelectron spectroscopy (XPS), Photoluminescence spectroscopy and Electrochemical Impedance spectroscopy. These techniques help to understand the materials as well as catalyst in a better way, so that materials can be improved or designed in better way as required. The following part gives a brief account of the theory and principle of various characterization techniques used for the current study. The procedure for each experimental technique is also described in this part.

2.3.2. Theory and Experimental Procedures

2.3.2.1. X-ray Diffraction (XRD)

XRD is one of the most common techniques used in catalyst characterization. It has been the most important technique for determining the structure of materials. It is used to identify crystalline phase(s), percent crystallinity and crystallite size of the catalyst [16]. X-rays are invisible, electrically neutral, electromagnetic radiations. Generally, their frequencies are intermediate between the ultra-violet (UV) and gamma radiations and their wavelength (λ) range from approximately 0.04 Å to 1000 Å. For diffraction applications, only short wavelength x-rays in the range of a few Å to 0.1 Å (1 keV -12 keV) are used; since this wavelength of X-rays is comparable to the size of atoms, hence they are ideally suited for probing the structural arrangement of atoms and molecules in a wide range of materials. The energetic X-rays can penetrate deep into the materials and provide information about the bulk structure. When electromagnetic rays are incident on a solid material (grating), they are either coherently/in-coherently scattered or absorbed. The coherent scattering of rays can interfere with each other giving bright (constructive interference) and dark (destructive interference) fringes. However, the scattered rays will become constructive only at a particular angle when the path difference between the two rays, differ by an integral number of wavelength. This phenomenon is broadly termed as X-ray Diffraction. The classical Bragg's law [17] of diffraction that relates the possibility of constructive interference to the inter-planar separations is given by the following equation

$$n\lambda = 2d\sin\theta \tag{2.3}$$

where λ is the wavelength of X-rays, θ is the glancing angle (called as Bragg's angle), d is inter-planar separations, and n is the order of diffraction. Each plane is characterized by miller indices given by (hkl). A schematic representation of the X-ray Diffraction is illustrated in Fig. 2.2.

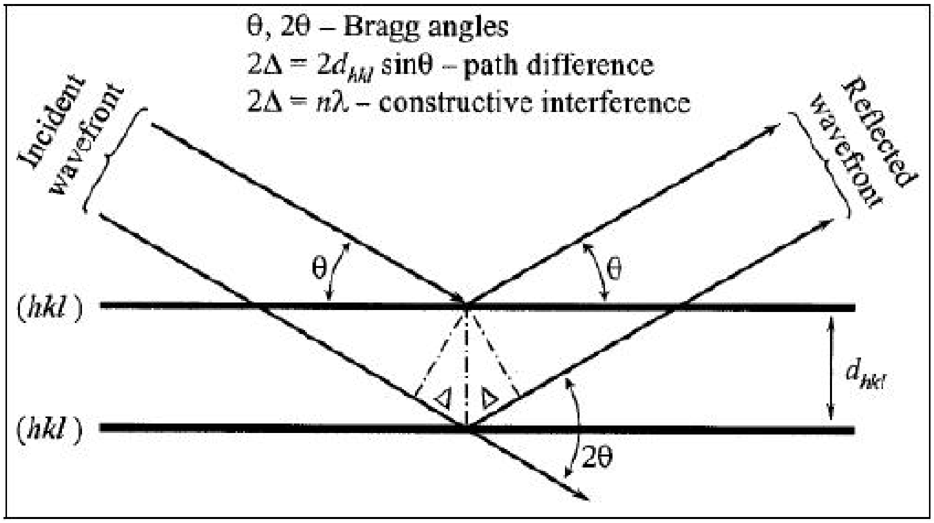

Figure 2.2: Schematic diagram of X-ray Diffraction

This phenomenon of X-ray diffraction can be extended to crystalline materials to extract their qualitative and quantitative informations. Output of the diffraction measurement is obtained as plot of diffracted x-rays versus incident angle. The angle where the incident beam meets the Bragg's angle (θ) for a particular plane, constructive interference among the diffracted x-rays from that plane occurs, giving a sharp intensity peak. A short time scan in the 2θ range of 10 to 70° is sufficient for the identification of a well crystalline inorganic material. The scan time can be optimized for getting good intensity peaks. In the present study, the observed diffraction patterns were compared with JCPDS (Joint Committee on Powder Diffraction Standards, 1974) files available for reported crystalline samples. By measuring the angle, 2θ, under which constructively interfering X-rays leave the crystal, the Bragg's equation gives the corresponding lattice spacing, which is characteristic for a particular compound. Width of the diffraction peaks signifies the dimension of the reflecting planes. It is known that the width of a diffraction peak increases when the crystallite size is reduced below a certain limit (<100 nm). Therefore, XRD patterns can be used to estimate the average crystallite size by using Scherrer formula which is given as

$$t = \frac{0.9\lambda}{B\cos\theta_B} \qquad (2.4)$$

where t is the thickness of the crystal (in Å), λ the X-ray wavelength and θ_B the Bragg angle. The line broadening, B, is measured from the full width at half maximum (FWHM) and is obtained from the Warren formula:

$$B^2 = B_M^2 - B_S^2 \qquad (2.5)$$

where B_M is the measured peak width in radians at half peak height and B_S is the measured peak width of a peak of a standard material (silicon). PXRD patterns of all the catalysts reported in this thesis were collected from PANalytical X'pert Pro dual goniometer X-ray diffractometer. A proportional counter detector was used for low angle experiments. The data were collected with a step size of 0.02^0 and a scan rate of 0.5^0 min^{-1}. The sample was rotated throughout the scan for better counting statistics. The radiation used was Cu-Ka (1.5418 Å) with Ni filter and the data collection was carried out using a flat holder in Bragg–Brentano geometry (0.2^0).

2.3.2.2. Surface Area Determination by BET Method

Surface area is a significant powder property of nano-crystalline materials. The nano powders consisting of ultra fine crystals are typically characterized by a large surface-to volume ratio. Thus, they exhibit large surface area owing to higher surface energy. The specific surface area (in m^2/g) of powder samples was measured through Brunauer-Emmet-Teller (BET) method **[**18**]** by using the BET equation:

$$\frac{P}{V_{ads}(P_0 - P)} = \frac{1}{V_m C} + \left[\frac{(C-1)}{V_m C}\right] * \frac{P}{P_0} \qquad (2.6)$$

where P = adsorption equilibrium pressure, P_0 = standard vapor pressure of the adsorbent, V_{ads} = volume at STP occupied by molecules adsorbed at pressure P, V_m = volume of adsorbate required for a monolayer coverage, and C = constant related to heat of adsorption. It is based on the determination of the amount of gas that is adsorbed on the surface of a powder in a monomolecular layer. To determine the surface area by the BET method, the amount of gas adsorbed in a monomolecular layer on the surface of a powder and the area occupied by a molecule of the adsorbed gas must be known. The latter value is 16.2×10^{-20} m^2 for nitrogen.

To differentiate the adsorption mechanism between micro-pore and to that in meso and macro-pores, the *t-plot* analysis was developed by Lippens and de Boer and the same was applied. [19] The method consists of plotting the adsorption isotherm in terms of the volume of the adsorbate versus the statistical film thickness, *t*. The pore size distribution is obtained from the analysis of the desorption isotherms by applying the BJH expand model [20] which involves the area of the pore walls and uses the Kelvin equation to correlate the partial pressure of nitrogen in equilibrium with the porous solid to the size of the pores where the capillary condensation takes place.

Nitrogen adsorption/desorption isotherms for all materials were collected from Quantachrome autosorb automated gas sorption system (NOVA 1200). The Brunauer–Emmett–Teller (BET) equation was used to calculate the surface area from the adsorption branch. The pore size distribution was calculated by analyzing the adsorption branch of the nitrogen sorption isotherm using the Barrett–Joyner–Halenda (BJH) method.

2.3.2.3. Transmission Electron Microscopy

Microstructural characterization has become important for all types of materials as it gives substantial information about the structure-property correlation. Microstructural characterization broadly means ascertaining the morphology, identification of nature of porosity, estimating the particle size etc. These studies cannot be performed using optical microscopes as they have resolution limitations. This paved the way for the development of electron microscope by Knoll and Ruska in 1932. [21] Electron microscopy is based on the interaction between electrons (matter wave) and the sample. When electron interact with specimen various phenomena occurs as shown in Fig. 2.3. Transmission Electron Microscopy involves investigation of the transmitted electron from the thin sample. Transmission Electron Microscopy (TEM) gives details about the nature of nano powders and their particle size. In TEM, a beam of focused high-energy electrons is transmitted through the sample to form an image, which reveals information about its morphology, porosity and particle size distribution at a spatial resolution of 1.4 nm.

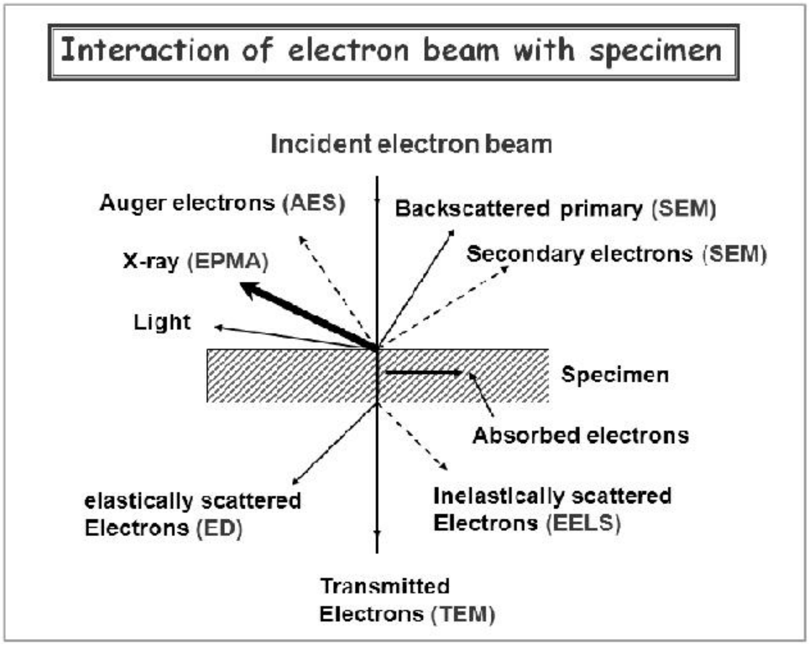

Figure 2.3: Interaction of electron with specimen

TEM is a unique technique as it can focus electron on a single nano particle and can determine its size and morphology. This technique can be applicable to a variety of materials such as metals, ceramics, semiconductors, minerals, polymers etc. The first transmission electron microscope was constructed by Manfred von Ardenne in 1933. A TEM setup consists of an electron gun, voltage generator, vacuum system, electromagnetic lenses and recording devices. Usually thermionic gun (tungsten filament, LaB_6 crystal) or field emission gun is used as an electron source to illuminate the sample specimen. The electrons thus produced are accelerated at chosen voltages by a voltage generator. The acceleration voltage of the electrons determines the wavelength of the electron beam, which in turn governs the resolution of the electron microscope. The electron beam after passing through the condenser lens system is directed towards a thin sample. Typically TEM specimen thickness is in the range of 50 to 100 nm for it to be electron transparent. The microscope column is maintained at high vacuum levels to prevent scattering of electrons by the atmosphere inside the microscope. The diffraction pattern and image are formed at the back focus plane and image plane of the objective lens. Information is obtained from both transmitted electrons (i.e. image mode) and diffracted electrons (i.e. diffraction mode). A transmitted beam combined with one or more diffracted beam gives a bright field image, whereas a dark field image is obtained from a transmitted beam alone or one of the diffracted beams. Some of the diffraction patterns are from a selected area of the specimen and these are known as selected area electron diffraction (SAED) patterns. High resolution requires both high instrumental resolving power and high image contrast. The technique in this case is termed as high-resolution transmission electron microscopy (HR-TEM). [22] A FEI TECNAI 3010 electron microscope operating at 300 kV (C_s = 0.6 mm, resolution 1.7 Å) was employed for high resolution transmission electron microscopy (HRTEM) measurements of all materials. Samples were crushed and dispersed in isopropanol before depositing onto a holy carbon grid.

2.3.2.4. UV-Visible Spectroscopy

UV-Vis reflectance spectroscopy is best method for characterizing optical and electronic properties of many different materials. The band gap (E_g) is an important feature of semiconductors which determines their applications in optoelectronics. [23] Kubelka-Munk theory helps to calculate the band gap of semiconductors from the diffuse reflectance spectra.[24] Originally they proposed a model to describe the behavior of light traveling inside a light-scattering specimen, which is based on the following differential equations:

$$-di = -(S + K)idx + Sjdx \tag{2.7}$$

$$dj = -(S + K)jdx + Sidx \tag{2.8}$$

where i and j are the intensities of light traveling inside the sample towards its un-illuminated and illuminated surfaces, respectively; dx is the differential segment along the light path; S and K are the so called K-M scattering and absorption coefficients, respectively. These last two quantities have no direct physical meaning on their own, even though they appear to represent portions of light scattered and absorbed, respectively, per unit vertical length. [25] This model holds when the particle size is comparable to, or smaller than the wavelength of the incident light, and the diffuse reflection no longer allows to separate the contributions of the reflection, refraction, and diffraction (*i.e.* scattering occurs). In the limiting case of an infinitely thick sample, thickness and sample holder have no influence on the value of reflectance (R). In this case, the Kubelka-Munk equation at any wavelength becomes:

$$\frac{K}{S} = \frac{(1 - R_\infty)^2}{2R_\infty} \equiv F\llbracket(R\rrbracket_\infty) \tag{2.9}$$

F (R_∞) is the so-called remission or Kubelka-Munk function, where $R_\infty = R_{sample} / R_{standard}$. [26] In the parabolic band structure, the band gap E_g, and absorption coefficient α of a direct band gap semiconductor are related through the well known equation [27]:

$$\alpha h\nu = C_1(h\nu - E_g)^{\frac{1}{2}} \tag{2.10}$$

where α is the linear absorption coefficient of the material, $h\nu$ is the photon energy and C_1 is a proportionality constant. When the material scatters in perfectly diffuse manner (or when it is illuminated at 60° incidence), the K-M absorption coefficient K becomes equal to 2α ($K=2\alpha$). In this case, considering the K-M scattering coefficient S as constant with respect to wavelength, and using the remission function in Eq. (2.10) we obtain the expression:

$$[F(R_{\infty})h\nu]^2 = C_2\,(h\nu - E_g) \qquad (2.11)$$

Therefore, obtaining $F\ (R_{\infty})$ from Eq. (2) and plotting the $[F\ (R_{\infty})\ h\nu]^2$ against $h\nu$, the band gap E_g of a powder sample can be extracted easily. The intensity of the absorption band depends on three factors namely (a) transition probability, (b) population of states and (c) concentration or path length. Almost all relationships between intensities of incident and transmitted radiation and the concentration and path-length is governed by Beer-Lambert's law which is written as

$$I - I_0 e^{-\kappa cl} \qquad (2.12)$$

$$\log\left(\frac{I_0}{I}\right) = A = \kappa cl \qquad (2.13)$$

where I = Intensity of the emitted radiation, I_0 = Intensity of the incident radiation, κ = constant, c = concentration and l = path length. A is known as the absorbance or the optical density and κ, the constant generally represented as ε, known as the molar absorption coefficient. Diffuse reflectance UV-Vis measurements of all materials were performed on a spectrophotometer (Shimadzu, Model UV-2550) with spectral grade $BaSO_4$ as the reference material.

2.3.2.5. Raman Spectroscopy

Vibrational spectroscopy is an excellent method for identifying substances by providing unique fingerprint spectra. Raman spectroscopy is one of the fastest and non-destructive analytical techniques that give the vibrational spectrum and physical or chemical information of many materials. Among all vibrational techniques, Raman spectroscopy appears as privileged method for the analysis in material science. In 1928, an Indian physicist Chandrashekhara Venkata Raman discovered the phenomena of inelastic scattering of light, known as the Raman effect. This explains the shift in wavelength of a small fraction of radiation scattered by molecules, having different frequency from that of the incident beam. [28] This shift in wavelength depends upon the chemical structure of the molecules responsible for scattering. Raman spectroscopy utilizes scattered light to gain knowledge about molecular vibrations which can provide information regarding the structure, symmetry, electronic environment and bonding of the molecule, thus permits the quantitative and qualitative analysis of the individual compounds. The irradiation of a molecule with a monochromatic light always results in two types of light scattering, elastic and inelastic. In elastic scattering, there occurs no change in photon frequency or without any change in its wavelength and energy. Conversely, the other is inelastic scattering which is accompanied by the shift in photon frequency due to excitation or deactivation of molecular vibrations in which either the photon may lose some amount of energy or gains energy. Thus, three types of phenomena can occur First, when light is incident on a molecule, it can interact with the molecule but the net exchange of energy (E) is zero, so the frequency of the scattered light is the same as that of the incident light ($E = E_o$). This process is known as Rayleigh scattering. Second, the light can interact with the molecule and the net exchange of energy is the energy of one molecular vibration. If the interaction causes the light photon to gain vibrational energy from the molecule then the frequency of the scattered light will be higher than that of the incident light ($E = E_o + E_v$), known as anti-Stokes Raman scattering. Third, if the interaction causes the molecule to gain energy from the photon then the frequency of the scattered light will be lower than that of the incident light ($E = E_o - E_v$), this process is known as Stokes Raman scattering. Raman spectra bring direct results of the analysis without sample preparation and easy interpretation of the results making it as a time saving and cost-effective technique. All the Raman spectra presented in the thesis were recorded on a Horiba JY LabRAM HR 800 Raman spectrometer coupled with microscope in reflectance mode with 633 nm excitation laser source and a spectral resolution of 0.3 cm^{-1}.

2.3.2.6. FT-IR Spectroscopy

Infrared spectroscopy (IR) is one of the most widely used techniques, and usually most effective method for characterisation of heterogeneous catalysts. This method permits us to monitor directly the interaction between the sorbed molecules and the catalysts. In case of nanosized materials FTIR gives information on their bulk and surface, and provide insight into the nanostructure of the material. In infrared spectroscopy, IR radiation is passed through a sample. Some of the infrared radiation is absorbed by the sample and some of it is passed through (transmitted). The resulting spectrum represents the molecular absorption and transmission, creating a molecular fingerprint of the sample. Like a fingerprint no two unique molecular structures produce the same infrared spectrum. This makes infrared spectroscopy useful for several types of analysis. This technique is mainly used to determine the nature of metal oxides (M-O bonds, OH groups), adsorption sites and acidity and basicity of catalysts (using probe molecules). An infrared spectrum represents a fingerprint of a sample with absorption peaks which correspond to the frequencies of vibrations between the bonds of the atoms making up the material. Because each different material is a unique combination of atoms, no two compounds produce the exact same infrared spectrum. Therefore, infrared spectroscopy can result in a positive identification (qualitative analysis) of different kind of material. FT-IR spectra presented in the thesis were recorded using a Shimadzu 8000 series FTIR spectrometer.

2.3.2.7. X-Ray Photoeletron Spectroscopy (XPS)

The physical and chemical composition of the catalyst surfaces determines the nature of the interactions. Their surface chemistry will influence factors such as corrosion rates, catalytic activity, adhesive properties, contact potential, and failure mechanisms. Surfaces, therefore, influence many crucially important properties of the solid. X-ray photoelectron spectroscopy (XPS) is based on the photoelectric effect discovered by Heinrich Hertz and explained later by Albert Einstein. [29] Each atom in the surface has core electron with the characteristic binding energy that is conceptually, not strictly, equal to the ionization energy of that electron. When an X ray beam directs to the sample surface, the energy of the X-ray photon is adsorbed completely by the core electron of an atom. If the photon energy, $h\nu$, is large enough, the core electron will then escape from the atom and emit out of the surface. The emitted electron with the kinetic energy of E_k is referred to as the photoelectron. The binding energy of the core electron is give by the Einstein relationship:

$$\boldsymbol{h}\nu = E_b + E_k + \Delta \qquad (2.14)$$

$$E_b = \boldsymbol{h}\nu - E_k - \Delta \qquad (2.15)$$

Where $h\nu$ is the X-ray photon energy (for Al Kα, $h\nu$ =1486.6eV); E_k is the kinetic energy of photoelectron, which can be measured by the energy analyzer; and Δ is the work function induced by the analyzer, about 4~5eV. Since the work function, Δ, can be compensated artificially, it is eliminated, giving the binding energy as follows:

$$E_b = \boldsymbol{h}\nu - E_k \qquad (2.16)$$

XPS is a widely used technique for obtaining chemical information of various material surfaces. The low kinetic energy ($0 \leq 1500$ eV) of emitted photoelectrons limit the depth from which it can emerge, so that XPS is a very surface-sensitive technique and the sample depth is in the range of few nanometers (<10 nm). Photoelectrons are collected and analyzed by the instrument to produce a spectrum of emission intensity versus electron binding (or kinetic) energy. In general, the binding energies of the photoelectrons are characteristic of the element from which they are emanated, so that the spectra can be used for surface elemental analysis. Small shifts in the elemental binding energies provide information about the chemical state of the elements on the surface. The peak area can be used (with appropriate sensitivity factors) to determine the surface compositions of the material. Therefore, the high-resolution XPS studies can provide the chemical state information of the surface. Once a photoelectron has been emitted, the ionized atom must relax in some way. This can be achieved by the emission of an X-ray photon, known as X-ray fluorescence. The other possibility is the ejection of an Auger electron through a secondary process. All the XPS data presented in the thesis were carried out on VG Microtech Multilab ESCA 3000 spectrometer using a non-monochromatized Mg Kα X-ray source (hν = 1253.6 eV). Selected spectra were also recorded with Al Kα x-ray (hν = 1486.6 eV). Base pressure in the analysis chamber was maintained around 5×10^{-10} Torr. Binding energy (BE) calibration was performed with Au $4f_{7/2}$ core level at 83.9 eV. The error in BE values reported is ± 0.1 eV. [30]

2.3.2.8. Energy Dispersive Analysis of X-ray (EDAX)

Energy Dispersive X-Ray Analysis (EDX), referred to as EDS or EDAX, is an x-ray technique used to identify the elemental composition of materials. This technique is used in conjunction with SEM or TEM. An electron beam with an energy in the range of 10-20keV strikes the surface of a conducting sample. These incident electrons knock out the inner core level electrons of the sample. The electrons from the higher energy levels fill up the vacancy thus created. During this transition X-ray is emitted which is plotted as no. of counts (intensity) with respect to the BE. The energy of the X-rays emitted mainly depends on the material under examination. The X-rays are generated in a region about 2 microns in depth, and thus EDX is not a surface science technique. By moving the electron beam across the material an image of each element in the sample can be acquired. Due to the low X-ray intensity, images usually take a number of hours to acquire. Elements of low atomic number are difficult to detect by EDX. The detector used in EDX is the Lithium drifted Silicon detector (SiLi). This detector must be operated at liquid nitrogen temperatures. When an X-ray strikes the detector, it will generate a photoelectron within the body of the Si. As this photoelectron travels through the Si, it generates electron-hole pairs. The electrons and holes are attracted to opposite ends of the detector with the aid of a strong electric field. The size of the current pulse thus generated depends on the number of electron-hole pairs created, which in turn depends on the energy of the incoming X-ray. Thus, an X-ray spectrum can be acquired giving information on the elemental composition of the material under examination. The SiLi detector (see below) is often protected by a Beryllium window. The absorption of the soft X-rays by the Be precludes the detection of elements below an atomic number of 11 (Na). In windowless systems, elements with as low atomic number as 4 (Be) have been detected, but the problems involved get progressively worse as the atomic number is reduced. [31] Elemental mapping works similarly to a scanning electron microscope: the sample is bombarded with an electron beam, and signals that come from the sample are collected. This enables the elements present within sample volumes of 10-30 cubic micrometers or less to be determined. EDAX measurements described in this thesis were performed on a on a SEM system equipped with EDX attachment (FEI, Model Quanta 200 3D). Samples for EDAX analysis were made by drop coating the solutions onto Si (111) wafers. In some cases, powder samples were also used directly on the sample-holder for the measurement. EDX spectra were recorded in the spot profile mode by focusing the electron beam onto specific regions of the sample. Calibration of the experiment for nitrogen estimation was measured with several mixtures of gallium nitride and alumina powder mainly to ensure the reliability of nitrogen estimation. However, materials composition reported is based on the data collected over large areas (>300 μm^2).

2.3.2.9. Photoluminescence spectroscopy

The phenomenon of re-emission of previously absorbed radiation (at relatively lower λ) is termed as luminescence. In photoluminescence, the molecules/atoms acquire higher energy excited state by absorption of photons of electromagnetic radiation, and then return to the ground state with emission of light. Thus, photoluminescence (PL) spectroscopy is concerned with the monitoring of light emitted from molecules/atoms.

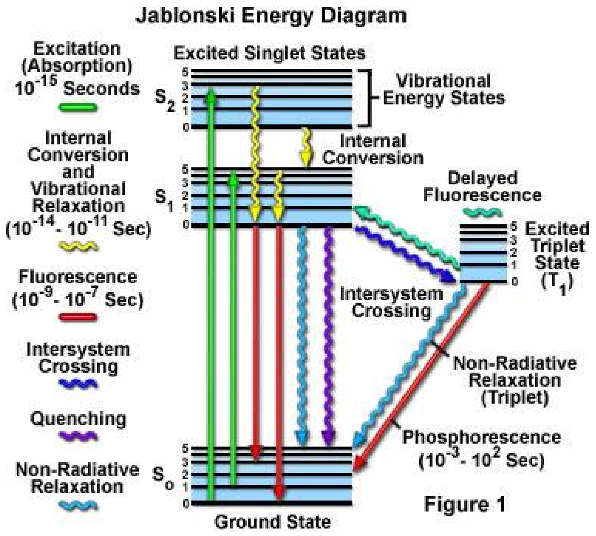

Figure 2.5: Jablonski diagram showing various electronic transitions

Fig. 2.5 shows a typical Jablonski diagram illustrating possible radiative and nonradiative emission processes in a general sample, with S1 or S2 a singlet and T1 a triplet electronic level over the ground state S0. This technique involves recording of the excitation and emission spectra of the sample at particular wavelengths. Excitation spectrum is first recorded to confirm the identity of the sample and to select the optimum excitation wavelength. Emission spectrum is then recorded at the selected excitation wavelength, which gives the intensity of the luminescence emission as a function of wavelength. PL measurements were performed using Horiba Jobin Yuon Fluorolog 3 spectrophotometer equipped with 450 W xenon lamp at room temperature under the excitation light of 280 nm. The conditions are fixed as far as possible in order to compare the photoluminescence signals directly.

2.3.2.10. Electrochemical impedance spectroscopy (EIS)

Electrochemical impedance spectroscopy (EIS) is a very versatile electrochemical tool to characterize intrinsic electrical properties of any material and its interface. This is a steady state method measuring the current response to the application of an ac voltage as a function of the frequency. [32] The basis of impedance spectroscopy is the analysis of the impedance (resistance of alternating current) of the observed system with respect to the applied frequency and applied signal. An important advantage of EIS over other techniques is the possibility of using tiny ac voltage amplitudes exerting a very small perturbation on the system. EIS provides quantitative information about the conductance, dielectric coefficient and some interfacial properties. Also this has been widely employed to study the kinetics of electrochemical and photoelectrochemical processes including the elucidation of salient electronic and ionic processes occurring in the DSC. EIS data for electrochemical cells are most often represented in Nyquist and Bode plots. Bode plots refer to representation of the impedance magnitude (or the real or imaginary components of the impedance) and phase angle as a function of frequency. Because both the impedance and the frequency often span orders of magnitude, they are frequently plotted on a logarithmic scale. Bode plots explicitly show the frequency-dependence of the impedance of the device under test. A complex plane or Nyquist plot depicts the imaginary impedance, which is indicative of the capacitive and inductive character of the cell, versus the real impedance of the cell. Nyquist plots have the advantage that activation-controlled processes with distinct time-constants show up as unique impedance arcs and the shape of the curve provides insight into possible mechanism or governing phenomena. The Nyquist diagram features typically three semicircles that in the order of increasing frequency are attributed to the Nernst diffusion within the electrolyte, the electron transfer at the oxide/electrolyte interface, and the redox reaction at the platinum counter electrode. [33] The impedance spectra of all materials in this thesis were made at room temperature using Autolab PGSTAT30 (Eco-Chemie). The frequency range chosen for the measurement was from 10^{-2} Hz to 10^{6} Hz with AC amplitude of 10 mV.

2.4. References

1. C. Perego and P. Villa, *Catal. Today* **34** (1997) 281.
2. H. C. Yi and J. J. Moore, *J. Mater. Sci.* **25** (1990) 1159.
3. K. Nagaveni, M. S. Hegde, N. Ravishankar, G. N. Subbanna, and G. Madras, *Langmuir,* **20** (2004) 2900.
4. M. Mapa and C.S. Gopinath, *Chem. Mater.,* **21** (2009) 351.
5. M. Mapa, K.S. Thushara, B. Saha, P. Chakraborty, C.M. Janet, R.P Viswanath, C.M. Nair, K.V.G.K. Murty and C.S. Gopinath, *Chem. Mater.,* **21** (2009) 2973.
6. M. Mapa, K. Sivaranjani, D. S. Bhange, B. Saha, P. Chakraborty, A.K. Viswanath and C.S. Gopinath, *Chem. Mater.*, **22** (2010) 565.
7. K. Sivaranjani, and C.S. Gopinath, *J. Mater. Chem.* **21** (2011) 2639.
8. A.S. Mukasyan, C. Costello, K.P. Sherlock, D. Lafarga and A. Varma, *Separ. Purif. Tech.*, **25** (2001) 117.
9. A.S. Mukasyan, P. Epstein and P. Dinka, *Proc. Combust. Inst.,* **31** (2007) 1789.
10. C-C. Hwang and T-Y. Wu, *J. Mater. Sci*., **39** (2004) 6111.
11. H. Guo, D. Li, D. Giang, W. Li and Y. Sun, *Catal. Lett*., **135** (2010) 48.
12. S. D. Yim, S. J. Kim, J. H. Baik, In-Sik. Nam, Y. S. Mok, J.-H. Lee, B. K. Cho and Se. H. Oh, *Ind. Eng. Chem. Res.*, **43** (2004) 4856.
13. K. Sivaranjani, S. Agarkar, S.B. Ogale, C.S. Gopinath, *J. Phys. Chem. C* **116** (2012) 2581.
14. K. Sivaranjani, A. Verma, C.S. Gopinath, C.S. *Green Chem.* **14** (2012) 461.
15. S. Muduli, W. Lee, V. Dhas, S. Mujawar, M. Dubey, K. Vijayamohanan, S-H. Han, S.B. Ogale, *ACS Appl. Mater. Interfaces*, **1** (2009) 2030.

16. H. P. Klug and L. E. Alexander, *X-Ray Diffraction Procedures: For Polycrystalline and Amorphous Materials*, (1974) p. 618 John Wiley and Sons,New York.

17. B. D. Cullity and S. R. Stock, Elements of X-ray Diffraction, Prentice Hall, Upper Saddle River, NJ 07458, 3rd ed. (2001).

18. P.W. Atkins, *Physical Chemistry*, Oxford University Press, London (1990).

19. B. C. Lippens and J. H. de Boer, *J. Catal*. **4** (1965) 319.

20. E. P. Barret, L. G. Joyner and P. H. Halenda, *J. Amer. Chem. Soc*. **73** (1951) 373.

21. M. Knoll and E. Ruska, *Physik,* **78** (1932) 318.

22. D.B. William and C.B. Carter, *Transmission Electron Microscopy*, Plenum Press, New York (1996).

23. A. E. Morales, E. S. Mora, and U. Pal, *Rev. Mex. Fís*. **53** (2007) 18.

24. P. Kubelka and F. Munk, *Z. Tech. Phys*. **12** (1931) 593.

25. L. Yang and B. Kruse, *J. Opt. Soc. Am. A* **21** (2004) 1933.

26. J. Torrent and V. Barrón, *Encyclopedia of Surface and Colloid Science.* (Marcel Dekker, Inc.: New York, 2002).

27. R.A. Smith, *Semiconductors*, 2nd ed. (Cambridge University Press: Cambridge, 1978).

28. C.V. Raman and R.S. Krishnan, Nature **121** (1928) 501.

29. (a) T. A. Carlson, *X-ray Photoelectron Spectroscopy*, Dowden, Hutchinson & Ross: Stroudsburg, PA, 1978. (b) Practical Surface Analysis, Vol. 1: Auger and X-ray Photoelectron Spectroscopy, 2nd ed., D. Briggs and M. P. Seah, Eds., Wiley, New York, 1990. (c) S. Hüfner, *Photoelectron Spectroscopy*, Springer- Verlag: Berlin, 1995.

30. (a) M. K. Dongare, V. Ramaswamy, C. S. Gopinath, A. V. Ramaswamy, S. Scheurell, M. Brueckner and E. Kemnitz, *J. Catal*. **199** (2001) 209. (b) V. L. J. Joly, P. A. Joy, S. K. Date and C. S. Gopinath, *J. Phys. Condens. Matt.* **13** (2001) 649.

31. http://www.uksaf.org/tech/edx.html.

32. Q. Wang, J-E. Moser, and M. Grätzel**,** *J. Phys. Chem. B***,** 109 (2005) 14945.

33. R. Kern, R. Sastrawan, J. Ferber, R. Stangl and J. Luther, J. *Electrochim. Acta*, 47 (2002) 4213.

Chapter 3

Characterization and Application of $TiO_{2-x}N_x$ in Photocatalysis and DSSC

3. Characterization and Application of $TiO_{2-x}N_x$ in Photocatalysis and DSSC

Synopsis

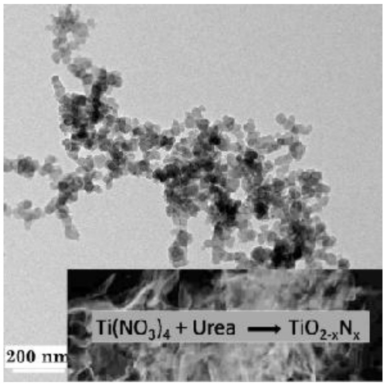

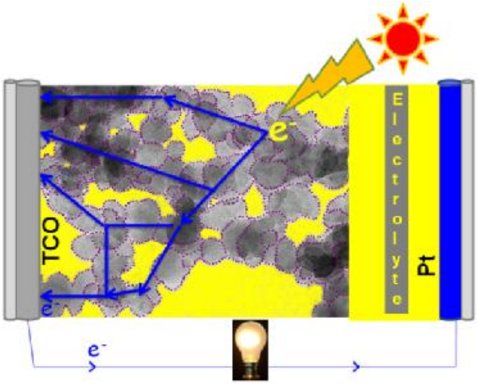

- $TiO_{2-x}N_x$ materials are prepared by simple solution combustion method within 10 minutes using Titanyl nitrate and urea as oxidizer and fuel respectively.

- Among all materials, UT10 (urea/Ti = 10) gives best activity for Rhodamine B degradation, Photocatalytic oxidation of p-anisyl alcohol under direct sunlight as well as with laboratory light source.

- Moreover, UT10 shows highest efficiency (6.9%) in dye sensitized solar cells.

- High photocatalytic and photovoltaic activity of UT10 is mainly attributed to pseudo 3D mesoporous nature, visible light absorption, high surface area, nanocrystalline particles and electrically interconnected nanoparticles.

- Likely the charge carrier recombination is very low with UT10 which gives the best activity.

Part A: Characterization of $TiO_{2-x}N_x$

3.1. Introduction

Generally, semiconductors (such as TiO_2, ZnO, Fe_2O_3, CdS, and ZnS) are suitable materials to be used as photocatalyst. Semiconductor materials are materials whose VB and CB are separated by an energy gap or band-gap. [1] When a semiconductor molecule absorbs photons with energy equal or greater than its band-gap, electrons in the VB can be excited into the CB, and thus charge carriers are generated. In order to have a photocatalyzed reaction, the e^-–h^+ recombination, subsequent to the initial charge separation, must be minimized. [2] Among all semiconductors, the most widely used semiconductor is titanium dioxide (TiO_2). In fact it is chemically and biologically inert, photocatalytically stable, relatively easy to produce and to use, able to efficiently catalyze reactions, cheap and without risks to environment or humans. [3] However TiO_2 is active only in UV light. There are constant efforts are going on in this field in order to make visible light active titania photocatalyst. It is universally accepted fact that nitrogen doping in titania reduces the band gap sufficiently and makes titania to absorb into the visible light regime.

In photocatalysis, the competition between the rate of charge carrier transport to the surface and the rate of electron-hole recombination decides the efficiency of the catalyst. [4, 5] Cao et al [6] demonstrated that the quantum sized particles displays the charge trapping process and it is faster than the recombinations, by accelerated transfer of these photogenerated electrons and holes from the bulk to the surface. Recombination is less in nanocrystalline TiO_2 compared to bulk and/or nanoparticle TiO_2 with a more amorphous nature. Hence we can prevent recombination by decreasing the particle size of titania, while retaining the high crystallinity. Hence, titania nano particles below 10 nm with anatase phase will act as an efficient photocatalyst. A combination of nano particle size with high crystallinity helps for faster diffusion of charge carriers to the surface without charge recombination. [7] If disordered mesoporosity, which requires lesser diffusion lengths of few nanometers, can be coupled with the above aspect, it would enhance the utilization of charge carriers for Photocatalysis. Since grain boundaries hinder transport and enhance recombination, [8] it is highly desirable to have an electrically interconnected nanoparticulate (EINP) material in a high surface area framework, such as a mesoporous system, to render high efficiency. The possibility of integrating visible light absorption, due to N-doping in TiO_2, along with above all aspects would enhance the efficiency of the sunlight harvesting capabilities for different applications. A combination of nanocrystallinity, high surface area in a disordered mesoporous framework, and EINP structure in a single material is expected to increase the charge carrier transport and hence influence efficiency (η) for a DSSC.

In this chapter, we report the preparation of meso $TiO_{2-x}N_x$ material through simple and cost effective solution combustion method (SCM) which has all the above discussed positive aspects such as, visible light absorption, mesoporosity, high surface area, electrically interconnected nano crystalline anatase phase and smaller particle size. Above aspects have been combined in one to make a better visible light active $TiO_{2-x}N_x$ material. Catalytic activity of the prepared material was measured by rhodamine B degradation and oxidation of aqueous p-anisyl alcohol to p-anisaldehyde under direct sunlight. Moreover $TiO_{2-x}N_x$ material shows a remarkable $\eta = 6.9\%$ without using any light harvesting protocols and this far exceeds the values reported thus far for wormhole meso-TiO_2 (<5%). Although the SCM is an exothermic process, high temperatures occur for only a few seconds which helps the growth of nanocrystalline titania particles from nascent titanium oxo (Ti_xO_y) clusters. Textural properties of the final material could be varied systematically by altering the oxidizer/fuel ratio.

3.2. Results and Discussion

3.2.1. Powder X-ray diffraction

Figure 3.1 shows PXRD pattern of all $TiO_{2-x}N_x$ materials. XRD pattern consists of a set of narrow and intense features and another set of broad features with relatively less intensity. A comparison with the standard anatase and rutile phases (JCPDS File 21-1272, 21-1276 respectively) [9] clearly indicating the broad features are entirely due to anatase and narrow features are due to rutile.

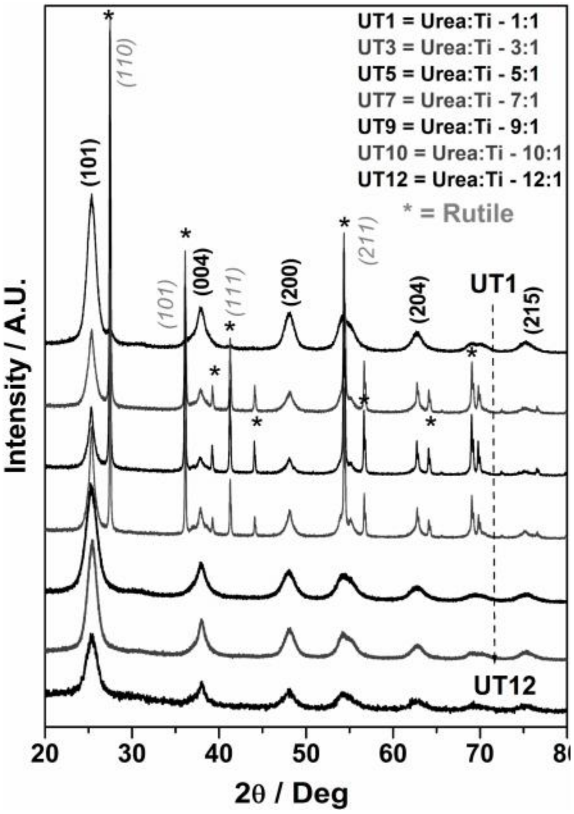

Figure 3.1: Powder XRD pattern of mesoporous $TiO_{2-x}N_x$ prepared with different urea/titanyl nitrate ratio.

The presence of anatase phase is observed for highest (UT9, UT10 and UT12) urea containing starting compositions. Intermediate ratio (UT3-UT7) materials show the mixture of anatase and rutile phases and UT1 exhibits predominantly anatase phase. Among all materials, UT10 and UT12 shows 100% anatase phase. It is a well known fact that the ratio of anatase:rutile phase depends on the temperature. Among two phases of titania, rutile phase is thermodynamically more stable. Indeed, high combustion temperatures (>600^0C) lead to increasing amount of rutile phase. Maximum temperature generated under combustion conditions is strongly dependent on the fuel to oxidizer ratio. When the above ratio is lesser than or equal to the stoichiometry value (1.67) less combustion temperature was observed due to flameless or smoldering type combustion. [10-12] When the urea/oxidizer ratio is higher than the stoichiometry (UT3 to UT7) value voluminous type of combustion occurs and hence high temperature is generated. Further increase in the fuel content (UT9, UT10 and UT12) again leads to flameless combustion due to low concentration of oxidizer. In this case, the combustion reaction is partly supported by the ambient air and the reaction rate is limited by the diffusion of oxygen. Therefore only intermediate ratios have more rutile content. Above observations of different percentage of anatase/rutile (Table 1) indicating a non-uniform (uniform) thermal conditions generated during SCM, for intermediate (high) fuel/oxidizer ratio UT3-UT7 (UT9 and UT10) starting compositions. Among all of the $TiO_{2-x}N_x$ materials, UT5 exhibits the largest amount (57%) of rutile phase. More urea or oxidizer produces more gaseous by products such as CO_2, NH_3, NO_2 while decomposition, which prevents the grain growth [13] of titania particles. Also these gases prevent dense packing of the particle and results in anatase phase. [14] Therefore UT10 and UT12 gives 100% anatase phase with smaller crystallite size. Percentage of anatase phase, crystallite size calculated from XRD and bulk nitrogen content measured from EDX for different materials are shown in Table 3.1. The percent crystallinity were calculated from the XRD data by integrating all the peak areas and the same are listed in Table 3.1. Same amount of materials was used and the XRDs were recorded under identical conditions. The maximum crystallinity observed with UT10 is *assumed* to be 100 % and the percent crystallinity of other materials is calculated with reference to that.

Figure 3.2 shows the low angle XRD pattern of $TiO_{2-x}N_x$ materials. Mesoporous nature of the simple combustion synthesized materials (UT1, UT9, UT10 and UT12) was confirmed by the low angle XRD.

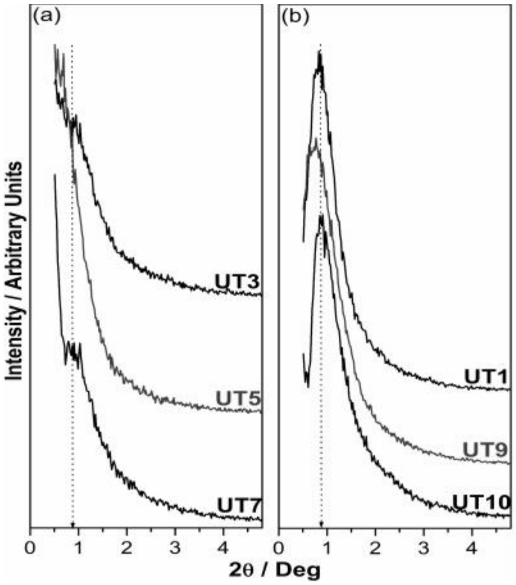

Figure 3.2: Low angle XRD recorded for mesoporous $TiO_{2-x}N_x$ materials. Panel a shows diffractorgram from UT3, UT5 and UT7, which are not mesoporous and contains rutile phase. Panel b shows mesoporous nature in UT1, UT9, UT10 and UT12 containing anatase phase.

Only one peak was observed around $0.8\text{-}0.9^0$ without any additional peaks indicating the presence of disordered mesoporosity. Unlike the regular mesoporous materials, like MCM-41,[15,16] no other low angle peaks were observed highlighting the mesoporous nature is likely due to an intergrowth of fundamental particles. The intergrowth of small primary particles results in aggregates with significant extra-framework void space, which is further confirmed by N_2 adsorption isotherms discussed later and it is due to wormhole-like mesoporous structure. [17] Extent of mesoporosity decreases in the intermediate ratio materials (UT3, UT5, UT7), which contains more rutile phase. It is observed that mesoporosity is inversely proportional to the rutile content. It is to be noted that rutile phase is densely packed (D = 4.24 g/cm^3) than the anatase phase (3.9 g/cm^3), which might be a reason for the loss of mesoporosity in the above materials.

Table 3.1: Physicochemical properties of as synthesized UTx materials

Material	Anatase Content (%)	BET surface area (m^2/g)	Pore size (nm)	Pore volume (cc/g)	Anatase Crystallite size (nm)	N-content (%)		Crystallinity (%)
UT1	94	160	3.9	0.18	15.3	2.2	1.2	-
UT5	43	57	6.2	0.10	12.1	7.3	3.1	-
UT9	98	175	4.7	0.30	9.2	8.1	5.0	92
UT10	100	234	7	0.44	6.8	9.2	6.7	100
UT12	99	230	6.8	0.38	5.9	8.9	7.0	79

3.2.2. EDX

Nitrogen content in $TiO_{2-x}N_x$ materials were analyzed by EDX. [18] EDX spectra of all materials are shown in Figure 3.3. Peak observed around 0.40 keV confirms the presence of nitrogen. Table 3.1 shows the bulk nitrogen content obtained from EDX analysis. Generally nitrogen content increases linearly with urea content and this has been confirmed by the increase in the intensity of nitrogen peak in EDX spectra. An interesting observation is the correlation between the nitrogen content observed by XPS as well as EDX which shows a similar trend. Although XPS measurements provide the surface N content, there is good agreement with the EDX results hinting the availability of more N on the surface. Thermogravimetric analysis of the $TiO_{2-x}N_x$ materials show weight loss due to desorption of water below 180 ^{0}C and no other loss features at high temperatures hinting that carbon impurities are very low, and supporting the clean combustion with urea in the preparation procedure.

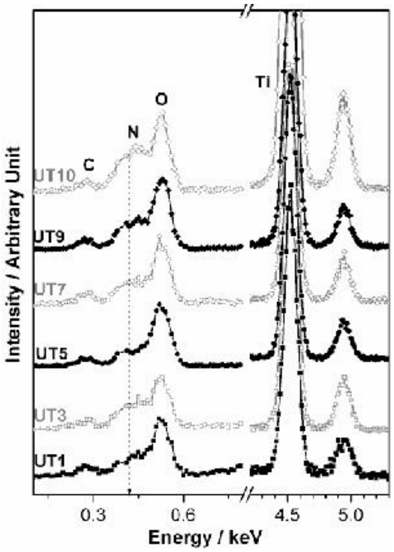

Figure 3.3: EDX patterns recorded for mesoporous $TiO_{2-x}N_x$ materials. The N peak in all samples confirms the N-doping, irrespective of the amount of urea used.

3.2.3. TEM

Particle morphology of $TiO_{2-x}N_x$ has been studied by HRTEM carefully. HRTEM images recorded for UT1, UT9 and UT10 materials are shown in Figure 3.4. A disorderd mesoporous structure can be observed in both materials. Disordered mesoporosity arises due to intergrowth of fundamental particles and the same leads to aggregates with significant extra framework void space. This is also consistent with textural mesoporosity observed in N_2 adsorption isotherms, discussed in the next section. These results are consistent with low angle X-ray diffraction data (see Fig. 3.2). Similar types of images have already been observed by Yu et al. for wormhole type phosphate mesoporous titania prepared by using co-block polymers as a template. [19] Selected-area electron diffraction (SAED) pattern confirms the crystalline nature of the prepared mesoporous materials and also it shows the anatase phase in all materials. HRTEM image shows the majority of lattice fringes corresponding to (101) ($d_{(101)}$ = 0.352 nm) crystallographic planes of anatase phase and the particle size of UT10 is around 7 nm which agrees well with the XRD results. Intergrown fundamental particles also ensures that they are electrically connected, which is necessary for charge transfer across particle such connectivity extends up to *several nm.* Porosity through interconnected nanoparticles (INP) is clearly visible from the TEM images indicating INP. Indeed such images are observed with different batches of UT10 materials prepared hinting the intrinsic nature of the connectivity. The rectangular area in Fig. 3.4c and 3.4d shows the alignment of crystallites with (101) facets (enlarged rectangular area are shown in Fig. 3.4e and f for better clarity). These observations critically support the qualitative EINP nature, particularly for UT10. It is to be noted the EINP and the same extending over micron scale length is observed with as prepared UT10 material, and the same is expected to enhance the diffusion of charge carriers to the surface. In contrast to the observations made for UT10, HRTEM image of UT9 shows isolated titania crystallites in Fig. 3.4g. Further within a group of particles, the interconnectivity between the particles is not as good as UT10. Although the preparation conditions are same, except for reactants ratio, the above marked difference reflects in the porosity and textural properties. It is expected that good crystallinity associated with nanoparticles enhances the light harvesting properties by increasing the mobility of charge carriers as well as minimizing the defects. Indeed the disordered mesoporous nature reduces the diffusion length of charge carriers, since the depth/length of mesopores are minimum to few nanometers, unlike several hundred nanometers in conventional mesoporous materials, like SBA-15. This disordered wormhole like framework provides an easy route for the diffusion of reactants due to less diffusion barriers. A similar concept has been invoked by Kim et al [20] and Zhang and Pinnavaia. [21] Unlike regular mesoporous material, like MCM-41, SBA-15 where the diffusion of reactants/products is large, the extent of diffusion is minimized in such disordered mesoporous materials. This is an added advantage for the fast diffusion of charge carriers in photocatalysis, which have a finite but short lifetime.

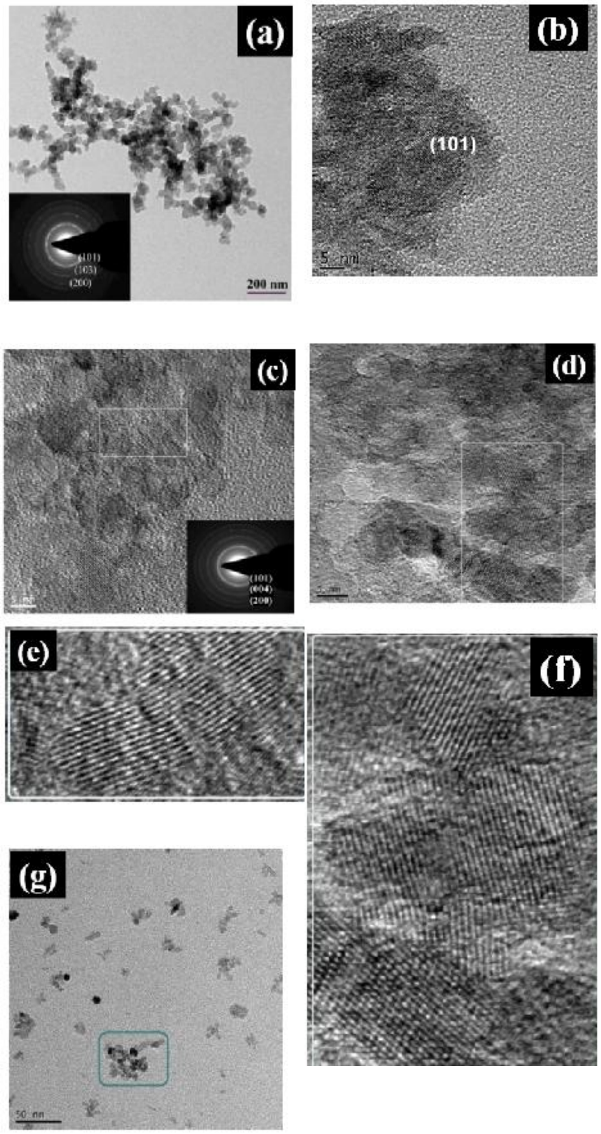

Figure 3.4: TEM image for (*a* and *b*) UT1, and (*c* and *d*) UT10 materials. Even though crystallite size is small, highly crystalline nature is evident from electron diffraction (inset in *a* and *c*) and d-value measured for preferentially oriented (101) planes. Rectangle area in *c* and *d* are expanded in panels *e* and *f*, respectively, to show the alignment of crystallites with (101) facets. (*g*) HRTEM image of UT9 shows not-so-well-connected particles.

3.2.4. N_2 adsorption isotherm

Textural properties of meso $TiO_{2-x}N_x$ materials have been studied by N_2 adsorption-desorption isotherms at 77 K. Figure 3.5 shows the results obtained from N_2 adsorption-desorption isotherm studies and analyzed by BET method for surface area and BJH pore size distribution. The surface area and porosity have been measured for all of the materials and the results are given in Table 3.1. UT1, UT9, UT10, UT12 materials shows type IV adsorption isotherm [22] which is typical for mesoporous materials. UT1 and UT9 shows H_2 type hysteresis [23] loop with a pore dia in the range of 4-6 nm. Relatively sharp desorption curves observed for UT1 and UT9 indicate the presence of bottle-neck like mesopores, and it is fully supported by adsorption-desorption isotherms. Large contribution of higher (lower) pore size, within 4-6nm, is evident with UT9 (UT1). However, UT10 shows H_3 type hysteresis loop which does not level off even at the saturation vapour pressure ($P = P_0$), is characteristic of the mesoporous materials arise through the agglomeration of nano particles with slit shaped pores. The extent of the mesoporosity is insignificant in UT5. Although mesopores contribution could be observed in Figure 3.5b for UT5, overall pore volume measured is 0.1 cc/g, indicating the contribution from mesopores is small. Less mesoporosity in UT5 may be attributed to large size of the densely packed rutile phase titania particles. Average pore size increases as the urea content increases from UT1 to UT12. Both pore size and number of pores increases simultaneously for UT10. Among all, UT10 shows the highest surface area (234 m^2/g) and pore volume (0.44 cc/g) due to well developed mesoporosity and smaller average crystallite size. High surface area generally enhances the light harvesting ability of the photocatalyst. [24,25]

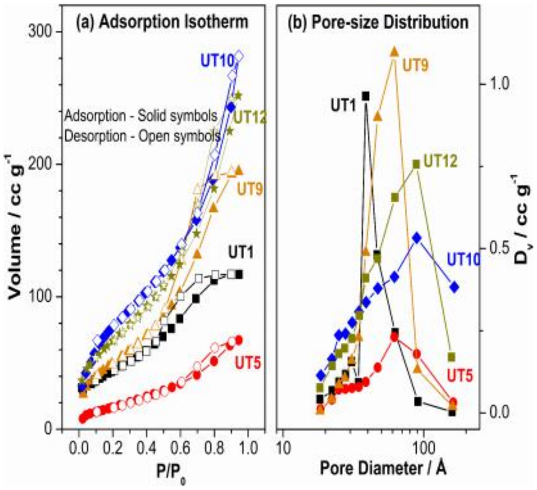

Figure 3.5: (a) N_2 adsorption-desorption isotherm studies, and (b) pore size distribution measured from the above isotherms of mesoporous $TiO_{2-x}N_x$ materials.

3.2.5. Raman Spectroscopy

Figure 3.6 shows the Raman spectra of $TiO_{2-x}N_x$ materials. Raman spectroscopy is

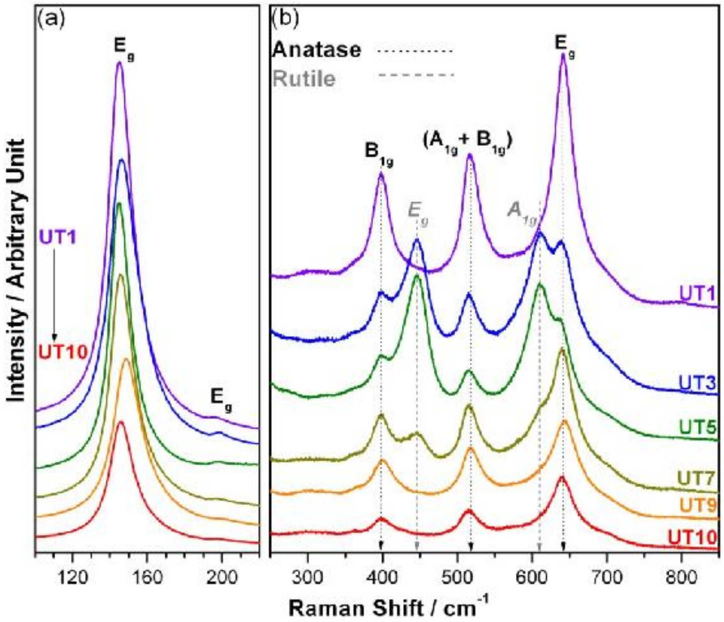

Figure 3.6: Raman spectra of meso $TiO_{2-x}N_x$ materials. Anatase and rutile features were indicated by dotted and dashed arrows, respectively.

extremely helpful for phase identification especially with TiO_2. Like XRD, Raman spectra also exhibit the presence of anatase + rutile phases in UT3-UT7 materials. There are six Raman active fundamental phonon modes observed at 145 (E_g), 198 (E_g), 398 (B_{1g}), 516 (A_{1g} + B_{1g}), 640 (E_g) cm^{-1} (dotted arrows in Figure 6b) for anatase titania. Four Raman active phonon modes for rutile phase are observed at 144 (B_{1g}), 446 (E_g), 610 (A_{1g}), 827 (B_{2g}) cm^{-1} (dashed arrows in Figure 3.6b). [26-29] The highest amount of rutile phase present in UT5 is evident from Figure 3.6. In fact most intense and sharp rutile features are observed for UT5, is in good agreement with XRD data. B_{1g} phonon mode at 144 cm^{-1} for rutile was observed for UT5 with low FWHM (13 cm^{-1}) supporting the highest rutile content in UT5. Broadening of the peaks confirms the presence of nano size titania particles. [9] Intensity of all of the peaks decreased when urea/oxidizer ratio increases from UT1 to UT10. Although UT1, UT9 and UT10 contains mostly anatase, intensity of all the phonon modes decreased drastically emphasizing two factors namely (a) the breaking of symmetry due to N-introduction into TiO_2 lattice, [9] especially in UT9 and UT10, and (b) a overall reduction in particle size from UT1 to UT10. This is further clearly visible in the E_g peak observed at 145 cm^{-1} (Figure 3.6a). The width of all the peaks is broadened due to quantum size confinement effect and therefore this small shift is not clearly visible in $TiO_{2-x}N_x$ materials. Importantly, increase in mesoporosity, and wider pore size range observed with UT9 and UT10 curtails the long range ordering. Although UT10 is fully anatase, due to the above reasons the intensity of Raman features are very small.

3.2.6. UV-Visible Spectroscopy

It is well known that the band gap of pure anatase phase titania is around 3.2 eV. The change in electronic property, especially the optical band gap due to nitrogen doping, [30-32] was clearly observed in UV-vis absorption spectra for $TiO_{2-x}N_x$ materials shown in Figure 3.7. Absorption cut-off for $TiO_{2-x}N_x$ materials varies between 2.90 eV for UT5, 3.24 eV for UT10. UT1 shows a band gap of 3.08 eV. Nitrogen doping gives visible light absorption in all of the materials. It is to be noted that although no distinct absorption band observed in the visible light regime, visible light absorption is observed with finite intensity up to 525 nm. As urea content increases, the visible light absorption also increases with the formation of rutile phase (UT5). Nonetheless UT10 is pale yellow in color and exhibits a blue shift (3.24 eV) compared to all other materials (UT1 to UT9). Though UT10 shows visible light

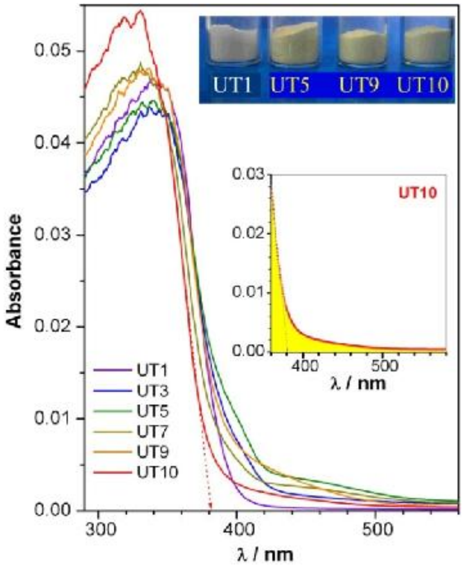

Figure 3.7: UV-Vis spectra of mesoporous $TiO_{2-x}N_x$ materials. Top inset shows a photograph for the pale yellow colour with materials.

absorption the observed blue shift is due to the smaller particle size and quantum size effects play a major role in UT10. [31, 33] Significant amount of N-content along with visible light absorption, up to 525 nm, and nanocrystallite size of $TiO_{2-x}N_x$ indicating a significant amount of nitrogen doping in the surface states. A photograph of UT1, UT5, UT9 and UT10 materials (Figure 3.7 – top inset) shows the change in color from colorless for UT1, to yellow for UT9 to pale yellow for UT10. Probably this is the first time that pale yellow color has been observed with a band gap of 3.24 eV corresponding to the UV regime for UT10. In fact UT10 exhibits the maximum visible light photocatalytic activity, and the same is to be discussed in the last section.

3.2.7. X-ray Photoelectron Spectroscopy

X-ray photoelectron spectroscopy (XPS) analysis was carried out to explore the nature of surfaces of UTx materials. Figure 3.8 shows XPS recorded for (a) Ti 2p and (b) N 1s core levels of UT1, UT5, UT9, UT10 and UT12 materials. Ti $2p_{3/2}$ core level in pure titania appears around 459 eV. [31, 32] The BE value of Ti $2p_{3/2}$ for UT1, UT5, UT9 and UT12 is also observed close to 459 eV. Nevertheless BE of Ti $2p_{3/2}$ for UT10 is observed at 457.6 eV. A substantial decrease in the BE value of Ti $2p_{3/2}$ in UT10 shows that there is an increase in electron density around Ti. Further, normal as well as grazing angle XPS of UT10 match with each other highlighting very similar electronic states of surface layer and top 5 nm of the crystallites.

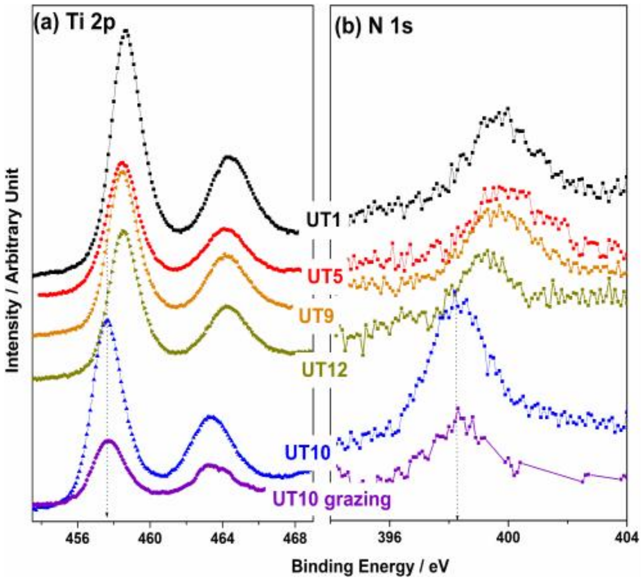

Figure 3.8: XPS spectra collected from (a) Ti 2p, and (b) N 1s core levels of mesoporous $TiO_{2-x}N_x$ materials. Note a systematic decrease in binding energy of both Ti 2p and N 1s core levels from UT1 to UT10.

This is attributed to the substitution of less electronegative nitrogen atom in the place of oxygen. Hence electron density around Ti ion increases and leads to formation of more Ti^{3+} which leads to lower BE for Ti 2p core level in UT10 material. Although there is a shift in BE there is no change in peak width of UT10, compared to other materials, indicating a overall decrease in BE and hence a change in electron density on Ti. O 1s core level also displays similar changes. UT10 exhibits O 1s peak at 528.7 eV while other UTx show the same at 529.8 eV. This is attributed to two factors. Primarily the un-saturation occurs on UT10, compared to other UTx materials, due to the EINP and textural properties discussed earlier leading to an increase in the effective electron density on the surface. [34,35] Secondary effect due to substitution of less electronegative N in the TiO_2 lattice also might contribute to higher charge density.

N 1s core level BE value also decreases from around 399.5–400 eV for UT1 to UT9 to 398.3 eV for UT10. N 1s BE observed at 398.3 eV in UT10 material is attributed to the N-Ti-O linkage corresponding to anion like nitrogen in TiO_2 lattice. [31] Indeed Sathish et al. observed 398.2 eV for nanocrystalline N-doped TiO_2 and attributed this to the N–Ti–O environment; it is also to be noted the above N-TiO_2 was prepared by a different route. Various research groups reported different BE value for N 1s core level between 397 and 404 eV, and it was mainly due to different preparation methods adopted by them. [36] From nitride type nitrogen 397.0 eV [30] to hyponitrite type nitrogen at 404 eV [37] has been reported for N-TiO_2 and the consensus is more towards anionic nitrogen. [36] Higher BE value observed for UT10 is likely due to the presence of more electronegative oxygen atom in the surrounding. It is commonly accepted that 2p orbital of nitride and oxy nitride type of anionic nitrogen could overlap with O 2p valence band and will reduce the energy gap efficiently. [38] This BE value indicates that UT10 along with high crystallinity and better porosity differs electronically also from other UTx materials. These factors might increase the effective electron transfer between particles in mesoporous framework of UT10.

3.2.8. Impedance measurements

Impedance measurements were made to explore the resistance values for different interfaces in the DSSC assembly, and the resulting Nyquist plots [39] are shown in Figure 3.9. As the electrolyte and counter electrode are the same in all the materials, our primary interest is in the second semicircle (Z2) which focuses on the TiO_2|Dye|electrolyte interface. The resistance R_k, i.e., the diameter of the central arc which gives the charge transfer resistance including recombination of electrons with I_3^- at the TiO_2|electrolyte interface is minimum

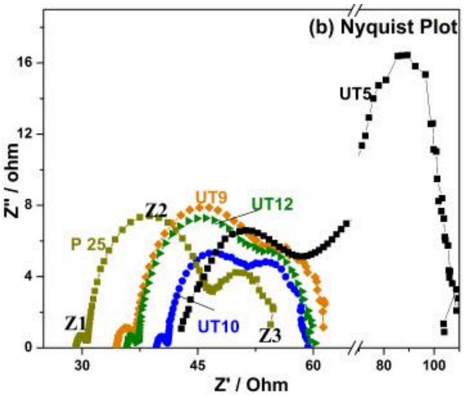

Figure 3.9: Electrochemical impedance spectra of DSSC made from P-25 and UTx materials.

(10.05 Ω) for UT10, while 15.9, 46.8, 17.74 and 18.15 Ω for P-25, UT5, UT9 and UT12 respectively. Con value is also calculated which describes the charge transport resistance and its recombination rate along the entire thickness of the working electrode and is equal to R_k L k_{eff}, [40] where, L is thickness of the film. Con value for UT5, UT9 and UT12 is 31.9, 6.8 and 10.1 Ω cm/s, respectively. This value is substantially low for UT10 which is 5.6 Ω cm/s. This all indicates that UT10 has the property of efficient charge transfer within its network as compared to UT9 and UT12. In other words, charge storage capacity has decreased in the case of UT10 than all others (height of Z2, Figure 3.9). This also suggests a good necking between the individual particles in UT10 confirming EINP, as seen in TEM images. The number of defect states in other materials are relatively high and they act as trapping sites for electrons thereby enhancing the capacitance and decreasing the J_{sc} (Table 3.2). It is to be noted that the thickness of meso UTx films prepared for photovoltaic measurements is ~12 μm and the EINP extending, at least, up to 1 μm demonstrates a minimum defects with UT10. Very high Con and R_k value measured for UT5 suggesting a poor connectivity between crystallites, and the bigger crystallite size rutile apparently hinders the charge transfer and hence a overall low η.

3.2.9. Current-perpendicular-to-plane (CPP) conductivity measurements

Current-perpendicular-to-plane (CPP) conductivity measurements were performed on UTx films before dye loading (i.e. after annealing at 450 ^{0}C) using aluminum top electrode. The voltage was swept from 0 to 10 V with a step size of 0.5 V, and a delay time of 0.5 s. The results of these measurements are summarized in Fig. 3.10. It is observed that the current is significantly higher for UT10 film than the UT12 and UT9 films. It is mainly due to the presence of better connectivity between the UT10 nanoparticles. This observation confirms the proposed EINP nature of UT10 material. Very poor CPP conductivity observed for UT5

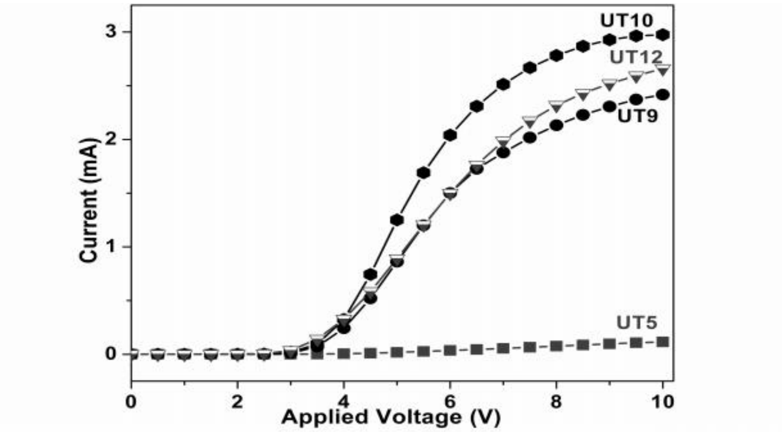

Figure 3.10: Current perpendicular to plane (CPP) transport data for UTx materials.

further reiterates the interpretation that large rutile content with low surface area and missing EINP do not favour high η.

Part B: Photocatalytic and Photovoltaic applications of $TiO_{2-x}N_x$

3.3.1. Rhodamine B degradation under direct sunlight

In order to evaluate photocatalytic oxidation ability of all the catalysts, rhodamine B degradation was carried out under direct sunlight as a model reaction. [41] Figure 3.11a shows the UV-vis absorption spectra recorded for Rh-B solution that was irradiated with direct sunlight for different time periods with UT10.

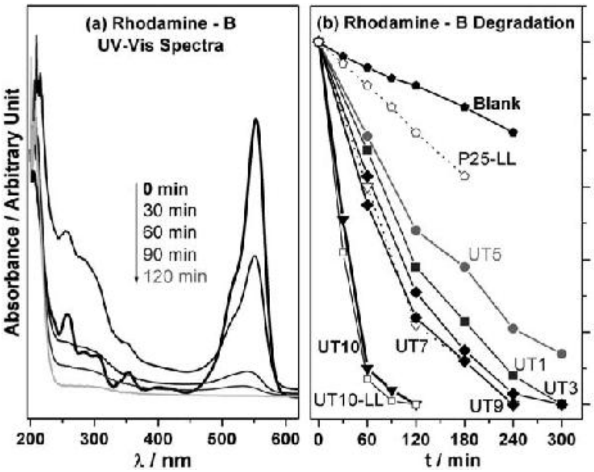

Figure 3.11: (a) UV-vis absorption spectra of rhodamine B degradation with UT10 catalysts at regular time intervals. (b) Photocatalytic degradation of rhodamine B with $TiO_{2-x}N_x$ catalysts under direct sunlight.

An exponential decrease in dye degradation is evident from the decrease in absorption co-efficient in first 60 min. Figure 3.11b compares the catalytic activity of all catalysts for Rh-B degradation. Experiments carried out with laboratory light (LL) source (λ > 420 nm) is also given for UT10 and P25.Among all catalysts, UT10 shows the best activity. Indeed, 90% of dye degradation occurs within 1 h with UT10 catalyst under direct sunlight as well as LL source. This underscores the visible light activity associated with UT10.The activity of all other catalysts follows the order given below; UT10 > >UT9 > UT7 > UT3 > UT1 > UT5. UT10 has unique properties like 100% anatase phase, smaller particle size (7 nm), and mesoporosity with higher surface area. Anionic like nitrogen present in UT10 catalyst is the reason for visible light absorption. Higher surface area enhances the absorption of more reactant molecules on the titania surface. Due to the highly crystalline but smaller particle size, the photo generated carriers diffuses fast to the surface and reacts rapidly with the adsorbed dye molecules and hence an effective utilization of charge carriers, especially holes for oxidation. Wormhole mesoporous nature of the catalyst decreases diffusion length of the charge carriers to the active sites and increases the rate of degradation. These features make UT10 to acts as a more active candidate for dye degradation reactions. UT5 shows very low activity and it is to be noted that it contains more rutile content and exhibit very low surface area. Low surface area leads to poor adsorption of reactant molecules and results in low activity. Photocatalytic activity measured on P25 with LL source shows poor activity for known reasons, such as no absorption in the visible light and low surface area (50 m^2g^{-1}). Results and discussion given in this section underscores the photocatalytic activity is essentially due to visible light absorption and that the small amount of UV present in sunlight plays no significant influence in the activity of $TiO_{2-x}N_x$ catalysts.

3.3.2. Photocatalytic Oxidation

Photocatalytic selective oxidation [42] of alcohol to aldehydes is one of the important reactions in organic synthesis. Para anisaldehyde is an important intermediate for the synthesis of drugs in pharmaceuticals and it is also used in perfumes. Photocatalytic oxidation is an economically viable route as well as green chemistry approach to prepare p-anisaldehyde. Photocatalytic oxidation [43] of p-anisyl alcohol was carried out with 20 mg of UT10 catalyst in aqueous solution under direct sunlight as well as with laboratory sources and the results are given in Fig. 3.12 and Table 3.2. Previously the same reaction was carried out by Palmisano et al. [44] and Yurdakal et al [45] under UV light in the presence of

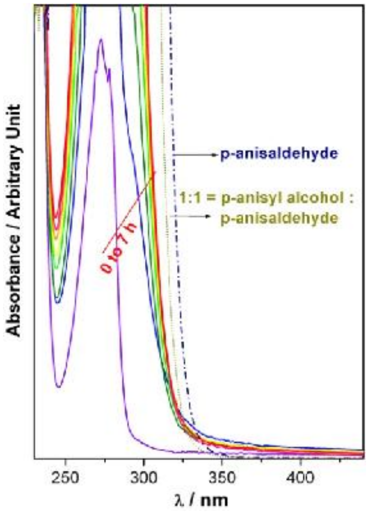

Figure 3.12: UV-visible absorption spectra recorded for the evolution of p-anisaldehyde from 4-anisyl alcohol by photocatalytic oxidation with UT10 catalyst in aqueous solution under direct sunlight.

Table 3.2: Para-anisaldehyde yield (in mol %) due to photocatalytic oxidation with UT10[a]

Time (hr)	Direct Sunlight	Laboratory light source (> 420 nm)
1	7.6	9.1
3	19.2	22.4
5	23.5	27.1
7	25.3	30.2
7.7	-	41.5[a]

[a] Yield reported by Palmisano et al.[44] under near-UV $\lambda = 360$ nm) irradiation conditions at room temperature with oxygen bubbling.

continuous bubbling of oxygen gas. In the present investigations the same reaction was carried out under direct sunlight in a static condition and without bubbling any oxygen. For comparison purposes the same reaction has been carried out under stirring in a laboratory visible light reactor ($\lambda > 420$ nm), but again without bubbling oxygen. p-Anisaldehyde formation from p-anisyl alcohol was confirmed both by UV-Vis absorption spectra and GC analysis. Fig. 3.12 shows the UV-vis absorption spectra for the reaction mixture at different time intervals. Dashdot line shows the UV-vis absorption spectrum of pure p-anisaldehyde. Continuous red shift occurs toward the product absorption onset as a function of irradiation time indicating the product formation. With reference to standard p-anisaldehyde, GC analysis shows only one peak at the same retention time and confirms that the product formed with 100% selectivity. 25 mol % conversion was observed with UT10 catalyst under direct sunlight within 7 h (10 am to 5 pm). Under LL source conditions a significantly higher rate of oxidation (30 mol %) was observed in the same experimental time. The above experimental observations again highlight the visible light activity associated with UT10. It is also to be noted that p-anisyl alcohol and p-anisaldehyde does not exhibit any absorption band in the visible light regime and is stable in visible light. Negligible p-anisyl alcohol oxidation (~1.5%) was observed over a period of 6 h in direct sunlight but without catalyst. Only photocatalytic oxidation could have transformed the reactant to product and has been further confirmed by the above blank reaction without any catalyst. Our results are also compared to those reported by Palmisano et al. [44] in Table 3.2 with their highest performing catalytic activity at near UV (ʎ ~ 360 nm) under continuous oxygen bubbling. It is to be noted that the reaction conditions employed, including catalyst surface area (235 m^2g^{-1}), are highly comparable in the present investigation to that of ref. [45], except for UV light and oxygen bubbling employed in ref. 48. In spite of the absence of oxygen bubbling an impressive yield of 25–30 mol % of p-anisaldehyde observed with visible light source in 7 h is a significant improvement. Usage of the least crystalline anatase titania which gave the highest activity compared to the good nanocrystalline anatase in the present investigations is a main difference. Rutile TiO_2 with a surface area of 107 m^2g^{-1} have been used by Yurdakal et al [45] in performing the partial oxidation of benzyl alcohol and p-anisyl alcohol to aldehydes and p-anisaldehyde, respectively, in water. As above in another work, [44] poorly crystalline rutile phase gave the highest selectivity of p-anisaldehyde. The effect of crystallinity towards photocatalytic reactivity is an interesting subject worth exploring further. However we believe that the charge utilisation might be playing the most significant role towards photocatalytic activity with $TiO_{2-x}N_x$ materials compared to the other factors.

Table 3.3. Photovoltaic properties of mesoporous $TiO_{2-x}N_x$ (UTx) materials

Sample code	Dye amount μmolcm^{-2}	V_{oc} (V)	J_{sc} (mA /cm^2)	FF (%)	η (%)
TU9	108	0.73	11.7	65.6	5.5±0.1
TU10	122	0.77	15.2	59.7	6.9±0.2
TU12	114	0.73	11.7	62.9	5.4±0.1
TU5		0.80	5.3	71.0	2.9±0.1
P-25	50	0.69	10.0	65.0	4.7±0.1
Grätzel Cell[a]		0.74	20.05	0.77	11.5

[a] This is the highest η achieved so far in DSSC .

3.3.3. Photovoltaics

Figure 3.13 shows the photocurrent-voltage (*I*-*V*) characteristics of the DSSCs made of different photoanodes prepared with anatase UTx materials and compared with Degussa P25 and mixed-phase UT5. Photovoltaic properties (open circuit voltage (V_{oc}), short circuit current (I_{sc}), fill factor (FF) and η are given in Table 3.3. UT9, 10 and 12 materials show η > 5% indicating the efficacy of SCM. Disordered mesoporosity with high surface area is the major reason for higher η of UTx (x≥9). In addition, high J_{sc} and marginally higher V_{oc} values of UT10 help to achieve the highest η, compared to UT9 and UT12. This is attributed to the EINP and the highest crystallinity with UT10, apart from mesoporosity. Better textural properties present in UT10 enhance dye diffusion throughout the interior surfaces too, and increases dye adsorption significantly. Relatively lower surface area of UT9, and lower

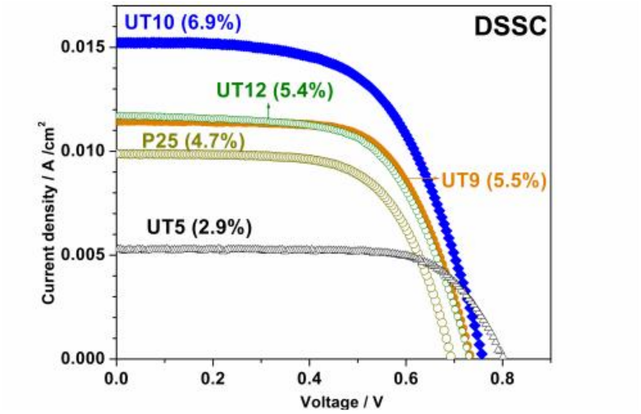

Figure 3.13. J-V characteristics of DSSC based on photoanodes prepared from UTx and compared with P-25. Efficiency (η) values are given in parentheses.

crystallinity of UT12 decreases η. The η of DSSC based on UT10 is significantly better, by about 47% compared to P25. Higher crystallinity (or low defect concentration) of UT10 clearly minimizes charge carrier recombination leading to fast electron conduction and maximum charge collection. Superior textural properties also allow interior and exterior surfaces accessible to the electrolyte, leading to higher V_{oc} and J_{sc} in UT10. In contrast to the above, UT5 shows η = 2.9%, which is much lower than P-25. This is attributed to the low surface area and especially the predominant rutile phase with large

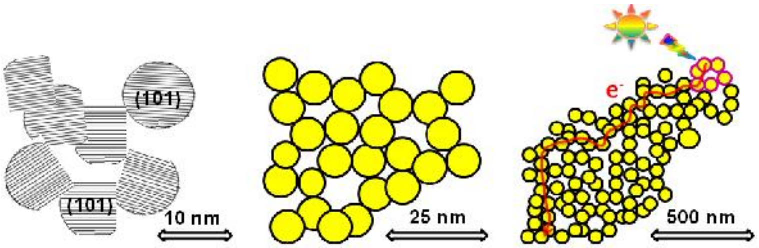

Figure 3.14: Cartoon model to show the connectivity between nanocrystalline particles and the same extending to micron scale length to enhance electron transfer capacity between particles. Introduction of yellow color in the latter two cartoons is to emphasize the increase in electron density.

crystallite size. Although, P-25 also contains 30% rutile (anatase 70%), however, the anatase phase in UT5 is just 20 % (rutile 80%). In addition, there is no interconnectivity between the particles observed on UT5, mainly due to large rutile content with large crystallite size. In short, most of the favourable factors found in UT10 toward high η, such as high surface area, EINP, are missing in UT5.

A series of cartoons shown in Figure 3.14 illustrates the EINP nature of meso $TiO_{2-x}N_x$ from single nanocrystalline particle level to micron length. Fast electron transfer occurs through the EINP network upon illumination on partially dye-coated titania; this is mainly to emphasize the importance of effective charge transfer from the point of origin to the collecting electrode. We believe that such inter-crystallite connectivity is essential to minimize the loss of electrons in secondary processes. Among UTx materials, UT10 exhibits the maximum EINP with (101) facets, highest surface area, porosity and hence high dye loading; all these factors helps for fast charge conduction and hence high surface area. Absence of the above factors in UT5 leads to the lowest η. UT9 and UT12 shows η between the above two values. Although many favourable factors (high surface area, comparable dye loading to that of UT10) are found with UT9 and 12, missing EINP character decreases the η.

Upon illumination of DSSC with 1 sun AM 1.5 light, electron transfer from dye to electron rich UT10 nancrystallites occurs, which creates an artificial potential difference with near neighbour environment. This potential difference would help for fast charge transfer towards the TCO through the UT10 network (Fig. 3.14).

3.4. Conclusion

Mesoporous $TiO_{2-x}N_x$ materials have been prepared by simple SCM and thoroughly characterized by structural, spectroscopy, textural and microscopy methods. This is probably the first report where we produced materials which have all aspects like visible light absorption, disordered mesoporosity with electrically interconnected nanoparticles, anatase phase, smaller particle size with high crystallinity and high surface area. Among all of the materials studied, UT10 gives the best activity for rhodamine-B degradation, in spite of a high band gap of 3.24 eV. Dye degradation occurs very fast under direct sunlight. Photocatalytic oxidation of p-anisyl alcohol to p-anisaldehyde is also performed using UT10 catalyst with direct sunlight. High visible light driven photocatalytic activity is attributed to large surface area, N-doping and smaller particle size of UT10. Very likely the charge carrier recombination is very low with UT10 which gives the best activity due to fast diffusion of charge carriers due to high crystallinity, and less diffusion length due to the disordered mesoporous nature of UT10. Moreover the *psuedo* 3D nature of mesoporous $TiO_{2-x}N_x$ in the present set of materials leads to faster diffusion of charge carriers to surfaces. Disordered mesoporosity with large number of bigger pores and electrically interconnected nanosized, but crystalline, particles lead to a higher efficiency in DSSC, as in UT10. Generally, the efficiency is higher when the nanocrystalline (101) faceted particles interconnected in a mesoporous framework and it is quantitatively shown. The energy conversion efficiency of DSSC based on UT10 is significantly higher, by about 47% compared to P25. The present study throws light on the importance of textural properties for fast electron transfer and hence higher efficiency of DSSC. More studies in this direction, such as further optimization of textural properties, is likely to increase the efficiency further.

3.5. References:

1. U.G. Akpan, B.H. Hameed *J. Hazar. Mater*., **170** (2009) 520.
2. T.V. Gerven, G. Mul, J. Moulijn, A. Stankiewicz, *Chem. Eng. Proc*. **46** (2007) 781.
3. O. Carp, C.L. Huisman, A. Reller, *Solid State Chem*. **32** (2004) 33.
4. B. O’Regan, M. Grätzel, *Nature*, **353** (1991) 737.
5. M. Grätzel, *Nature*, **414** (2001) 338.

6. L. Cao, F.J. Spiess, A. Huang, S.L. Suib, T.N. Obee, S.O. Hay and J.D. Freihaut, *J. Phys. Chem. B,* **103** (1999) 2912.
7. A. Kudo and Y. Miseki, *Chem. Soc. Rev*., **38** (2009) 253.
8. H. J. Snaith, *Adv. Funct. Mater*., **20** (2010) 13.
9. K. Bhattacharyya, S. Varma, A.K. Tripathi, S.R. Bharadwaj and A.K. Tyagi, *J. Phys. Chem. C,* **112** (2008) 19102.
10. A.S. Mukasyan, C. Costello, K.P. Sherlock, D. Lafarga and A. Varma, *Separ. Purif. Tech*., **25** (2001) 117.
11. A.S. Mukasyan, P. Epstein and P. Dinka, *Proc. Combust. Inst.,* **31** (2007) 1789.
12. C-C. Hwang and T-Y. Wu, *J. Mater. Sci*., **39** (2004) 6111.
13. H. Guo, D. Li, D. Giang, W. Li and Y. Sun, *Catal. Lett*., **135** (2010) 48.
14. A. Sclafani, L. Palmisano and M. Shiavell, *J. Phys. Chem*., **94** (1990) 829.
15. S. Basu, M. Mapa, C.S. Gopinath, M. Doble, S. Bhaduri and G.K. Lahiri, *J. Catal.,* **239** (2006) 154.
16. S.B. Waghmode, R. Vetrivel, S.G. Hegde, C.S. Gopinath and S. Sivasanker, *J. Phys. Chem. B,* **107 (**2003) 8517.
17. H. Yoshitake, T. Sugihara and T. Tatsumi, *Chem. Mater***. 14** (2002) 1023.
18. K.U. Gautam, L.S. Panchakarla, B. Dierre, X. Fang, Y. Bando, T. Segikuchi, A. Govidaraj, A. Golberg and C.N.R. Rao, *Adv. Funct. Mater.,* **19** (2009) 131.
19. J.C. Yu, L. Zhang, Z. Zheng and J. Zhao, *Chem.Mater*., **15** (2003) 2280.
20. S.S. Kim, T.R. Pauly and T. Pinnavaia, *Chem. Commun*. (2000) 835.
21. Z. Zhang and T. Pinnavaia, *J. Am. Chem. Soc.*, **124** (2002) 12294.
22. K.S.W. Singh, *Pure Appl. Chem.,* **57** (1985) 603.
23. D.G. Kulkarni, A.V. Murugan, A.K. Viswanath and C.S. Gopinath, *J. Nanosci. Nanotech.*, **9** (2009) 371.

24. X. Wang, J.C. Yu, Y. Chen, L. Wu and X. Fu, *Environ. Sci. Technol.,* **40** (2006) 2369.

25. G. Liu, L. Wang, C. Sun, X. Yan, X. Wang, Z. Chen, S.C. Smith, A-M. Cheng and G.Q. Lu, *Chem. Mater.*, **21** (2009) 1266.

26. T. Takahashi, H. Nakabayashi, J. Tanabe, N. Yamada and W. Mizuno, *J. Vac. Sci. Technol. A*, **21** (2003) 1419.

27. T. Ohsaka, F. Izumi and Y. Fujiki, *J. Raman Spectrosc*., **7** (1978) 321.

28. H. Berger, H. Tang and F. Levy, *J. Cryst. Growth*, **130** (1993) 108.

29. H. Tang, K. Prasad, R. Sanjines, P.E. Schmid and F. Levy, *J. Appl. Phys.* **75** (1994) 2042.

30. R. Asahi, T. Morikawa, T. Ohwaki, K. Aoki and Y. Taga, *Science,* **293** (2001) 269-271.

31. M. Sathish, B. Viswanathan, R.P. Viswanath and C.S. Gopinath, *Chem. Mater.*, **17** (2005) 6349.

32. M. Sathish, R. P. Viswanath and C. S. Gopinath, *J. Nanosci. Nanotech.*, **9 (**2009) 423.

33. M. Anpo and M. Takeuchi, *J. Catal*., **216** (2003) 505.

34. (a) M. Vijayaraj, C.S. Gopinath, *J. Catal*., **241** (2006) 83. (b) S.B. Waghmode, R. Vetrivel, S.G. Hegde, C.S. Gopinath, S. Sivasanker, *J. Phys. Chem. B*, **107** (2003) 8517.

35. (a) S. Velu, K. Suzuki, C.S. Gopinath, T. Hattori, H. Yoshida, *Phys. Chem. Chem. Phys*. **4** (2002) 1990. (b) B. Naik, K.M. Parida, C.S. Gopinath, *J. Phys. Chem. C*, **114** (2010) 19473. (c) S. Velu, K. Suzuki, C.S. Gopinath, *J. Phys. Chem. B*, **106** (2002) 12737.

36. C.S. Gopinath, *J. Phys. Chem. B.,* **110** (2006) 7079.

37. S. Sakthivel and H. Kisch, *Chem. Phys. Chem*., **4** (2003) 487.

38. K. Maeda and K. Domen, *J. Phys. Chem. C*, **111** (2007) 7851.

39. K-M. Lee, V. Suryanarayanan, K-C. Ho, *Sol. Energy Mater. Sol. Cells,* **90** (2006) 2398.

40. M. Adachi, M. Sakamoto, J. Jiu, Y. Ogata, S. Isoda, *J. Phys. Chem. B*, **110** (2006) 13872.

41. T. Wu, G. Liu, J. Zhao, H. Hidaka and N. Serpone, *J. Phys. Chem. B*, **102** (1998) 5845.

42. M.A. Fox and M.T. Dulay, *Chem. Rev*., **93** (1993) 341.

43. S.W. Lam, K. Chiang, T.M. Lim, R. Amal and G.K-C. Low, *J. Catal.*, **234** (2005) 292.

44. G. Palmisano, S. Yurdakal, V. Augugliaro, V. Loddo and L. Palmisano, *Adv. Synth. Catal.*, **349** (2007) 964.

45. S. Yurdakal, G. Palmisano, V. Loddo, V. Augugliaro and L. Palmisano, *J. Am. Chem. Soc.*, **130** (2008) 1568.

Chapter 4

Characterization and Application of nano Au/$TiO_{2-x}N_x$ composites in Solar H_2 Generation

4. Characterization and Application of nano Au/$TiO_{2-x}N_x$ composites in Solar H_2 Generation

Synopsis

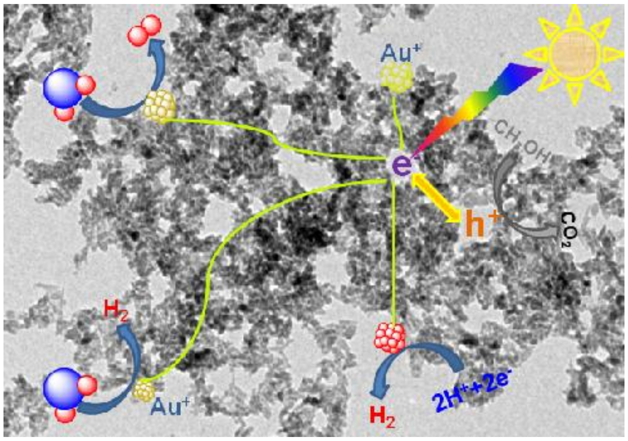

- Electronically integrated nano Au clusters with multifunctional, disordered mesoporous $TiO_{2-x}N_x$ (Au-NT) nanocomposites are prepared by simple one pot combustion synthesis.
- Au-NT nanocomposite material possesses all the desired properties, such as nanogold clusters with SPR in broad visible light regime, $TiO_{2-x}N_x$ with disordered mesoporosity and high surface area, electrically interconnected nanoparticles (EINP) and defects-less due to effective electronic integration of Au with $TiO_{2-x}N_x$ in Au-NT.
- Au-NT nanocomposites materials show decent activity towards H_2 generation from aqueous methanol solution under visible light irradiation. Among all 0.05 Au-NT gives 1.5 mmol h^{-1} g^{-1} from aqueous methanol under visible light irradiation.

4.1. Introduction

Visible light driven photocatalytic water splitting reaction (WSR) is projected to be an indispensable solution to meet a significant part of clean and sustainable energy demand at global level. [1] Producing hydrogen, a clean fuel from water and sun light, by overall water splitting reaction (OWSR) is an ultimate goal to sustain the globe in a better way. [1-3] In spite of many efforts in the past, OWSR by visible light driven photocatalysis is yet to produce a breakthrough in terms of quantum efficiency (QE) close to 10 % or above, which is the bench mark to think about commercialization. This might be considered as a long term solution for energy demands, from the rate of progress of OWSR achieved in the last three decades. Nonetheless, H_2 production through WSR with a sacrificial agent, such as methanol, glycerol, might be considered as a short term goal, as it is relatively less difficult than OWSR. [4-5]

In semiconductor photocatalysis, especially in WSR, the activity mainly depends on the electronic structure of the semiconductor. After photoexcitation, the electrons and holes should diffuse to the surface of the semiconductor without recombination can, reduce and oxidize the adsorbed reactants respectively, by the semiconductor. From a thermodynamic point of view, OWSR can occur only when the bottom level of the CB has to be more negative than the redox potential of H^+/H_2 (0 V *vs.* NHE), while the top level of the VB be more positive than the redox potential of O_2/H_2O (1.23 V). [6] The efficiency of a photocatalyst depends on the competition of different interface transfer processes involving electrons and holes and their deactivation by recombination. [7] Due to rapid recombination of photo-generated CB electrons and VB holes, it is difficult to achieve OWSR using pure TiO_2 photocatalyst in distilled water. Adding electron donors (commonly known as sacrificial reagents or hole scavengers) to react irreversibly with the photo-generated VB holes can enhance the photocatalytic electron/hole separation resulting in higher QE. [8] Since electron donors are consumed in photocatalytic reaction, continual addition of electron donors is required to sustain hydrogen production. As the hole scavengers are more favorably oxidized than water molecules the thermodynamical and kinetic constraints are greatly reduced. Free energy of the reaction is tremendously decreased and thus the crucial rate determining step of water splitting is also taken care.

In water/methanol system, around 3 mols of H_2 is produced by the consumption of one mole of CH_3OH.

$$CH_3OH + H_2O \rightarrow 3H_2 + CO_2 \tag{4.1}$$

Sakata et al [9] suggested a stepwise mechanism for H_2 production from a water/MeOH solution which involves stable intermediates, such as aldehydes and acids:

$$MeOH_{(l)} \leftrightarrow HCHO_{(g)} + H_{2\ (g)} \qquad \Delta G^0{}_1 = 64.1\ kJ/mol$$

$$HCHO_{(g)} + H_2O_{(l)} \leftrightarrow HCO_2H(l) + H_{2(g)} \qquad \Delta G^0{}_2 = 47.8\ kJ/mol$$

$$HCO_2H_{(l)} \leftrightarrow CO_{2(g)} + H_{2(g)} \qquad \Delta G^0{}_1 = -95.8\ kJ/mol$$

H_2 is produced in all of these steps. Bowker et al. [10], on the other hand, suggested a different mechanism which involves chemisorption and dehydrogenation of MeOH on active sites to produce chemisorbed CO and subsequent oxidation of the chemisorbed CO to CO_2.

$$CH_3OH + S \rightarrow CO_a + 2H_2 \tag{12}$$

$$TiO_2+ + hv \rightarrow Ti^{3+} + O^- \tag{13}$$

$$CO_a + O^- \rightarrow CO_2 + S + V_o^- \tag{14}$$

$$H_2O + V_o^- \rightarrow O^- + H_2 \tag{15}$$

$$Ti^{3+} + O^- \rightarrow TiO^{2+} \tag{16}$$

Similarly, in water/glycerol system produces 7 mols of H_2 and 3 mols CO_2 with the consumption of 1 mol of glycerol.

Noble metals, Pt, Au, Pd, Rh and Ni, Cu, Ag, have been reported to be very effective for enhancement of TiO_2 photocatalysis. Noble metal cluster deposition on titania acts as an electron sink by selectively storing electrons. As the Fermi levels of these noble metals are lower than that of TiO_2, photo-excited electrons can be transferred from CB to metal particles deposited on the surface of TiO_2, while photo-generated VB holes remain on the TiO_2. These activities greatly reduce the possibility of electron-hole recombination, resulting in efficient separation and stronger photocatalytic reactions. Under light irradiation photogenerated electrons accumulate and raise the Fermi level (E_F) of the composite where in E_F of metal and semiconductor are in equilibrium. As the E_F of the composite become more negative the free energy of reduction capacity also turns to be more negative influencing enhanced water reduction. There will be facile charge separation in the nanostructure loaded semiconductor composite system because charge carrier is selectively generated at three phase boundary formed by semiconductor, metal nanostructure and aqueous medium. As it is being the reaction site for WSR charge recombination is highly suppressed. Among metals Au, Ag, Pt receives attention mainly due to its nobility and visible light SPR. These nano Au or Ag depositions on titania brings more visible light absorption through its surface plasmon resonance (SPR) bands. In the case of Au on TiO_2, the size of Au, the size of the TiO_2 particulate support and the nature of TiO_2 can each, in turn, influence the photocatalytic activity.

In this chapter, we successfully synthesized an electronically integrated nanocomposite of nanoAu with nanocrystalline disordered mesoporous $TiO_{2-x}N_x$ (Au-NT) materials in a single step by tandem approach using SCM. Au-NT composite material possesses some of the most desired properties, such as (1) nanogold clusters with SPR in broad visible light range, (2) $TiO_{2-x}N_x$ with disordered mesoporosity, low meso-channel depth (≤ 10 nm) and high surface area, electrically interconnected nanoparticles (EINP), (3) effective reduction of defects due to electronic integration of Au with $TiO_{2-x}N_x$ in Au-NT, (4) significantly large lifetime of electrons in millisecond range. These nanocomposite materials show decent activity towards H_2 generation from aqueous methanol solution under visible light irradiation.

4.2. Results and Discussion

4.2.1. Powder XRD

Powder X-ray diffraction (PXRD) measurements were carried out in order to explore the structural features of xAu-NT nanocomposite materials. Figure 4.1 shows the PXRD pattern of all xAu-NT materials. All the peaks in the XRD pattern could be indexed to anatase phase of TiO_2 (JCPDS File 21-1272). [11]

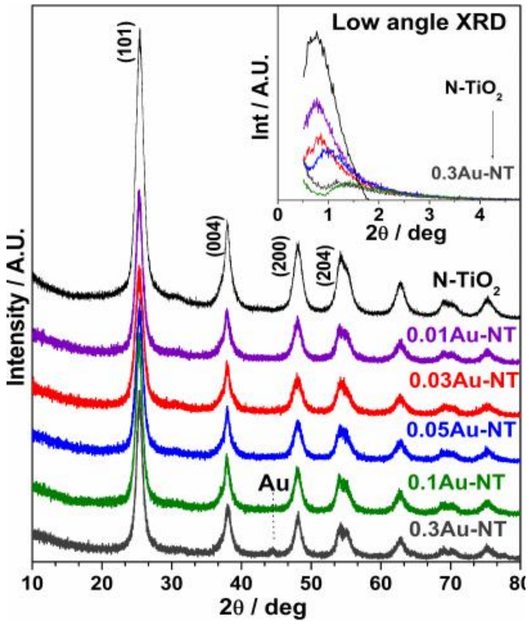

Figure 4.1: Wide angle XRD pattern of xAu-NT materials. Inset shows the low angle XRD pattern of xAu-NT nanocomposite materials.

There is no other peaks observed corresponds to the rutile TiO_2. All the XRD peaks are broad in nature which confirms the nanocrystalline nature of the materials. Crystallite size was calculated by using Debye-Scherer equation and shown in Table 4.1. Upto 0.10Au-NT, there is no feature observed that corresponds to metallic gold. However, 0.30Au-NT shows a small peak at $2\theta=44^{\circ}$ corresponds to (200) plane of metallic gold. This observation supports the presence of highly dispersed nano gold clusters on xAu-NT ($x \leq 0.1$).

Inset in Figure 4.1 shows the low angle XRD pattern of all xAu-NT materials. Mesoporous nature of Au-NT materials was confirmed by the low angle features in XRD. Only one peak was observed around $2\theta = 0.8\text{-}1.4^{\circ}$ without any additional peaks indicating the presence of disordered mesoporosity. [11, 12] Unlike the ordered hexagonal mesoporous materials, like MCM-41, SBA-15, no other low angle peaks was observed [13-15] highlighting the mesoporous nature is likely due to an intergrowth of fundamental particles. High Au loading (=0.3) significantly affects the mesoporosity of the materials. A severe decrease in low angle peak at $2\theta=1.5°$ indicating a pore blockage by gold clusters. Nonetheless all xAu-NT materials possess disordered mesoporosity along with nanocrysatallinity.

4.2.2. N_2 adsorption isotherm

N_2 adsorption-desorption studies has been measured to investigate the textural properties of the xAu-NT materials. [16] Figure 4.2 shows N_2 adsorption-desorption results and BJH pore size distribution of xAu-NT materials. All materials show type IV adsorption-desorption isotherm with H2 hysteresis loop which is typical for all mesoporous materials. [17] All xAu-NT nanocomposite materials show narrow pore size distribution with an optimum pore diameter around 8±1 nm. BET surface area of all materials were calculated and shown in Table 4.1. xAu-NT nanocomposite materials exhibits significantly lower surface area than the nitrogen doped TiO_2. [12] Among these composite materials, 0.05Au-NT shows high surface area (213 m^2/g). Surface area decreases with more Au loading and 0.3Au-NT shows the surface area of 157 m^2/g indicating a pore blockage.

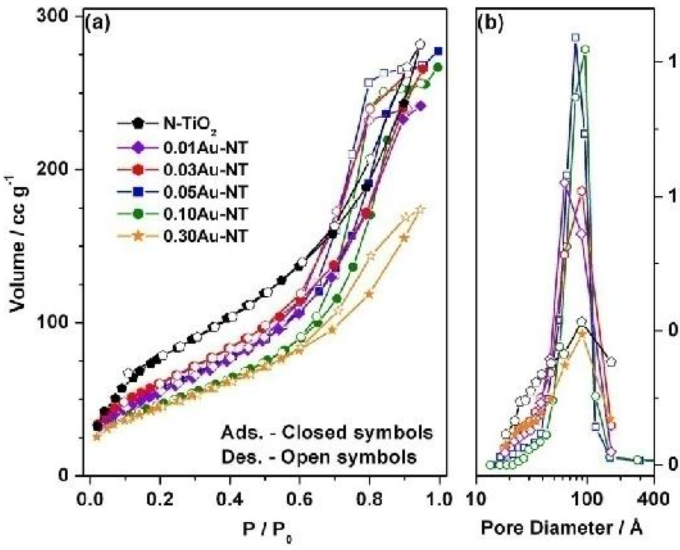

Figure 4.2: (a) N_2 adsorption-desorption isotherms, and (b) BJH pore-size distribution of xAu-NT nanocomposite materials.

Table 4.1. Physicochemical properties of xAu-NT materials.

Material	BET Surface area (m^2/g)	Pore size (nm)	Pore volume (cc/g)	Crystallite size (nm)	Bulk Au content	Defect sites[#] (%)
N-TiO_2	234	7	0.44	6.8	0	51.0
0.01Au-NT	182	8.2	0.37	6.0	0.009	23.0
0.03Au-NT	200	8.1	0.41	6.2	0.026	10.5
0.05Au-NT	213	8	0.43	6.9	0.045	4.4
0.10Au-NT	171	9.6	0.41	8.0	0.11	8.7
0.30Au-NT	157	6.8	0.27	8.8	0.28	33.6

[#] Defects sites calculated from PL and with reference to Degussa P-25's PL data (100 %)

4.2.3. TEM

Particle morphology of xAu-NT materials has been studied by HRTEM carefully. HRTEM images recorded for 0.05Au-NT and 0.3Au-NT materials are shown in Figure 4.3. All xAu-NT particles exhibits spherical or near spherical shape morphology. A disordered mesoporous structure can be seen for all xAu-NT materials. [18,19] Above disordered mesoporosity arises due to intergrowth of fundamental particles and the same leads to aggregates with significant extra framework void space.

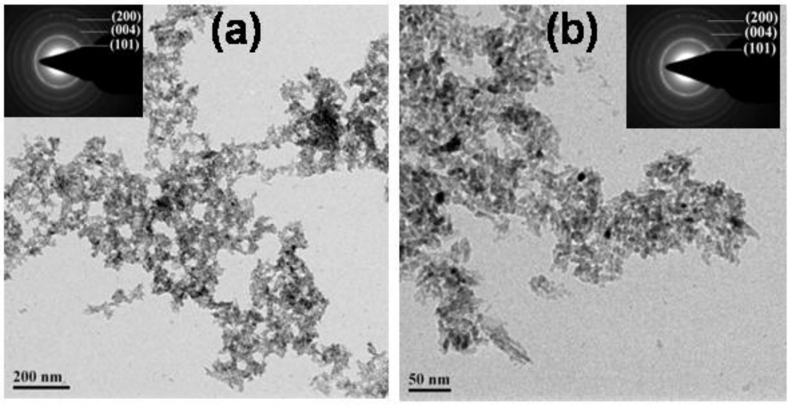

Figure 4.3: HRTEM image of (a) 0.05Au-NT, and (b) 0.03Au-NT nanocomposite materials. SAED is shown in the inset. No distinct gold particles are observed indicating a well dispersed and very small Au-particles.

Presence of meso and macro pores is clearly visible in Figure 4.3, which is required for faster diffusion of reactants and products in heterogeneous catalysis. Selected-area electron diffraction (SAED) pattern confirms the crystalline nature of the nanocrystalline xAu-NT materials and also it shows the anatase phase in all xAu-NT nanocomposite materials. HRTEM image shows the majority of lattice fringes corresponding to (101) (d(101) = 0.352 nm) crystallographic planes of anatase phase. These observations are in excellent agreement with XRD as well as with N_2 adsorption isotherm results. Present disordered mesoporous structure has an additional advantages like low diffusional barriers, since the depth or length of mesopores are minimum (~10 nm). [20] This disordered *p*3D wormhole like framework provides an easy route for the diffusion of reactants due to less diffusional barriers. Moreover these nanocrystallites are electrically well connected with each other and this connectivity extends upto microns. Due to EINP nature, [20] the excited electron can diffuse effectively from the bulk to the surface with less recombination during photocatalysis. Advantageous

EINP feature associated with xAu-NT nanocomposite material increases the life time of charge carrier, specifically electron through a porous frame work, which in turn increases the water splitting activity. Although the presence of gold is not visible in TEM images, but EDX confirms its presence and suggesting the presence of very small gold clusters of around 1 nm in size on mesoporous xAu-NT.

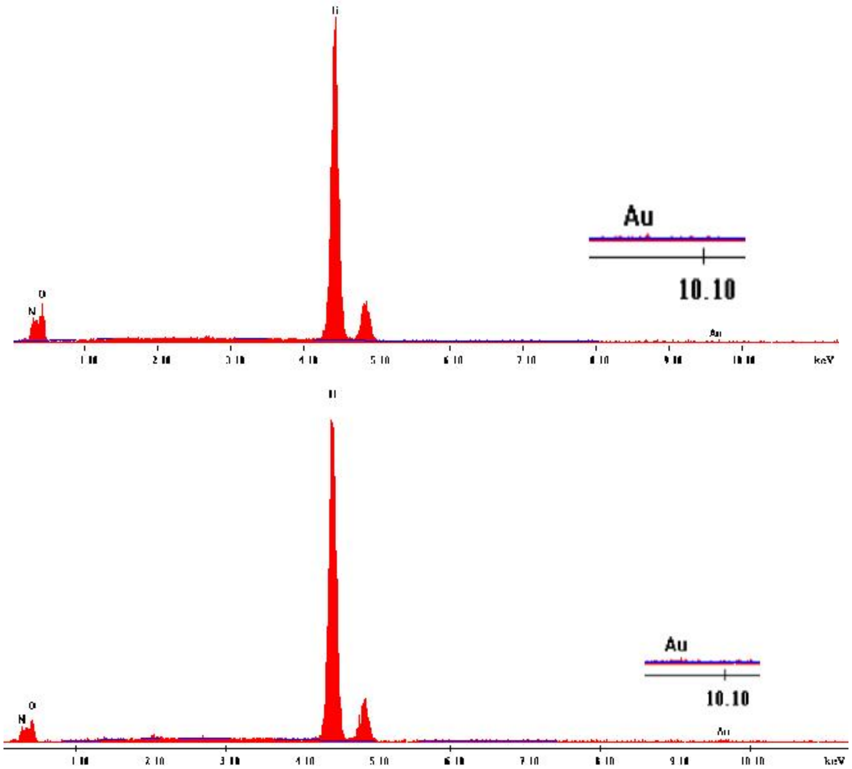

Figure 4.4: Elemental content of (top panel) 0.05 Au-NT (bottom panel) 0.3 Au-NT measured by EDX.

Figure 4.4 shows the EDX image of 0.05Au-NT and 0.3Au-NT nanocomposites. This small gold clusters are acting as sink for photoexcited electrons and increase the electron utilization. Indeed above charge separation increases the electron (hole) utilization on Au (titania) surfaces.

4.2.4. Raman spectroscopy

Raman spectroscopy is a versatile tool to determine the structural features of the oxide materials. Figure 4.5 shows the Raman spectra for all xAu-NT nanocomposite materials. In case of these nanocomposite materials, all six Raman active fundamental modes are observed at 145 (E_g), 198 (E_g), 398 (B_{1g}), 516 (A_{1g} + B_{1g}), 640(E_g) cm^{-1} for the anatase phase. [21]

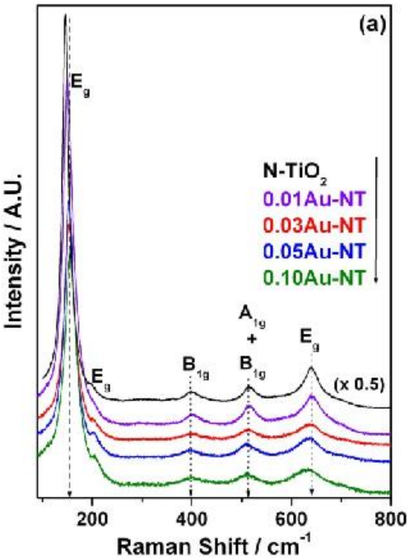

Figure 4.5: Raman spectra of xAu-NT nanocomposite materials. Raman active E_g mode on N-TiO$_2$ at 145 cm^{-1} shows a blue shift to 154 cm^{-1} and lower intensity with increasing Au-content.

Broad nature of these peaks confirms the formation of nanosize particles. [12] None of the Raman features was observed for rutile phase of TiO$_2$ which supports the presence of pure anatase phase in all these nanocomposite materials. Raman active E_g mode at 145 cm^{-1} exhibits a blue shift to 154 cm^{-1} upon composite formation of Au nanoparticles with N-TiO$_2$. Although no such blue shift has been reported in the literature, it is likely that there is a strong electronic interaction between anatase lattice with Au nano particles. Indeed this electronic interaction is essential for fastelectron transfer from the point of origin in titania lattice to nearby Au nanoparticle. EINP network present in N-TiO_2 helps for the above electron transfer. Further this also preferentially seperates e^- from holes and enhances the lifetime of charge carriers. We believe the above factors enhance the utilization of charge carriers for water splitting.

4.2.5. UV-Visible spectroscopy

Figure 4.6 shows the UV-visible spectra for all xAu-NT nanocomposite materials. The absorption edge of titania shows marginal red shift due to nitrogen doping. It has already been demonstrated (chapter 3, sec 3.2.6) that nitrogen doping in mesoporous titania gives visible light photocatalytic activity towards rhodamine B degradation, selective oxidation of alcohol to aldehyde and it is elaborately discussed in chapter 1. Inset in Figure 4.6 shows a photograph for colours of all Au-NT nanocomposite materials. N-TiO_2 shows a pale yellow colour and upon Au introduction blue

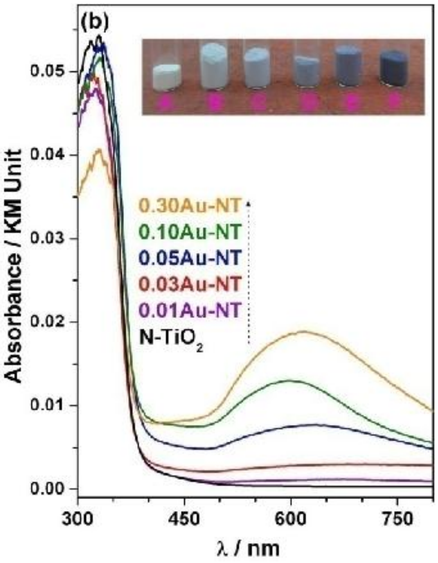

Figure 4.6: UV-Visible absorption spectra of xAu-NT nanocomposites. Inset shows the color variation with increasing Au-content of xAu-NT, with sample labels as A = N-TiO_2, B = 0.01Au-NT, C= 0.03Au-NT, D=0.05AuNT, E=0.10AuNT and F = 0.30Au-NT.

or blue grey colour develops gradually. On increasing Au to 0.1 and above, the colours changes to dark blue. SPR features of nano gold in these composite materials bring more visible light absorption. [22] This absorption is due to collective oscillation of free CB electrons of the gold particles in response to optical excitation. [23] Above SPR peak intensity increases with increasing gold loading and the position of this peak depends on the gold particle size, shape and the surrounding environment [24, 25] SPR peak maximum is observed between 550 and 650 nm highlighting the contribution from Janus and core-shell Au-NT nanostructure. [26] In case of Janus morphology, due to the non-centrosymmetric coupling of the metal and dielectric oxide nanoparticles at their small, interconnecting junction, extremely strong local electric nearfields can be generated through interparticle coupling. Above two nanostructures indicates that there is a strong electronic coupling of Au and $TiO_{2-x}N_x$ so that the charge separation and charge utilization is maximum at these interfaces. SPR peak maximum shifts to 620 nm for 0.3Au-NT indicating the pre-dominant yoke-shell morphology. This is supported by low pore volume and surface area (Table 4.1). SPR peak at higher wavelength is partly due to the high refractive index of anatase titania. [27] Hence more number of visible light photons can be harvested by using these xAu-NT nanocomposite materials. Apart from visible light absorption, these nano gold centres exhibit dual role in visible light photocatalytic water splitting reactions. These nano gold centres are acting as electron sinks by forming the schottky barriers with semiconductor metal oxides and moreover these centres are the sites for hydrogen evolution. Thus gold loading on meso $TiO_{2-x}N_x$ increases the visible light absorption and decreases the recombination probability of electron-hole pair.

4.2.6. Photoluminescence Spectroscopy

Figure 4.7 shows the PL emission spectra of Degussa P25 (P25) and xAu-NT nanocomposites. PL emission is the result of the recombination of charge carriers under irradiation conditions. All xAu-NT composites and P25 show peaks around 419, 442 and a shoulder around 470 nm. In general, the emission peak due to the band gap transition appears at 370 nm. [28] However, N-TiO_2 and other composite materials exhibit the emission at relatively higher wavelength which is mainly attributed to the band gap reduction of TiO_2 due to nitrogen doping. The emission band at 419 nm is due to free exciton emission of TiO_2. [29] Appearance of shoulder around 470 nm is due to the surface state such as Ti^{4+}−OH.[30] The emission feature at 440 nm originates from the charge-transfer transition from Ti^{3+} to oxygen anion in a TiO_6^{8-}

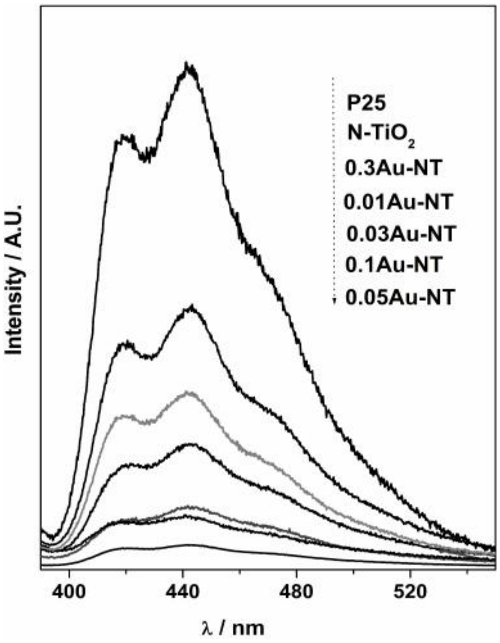

Figure 4.7: Photoluminescence spectra for xAu-NT materials.

complex [31] present in the material. All the three above emission features decreased in intensity from P25 to N-TiO_2 to xAu-NT. Assuming defects site density on P25 is 100%, a quantitative PL emission intensity calculation shows the same decreases to 51, 23, 10.5, 4.4 and 8.7 % on N-TiO_2, 0.01, 0.03, 0.05 and 0.10Au-NT, respectively. About two orders of magnitude decrease in defects site density with 0.05Au-NT underscores the maximum charge separation by trapping electrons in Au clusters. This also underscores that it is due to a large electronic integration of Au-clusters with titania. Indeed this is the critical observation that highlights the electronic interaction of nano Au clusters with $TiO_{2-x}N_x$. In fact it underscores the recombination of charge carriers is largely minimized due to effective electron trapping by Au clusters in xAu-NT. Curved surfaces of (101) facet with low surface energy Ti dangling bonds favours the uniform deposition of small gold clusters.

On increasing the Au content to 0.1 atom %, an increase in PL emission intensity comparable to 0.03Au-NT is observed. Further increase in the gold content (x = 0.30) increases the intensity of PL emission bands, which is attributed to the aggregation of bigger size gold particles. Bigger Au particles, as observed in XRD (Fig. 1a), decrease the interaction with $TiO_{2-x}N_x$ lattice, and thereby the electronic interaction also decreases. Indeed aggregation of gold particle at x = 0.3 re-exposes the defects sites present on $TiO_{2-x}N_x$ surface. An optimum quantity of gold (x = 0.05) in the Au-NT composite materials minimizes the defect sites by selective electron trapping in gold clusters.

4.2.7. XPS

To know more about the electronic integration aspects of xAu-NT, XPS studies have been carried out. A very interesting observation was made with Ti 2p core level results (Figure 4.8). As prepared xAu-NT nanocomposites show three features for Ti 2p core level (thin traces in Figure 4.8), in contrast to the normal two core level peaks for Ti $2p_{3/2}$ and $2p_{1/2}$. [32, 33] A glance at the above features indicates a possible static-charge buildup upon photoelectron emission and hence a low energy electron flood gun was employed to neutralize the above charge build-up. After charge neutralization the XPS result shows broad Ti 2p features (bold traces in Figure 4.8). Indeed these observations highlights some facts about the electronic aspects of xAu-NT. (1) Low BE feature observed around 457 eV corresponds to Ti^{3+} oxidation state on both 0.05 and 0.1 Au-NT. (2) Above low BE feature

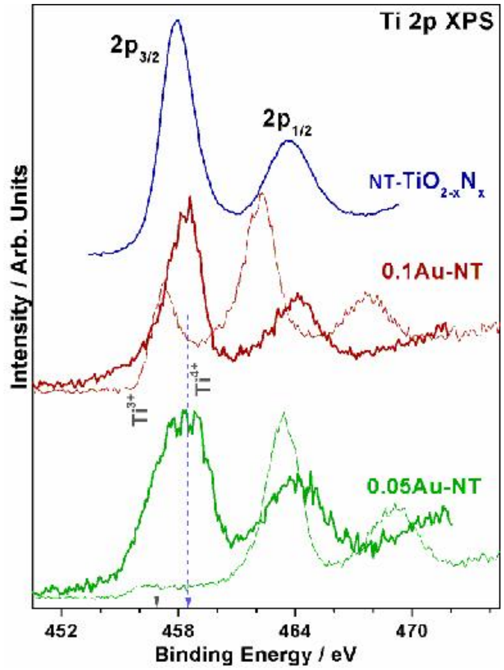

Figure 4.8: XPS core level spectra recorded for Ti 2p core level for NT and xAu-NT. Low energy electron flood gun employed to neutralize the static charge buildup on xAu-NT and the results are given in bold traces.

was observed even without applying flood gun source indicates a highly conducting nature of part of the nanocomposite material; this is attributed to a possible electronic interaction of nano Au clusters with Ti^{3+} in TiO_6^{8-}. Indeed a very small size Au-clusters (≤ 1 nm) are reported to be cationic in nature, [34] and above such interaction annihilate the defects associated with titania. (3) Unlike 0.1Au-NT, without applying electron flood gun, 0.05 Au-NT shows a continuous Ti 2p photoelectron emission from 457 eV till the onset of the next peak at 462 eV. This hints a distribution of gold clusters at very small sizes with 0.05Au-NT. A sharp peak at 457 eV with 0.1 Au-NT suggests a relatively uniform Au particle size. Indeed, the above points not only suggest a strong electronic interaction between Au and titania in Au-NT nanocomposites, but also a polarizing structural features on the surface, which effectively separates electron from electron-hole pairs and disordered mesoporous framework helps towards that. We believe the SCM adopted to prepare Au-NT deposits Au directly on TiO_6^{8-} defect sites, where the reduction of $2H^+$ to H_2 reaction occurs.

4.3. Catalytic Activity

4.3.1. Photocatalytic water splitting

In order to evaluate the efficacy of the above Au-NT nanocomposites, photocatalytic WSR was carried out under simulated sun light with aqueous methanol solution. Figure 4.9a shows the amount of H_2 evolution using 0.05Au-NT nanocomposites for continuous 15 h with evacuation after every 5 h. Steady rate of H_2 evolution is observed for at least another five such cycles with very similar activity suggests a photostability of the nanocomposites. CO_2 was also produced, along with H_2, has been confirmed by GC analysis. Ratio of H_2/CO_2 is close to 3 suggesting the general mechanism of one molecule each of CH_3OH and H_2O leading to $3H_2$ and CO_2 on titania surfaces. [5] Figure 4.9b shows the photocatalytic H_2 evolution activity of

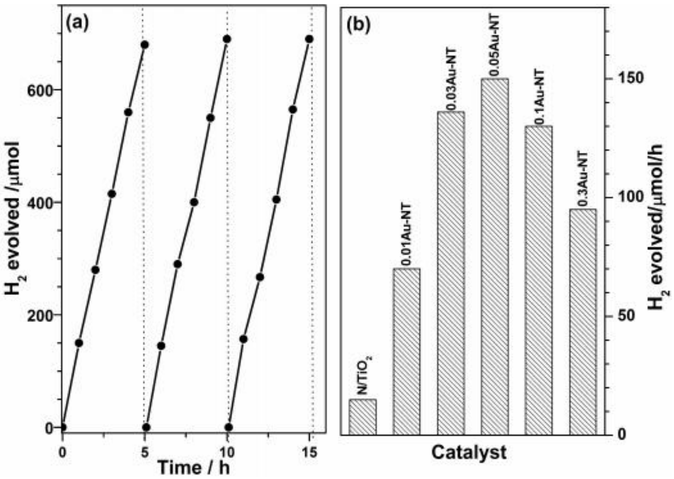

Figure 4.9: Photocatalytic H_2 evolution activity of (a) 0.05Au-NT for 15 hours, and (b) xAu-NT materials under white light irradiation with aqueous methanol solution. Amount of H_2 evolution reported is with 100 mg of catalyst. Dotted lines in (a) indicate evacuation after every 5h.

all xAu-NT materials. Among all the materials, 0.05Au-NT shows the highest H_2 evolution rate than other compositions. About 150 µmol H_2/h is generated with 100 mg of 0.05Au-NT. Pure $TiO_{2-x}N_x$ shows the lowest activity towards hydrogen generation (14 µmol/h) under similar conditions. Half to one order of magnitude increase in H_2 production observed with xAu-NT composites, compared to $TiO_{2-x}N_x$, demonstrates the critical role of nano Au clusters through SPR. The high rate of H_2 production is attributed to the electronic integration of nano Au clusters with disordered mesoporous $TiO_{2-x}N_x$ framework, which enhances the charge utilization and minimizes the charge recombination.

4.3.2. Photoelectrochemical Measurements

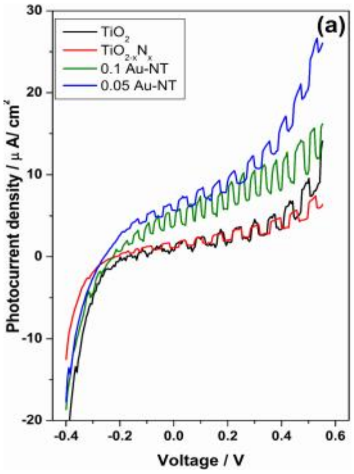

Figure 4.10: (a) Photocurrent generated upon UV illumination is shown to demonstrate a four folds increase in photocurrent density with xAu-NT nanocomposites than without gold clusters. (b) Photocurrent response of xAu-NT materials with time at 0.25V.

In order to support above conclusion, photoelectrochemical measurements have been made under UV light with xAu-NT nanocomposites and the results are shown in Figure 4.10. Compared to titania and $TiO_{2-x}N_x$, xAu-NT displays a four folds increase in photocurrent generation. Indeed the current density values without light (light chopping conditions) suggest a percolation pathway available.

4.4. Conclusion

We successfully synthesized visible light active $TiO_{2-x}N_x$ with Au-nanoclusters in mesopores using simple combustion synthesis protocol. More number of visible light photons could be harvested by SPR of Au clusters and charge carrier mobility is enhanced due to disordered mesoporosity along with electrically interconnected nanocrystallites of $TiO_{2-x}N_x$. It is expected that the junction that interconnects Au cluster to titania generates strong local SPR due to electronic interactions. Large decrease in defect sites density on xAu-NT is supported by PL, XPS and Raman studied. A polarized pathway available enhances the separation of charge carriers and hence its utilization. It is expected that SCM adopted to prepare Au-NT deposits Au directly on TiO^{3-} defect sites, where the reduction of $2H^+$ to H_2 reaction occurs. Also the presence of disordered mesoporosity greatly reduces the diffusion length of charge carriers and EINP helps for fast charge conduction. This added advantage due to *p*3D nature of mesopores helps to utilize the charge carriers efficiently for photocatalysis.

Further the charge carrier utilization is greatly increased by fast conduction of electrons through EINP lattice network and storing electrons in Au nanoparticles for proton reduction to hydrogen. Recombination probability is greatly reduced by nano Au metal clusters. Small mesochannel depth or *psuedo 3D* nature of mesoporous titania helps for faster diffusion of charge carriers to surface.

4.5. References

1. K. Maeda, K. Domen, *J. Phys. Chem. Lett.***,** **1** (2010) 2655.
2. A. Kudo, *Int. J. Hydrogen Energy*. **32** (2007) 2673.
3. R. M. N. Yerga, M. C. Alvarez Galvan, F. del Valle, J.A.Villoria de la Mano, J.L.G. Fierro, *ChemSusChem*, **2** (2009) 471.

4. K.A. Connelly, H. Idriss, *Green Chem.*, **14 (**2012) 260.
5. M. Bowker, *Green Chem.*, **13** (2011) 2235.
6. Marta I. Litter, *Appl.Catal. B: Environ*. **23** (1999) 89.
7. M.D. Ward, J.M. White, A.J. Bard, *J. Am. Chem. Soc*. **105** (1983) 27.
8. M. Ni, M. K.H. Leung, D. Y.C. Leung, K. Sumathy *Renewable and Sustainable Energy Reviews* **11** (2007) 401.
9. Kawai T, Sakata T. *JCS Chem Commun* (1980) 694.
10. A. Dickinson, D. James, N. Perkins, T. Cassidy, M. Bowker, *J Mol Catal A* **146** (1999) 211.
11. B. Naik, K.M. Parida, C.S. Gopinath, *J. Phys. Chem. C* **114** (2010) 19473.
12. K. Sivaranjani, C. S. Gopinath, *J. Mater. Chem.* **21** (2011) 2639.
13. N. Maity, P. R. Rajamohanan, S. Ganapathy, C. S. Gopinath, S. Bhaduri, and G. K. Lahiri. *J. Phys. Chem. C.* **112** (2008) 9428.
14. N. Maity, S. Basu, M. Mapa, P. R. Rajamohanan, S. Ganapathy, C. S. Gopinath, S. Bhaduri, and G. K. Lahiri, *J. Catal.* **242** (2006) 332.
15. S. Basu, H. Paul, C. S. Gopinath, S. Bhaduri, and G. K. Lahiri. *J. Catal.* **229** (2005) 298.
16. D.G. Kulkarni, A.V. Murugan, A.K. Viswanath, C. S. Gopinath, *J. Nanosci. Nanotech*. **9** (2009) 371.
17. K.S.W.Singh, *Pure and Applied Chemistry* **57** (1985) 603.
18. Z. Zhang, and T. J. Pinnavaia, *J. Am. Chem. Soc.* **124** (2002) 12294.
19. S. Kim, T. R. Pauly, and T. J. Pinnavaia. *Chem. Comm.* (2000) 835.
20. K. Sivaranjani, S. Agarkar, S. B. Ogale, C. S. Gopinath. *J. Phys. Chem. C* **116** (2012) 2581.
21. H. Tang, K. Prasad, R. Sanjines, P. E. Schmid, and F. Levy. *J. Appl.Phys.* **75** (1994) 2042.

22. J-J. Chen, J. C. S. Wu, P. C. Wu, and D. P. Tsai. *J. Phys. Chem. C* **115** (2011) 210**.**

23. A. Merlen, V. Gadenne, J. Romann, V. Chevallier, L. Patrone, and J. C. Valmalette. *Nanotechnology* **20** (2009) 1.

24. Y. Wu, H. Liu, J. Zhang, and F. Chen. *J. Phys. Chem. C* **113** (2009) 14689.

25. S. Link, M.A. El-Sayed, *J. Phys.Chem. B.* **103** (1999) 8410.

26. Z.W. Seh, S. Liu, M. Low, S-Y. Zhang, Z. Liu, A. Mlayah, M-Y. Han, *Adv. Mater.*, **24** (2012) 2310.

27. D. Buso, J. Pacifico, A. Martucci, P. Mulvaney, *Adv. Func. Mater.* **17** (2007) 347.

28. Y. Li, N-H. Lee, D-S. Hwang, J.S. Song, E.G.Lee, S-J. Kim, *Langmuir* **20** (2004) 10838.

29. K. Nagaveni, M.S. Hegde, G. Madras, *J. Phys. Chem. B.*, **108** (2004) 20204.

30. K.M. Parida, N. Sahu, A.K Tripathi, V.S. Kamble, *Environ. Sci. Tech.* **44** (2010) 4155.

31. J.C. Yu, J. Yu, W. Ho, Z. Jiang, L. Zhang, *Chem. Mater.* **14** (2002) 3808.

32. M.Sathish, B.Viswanathan, R.P.Viswanath, C.S.Gopinath, *Chem.Mater.* **17** (2005) 6349.

33. M. Sathish, R.P. Viswanath, C.S. Gopinath, *J. Nanosci. Nanotech.* **9** (2009) 423.

34. a) C.N.R. Rao, V. Vijayakrishnan, H.N. Aiyer, G.U. Kulkarni, G.N. Subbanna, *J. Phys. Chem.*, **97** (1993) 11157. b) G.J. Hutchings, et al., *J. Catal.* **242** (2006) 71.

Chapter 5

Characterization and Application of $Ti_{1-x}V_xO_2$ in Oxidative Dehydrogenation of Ethylbenze to Styrene

5. Characterization and Application of $Ti_{1-x}V_xO_2$ in Oxidative Dehydrogenation of Ethylbenze to Styrene

Synopsis

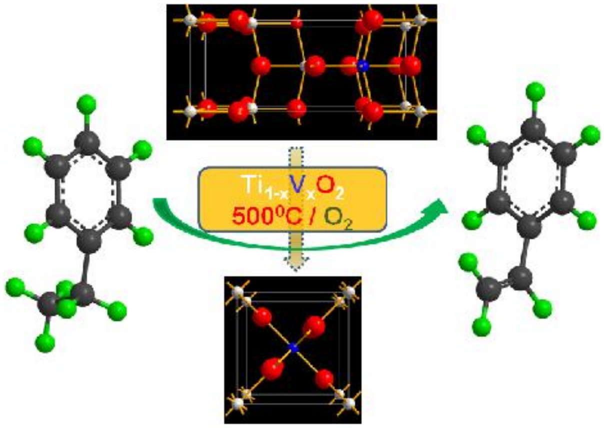

- Oxidative dehydrogenation (ODH) of ethylbenzene to styrene has been studied with vanadium-incorporated mesoporous nanocrystalline titania ($Ti_{1-x}V_xO_2$) in the presence of molecular oxygen between 440 and 530°C.

- Incorporation of V in TiO_2 lattice framework has been achieved by simple solution combustion method. Doping of V in TiO_2 lattice provides isolated V sites which is necessary for selective oxidation reaction.

- High ethylbenzene conversion and stable styrene yield has been observed with 10% V-containing rutile phase titania at 500°C.

- Higher activity of these catalysts primarily attributed to the ionic V^{5+} in $Ti_{1-x}V_xO_2$ lattice, which prevents agglomeration to V_2O_5.

5.1. Introduction

Supported vanadium oxide catalysts are widely used in many industrial processes. Among them V supported on TiO_2 catalysts are used in many oxidation reactions. [1, 2]

Supported vanadium can adopt different structures (such as isolated vanadium species, polymeric-type species and bulk vanadium oxides) on the support. The activity of the supported vanadia catalysts towards selective oxidation reaction mainly depends on the nature of vanadia species as well as the method of preparation, type of starting materials, calcination temperature, nature of titania support, additives/impurities and the acid base properties of the support. [3, 4] Thus, the design of a high-performance supported vanadia catalyst, especially one with a high degree of stability, is still a challenge.

The oxidative dehydrogenation (ODH) of ethylbenzene to styrene is one of the industrially important processes for various large-volume synthetic polymers. It is widely accepted that the ODH of alkane over easily reducible transition metal oxides proceeds via a Mars-van-Krevelen redox mechanism. In that mechanism, it is suggested that during alkane ODH on vanadium catalysts, the catalyst surface is reduced as lattice oxygen atoms activate alkane molecules, ultimately forming olefins. According to the mechanism, alkane must first adsorb (Eq. 5.1) to a surface or lattice oxygen atom (O*), and a C-H bond must be cleaved forming an alkoxy intermediate and a hydroxyl group on the catalyst surface (Eq. 5.2). This initial cleavage of the alkane C-H bond is considered the rate-limiting step, and the literature consistently shows that alkene formation rates are first order in alkane concentration. [5-7] The alkoxy intermediate, which is adsorbed to an oxygen atom, then loses a second hydrogen atom forming alkene and another hydroxyl group on the catalyst surface (Eq. 5.3). Finally, two hydroxyl groups combine to form water and a lattice vacancy (V*) leaving the active site in a reduced state (Eq. 5.4). Gas-phase oxygen must then adsorb to a vacancy and reoxidize the active site (Eq. 5.5).

$$C_nH_{2n+2} + O^* \rightarrow C_nH_{2n+2}O^* \tag{5.1}$$

$$C_nH_{2n+2}O^* + O^* \rightarrow C_nH_{2n+1}O^* + OH^* \text{ (rate determining step)} \tag{5.2}$$

$$C_nH_{2n+1}O^* + O^* \rightarrow C_nH_{2n} + OH^* \qquad (5.3)$$

$$OH^* + OH^* \rightarrow H_2O + O^* + V^* \text{ (lattice vacancy)} \qquad (5.4)$$

$$O_2 + 2V^* \rightarrow 2O^* \qquad (5.5)$$

Styrene is commercially produced by the Fe–K-based catalytic dehydrogenation of ethylbenzene in the presence of a large quantity of steam at 873–973 K. In the present commercial process, steam reduces the partial pressure of ethylbenzene, increasing the equilibrium yield of styrene, as well as it prevents coke deposition. [8] ODH is an attractive alternative to thermal and catalytic dehydrogenation processes utilized for the production of styrene. Due to thermodynamic advantages and fewer catalyst deactivation problems, significant research has been focused on catalytic ODH of EB in recent years. [9] In these ODH reactions, catalyst deactivation is mainly due to the segregation and agglomeration of active species on the support material. Aggregation of active species during the reaction especially at higher temperature is inhibited by lattice incorporation. Hence regeneration of the catalyst is possible by simple calcinations. Moreover this lattice incorporation leads to the formation of isolated V sites which is necessary for selective oxidation reactions. [10]

In the present chapter, we follow a simple solution combustion method (SCM) in order to meet most of the above important criteria. For the first time we have studied the effect of incorporation of vanadium ions in the titania ($Ti_{1-x}V_xO_2$) lattice, along with disordered mesoporosity for the ODH of EB at temperature ≤ 530°C with O_2 as oxidant. Prepared catalysts were analyzed by various physico-chemical methods and structure–activity relationship has been deduced.

5.2. Results and Discussion

5.2.1. PXRD

PXRD measurements were carried out in order to explore the structural features of the vanadium incorporated mesoporous titania $Ti_{1-x}V_xO_2$ (TVx) materials. In TVx, x stands for nominal V atom %, which is higher than the actual V-content due to the evaporation loss of some V during solution combustion synthesis. Figure 5.1 shows XRD pattern of as prepared TVx materials from low angle to wide angle. All TVx materials were prepared with 1:1 urea to oxidizer ratio. PXRD pattern of TVx materials could be indexed to anatase phase of titania with small amount of rutile phase (JCPDS file 21-1272, 21-1276).

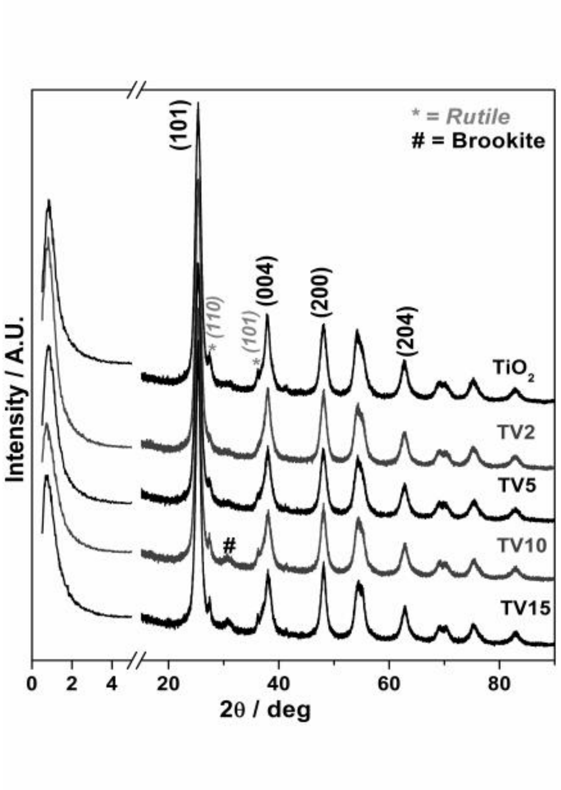

Figure 5.1. Low and wide angle XRD pattern of $Ti_{1-x}V_xO_2$ (TVx) materials.

It is clearly observed that the rutile content increases from 6% for TiO_2 with increasing V-content to 11% for TV15. It is well known that vanadium ion incorporation enhances the formation of thermodynamically stable rutile phase.[11,12] Very small amount of brookite phase is also observed with high V-content (≥10%). However, there is no vanadium oxide peak observed even at 15% of vanadium loading. This observation hints that vanadium ions are likely to occupy the lattice position of titania. Although no VO_x, particularly V_2O_5, has been observed in PXRD, it cannot be ruled out a highly dispersed vanadium oxide on titania.[13] Nonetheless, it is to be noted that Feng et al [14] observed V_2O_5 phase even at 7% loading itself. No V_2O_5 formation in TVx indicates the potential of SCM method to introduce V into the lattice. A broad peak confirms the formation of nanosize crystalline particles. Crystallite size was calculated by using Debye-Scherrer equation and shown in Table 5.1. There is no peak shift observed after vanadium incorporation in TiO_2. However broad XRD features, due to nanocrystallite size, does not show any shift due to V-introduction in the TiO_2 lattice.

In Figure 5.1, a single diffraction peak is observed around 0.8° demonstrates the mesoporous nature of the $Ti_{1-x}V_xO_2$ materials. Unlike ordered mesoporous materials, such as, SBA-15 and MCM-48, all TVx materials exhibit only one peak around 0.8° without any extra peaks. [15,16] This highlights the presence of disordered mesoporosity [17,18] for all TVx materials. Increasing V-content affects the mesoporosity of the materials. An increase in surface area and pore volume (Table 5.1) to be noted up to V = 10% compared to TiO_2 and then a marginal decrease in surface area is observed for TV15. Nonetheless, it is clear that all TVx materials exhibit mesoporosity along with high crystallinity.

Table 5.1. Physicochemical properties of $Ti_{1-x}V_xO_2$ catalysts

Catalyst	Bulk V-content	BET surface area (m^2/g)	Pore size (nm)	Pore volume (cc/g)	Crystallite size (nm)
TiO_2	0.0	160	3.9	0.18	15.3
TV5	4.9	195	4.7	0.25	12.9
TV10	6.9	210	4.9	0.26	9.8
TV15	10.5	140	5.6	0.20	10.3

5.2.2. Energy dispersive X-ray (EDX) analysis

Energy dispersive X-ray (EDX) analysis has been carried out to measure the material composition as well as to find out the extent of homogeneity of the material. Representative results are given in Figure 5.2 for TV5 (a and b), and TV10 (c and d) materials. Elemental mapping have been carried out and shown with colour coding for different elements. High intense and low intense (or diffused) color indicates the high and low content of corresponding elements, respectively, in a particular area/spot. Figure 5.2b and d shows the vanadium and titanium mapping of the above materials to show the homogeneous distribution over a large area (5.2 mm^2). A glance at TV5 (Figure 5.2a) and TV10 (Figure 5.2c) highlights an increase in V composition from the former to the latter. An increase in V content on TV10 compared to TV5 is evident from Figure 2. The above results confirm the homogeneous distribution of, particularly vanadium, at the microscopic level, indicating the effectiveness of the preparation method. Bulk atom % values reported in Table 1 are the average values obtained over large area of >500 μm^2.

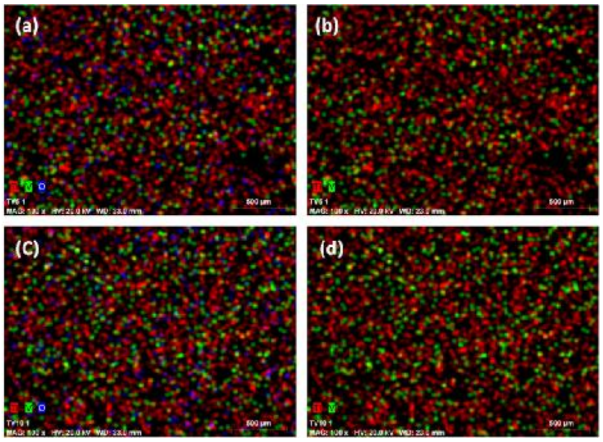

Figure 5.2. Elemental mapping of (a and b) TV5 (c and d) TV10 (Ti – Red, V – Green, O – Blue) measured by EDX over an area of 2x2.6 mm^2.

5.2.3. N_2 adsorption isotherm

N_2 adsorption-desorption studies has been measured to investigate the textural properties of the $Ti_{1-x}V_xO_2$ materials. Figure 5.3 shows N_2 adsorption-desorption results and Barret-Joyner-Halenda (BJH) pore size distribution of TVx materials.

Figure 5.3. (a) N_2 adsorption-desorption isotherms, and (b) BJH pore-size distribution of TVx materials.

All materials show type IV adsorption-desorption isotherm with H_2 hysteresis loop which is typical for all mesoporous materials. [19,20] All TVx and TiO_2 materials show narrow pore size distribution. BET surface area of all materials were calculated and shown in Table 5.1. Surface area increases as the V-content increases, and TV10 shows the highest surface area (210 m^2/g). It is interesting to note that an increase in the V-content significantly increases the extent of mesoporosity, surface area and the pore volume. This is attributed to a decrease in crystallite size from 15 nm for TiO_2 to 10 nm for TV10 and TV15. This observation is in agreement with low angle XRD data. Unimodel pore size distribution is observed with an average pore diameter around 4.7 ± 1 nm for all TVx materials.

5.2.4. TEM

Particle morphology and textural properties of TVx catalysts has been studied by HRTEM carefully. Representative high resolution transmission electron microscope

(HRTEM) images recorded for TiO_2, TV5 and TV10 materials are shown in Figure 5.4. Generally TVx exhibits spherical particles and the size of the particles also decreases with increasing V-content. A wormhole like mesoporous structure can be seen for TVx materials. This disordered mesoporosity arises due to intergrowth of fundamental particles and the same leads to aggregates with significant extra framework void space. [17,18,21]

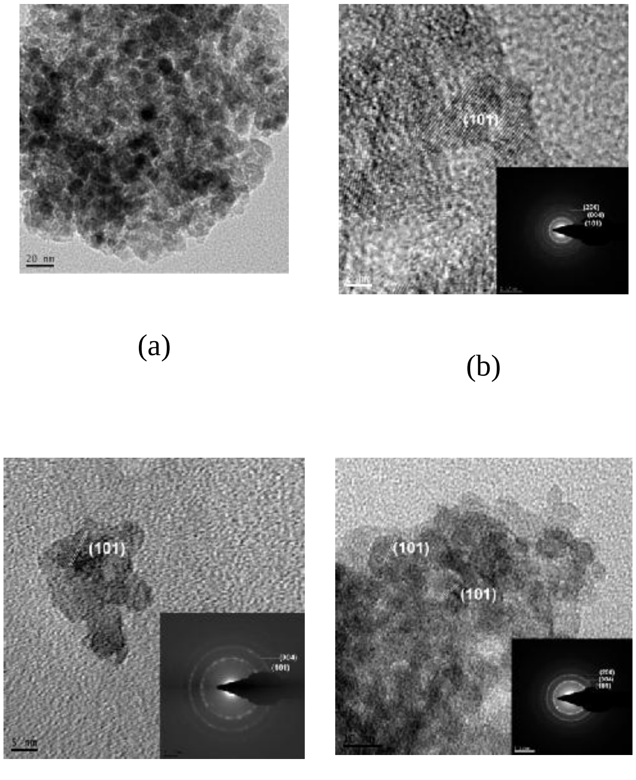

(a) (b)

(c) (d)

Figure 5.4. TEM image of (a and b) TiO_2 (c) TV5 and (d) TV10. Similar image as that of given in panel (a) is observed for all TVx materials.

Selected-area electron diffraction (SAED) pattern confirms the crystalline nature of the nanocrystalline TVx materials and also it shows the anatase phase in both materials. HRTEM image shows the majority of lattice fringes corresponding to (101) (d(101) =

0.352 nm) crystallographic planes of anatase phase. These observations are in excellent agreement with XRD as well as with N_2 adsorption isotherm results. Similar types of images are already observed by Yu et al for disordered type phosphated mesoporous titania prepared using co-block polymers as a template. [22] The disorderd mesoporous nature has additional advantages like low diffusional barriers, since the depth or length of mesopores are minimum to a few nanometers, unlike several hundred nanometers in conventional ordered mesoporous materials, like SBA-15. These types of mesopores are known as p3D mesopores. [21] This disordered p3D wormhole like framework provides an easy route for the diffusion of reactants due to less diffusion barriers.

5.2.5. Raman and FT-IR spectroscopy

Raman spectroscopy is a versatile tool to determine the structural features of the oxide materials. Figure 5.5a shows Raman spectra of all TVx materials. In the case of pure titania, all six Raman active fundamental modes are observed at 145 (E_g), 198 (E_g), 398 (B_{1g}), 516 (A_{1g} + B_{1g}), 640 (E_g) cm^{-1} for the anatase phase. Broad nature of these peaks confirms the formation of nanosize particles. None of the four Raman active modes (144 (B_{1g}), 446 (E_g), 610 (A_{1g}), 827 (B_{2g}) cm^{-1}) of rutile titania was observed, possibly due to low rutile content as well as very broad nature of the anatase features. Raman spectra for V_2O_5 also included for better comparison. None of the Raman features of V_2O_5 (285, 703, and 997 cm^{-1}) was observed in the Raman spectra underscores the absence of bulk crystalline V_2O_5 phase in mesoporous TVx materials. There is no peak that corresponds to monomeric or polymeric vanadium species has been observed for TVx materials, unlike other impregnated catalysts. [23, 13] Importantly, the intensity of all the peaks decreased drastically (up to two orders of magnitude) with increasing V-content. XRD and TEM analysis reveals that the crystallinity as well as morphology, respectively, of the bare TiO_2 as well as $Ti_{1-x}V_xO_2$ remains the same. Therefore this decrease in the peak intensity is mainly due to the symmetry breaking of TiO_2 lattice due to the incorporation of vanadium. [24] This symmetry breaking could occur only if vanadium was incorporated into the titania lattice. This observation also rules out the homogeneous distribution of vanadium oxide on titania. No V_2O_5 features observed for TVx with $x \geq 5$ supports the above conclusion. These results are in well agreement with the literature report. [13,24]

Figure 5.5b shows the FT-IR spectra for pure titania and TVx materials and compared to V_2O_5. Pure TiO_2 shows broad band in the region of 400-900 cm^{-1} due to unresolved stretching vibrations of Ti-O-Ti.

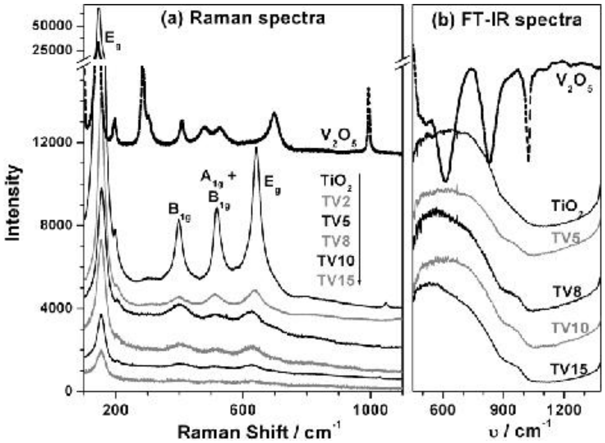

Figure 5.5. (a) Raman, and (b) FT-IR spectra of TVx materials. V_2O_5 spectral data given for comparison. None of the V_2O_5 features are observed in TVx materials highlighting the absence of V_2O_5 and suggesting the introduction of V into the titania framework.

Bulk V_2O_5 displays well resolved stretching and bending vibrations of V=O at 1025 and 831 cm^{-1}, respectively. However, there are no V_2O_5 features observed even with TV15. This confirms the absence of separate V_2O_5 phase in all TVx materials. Along with XRD and Raman spectroscopy, FT-IR also supports the lattice incorporation of vanadium in titania. Moreover there is no direct evidence observed for the dispersion of vanadia on anatase titania which strongly proves that vanadium is incorporated into titania lattice.

TVx material reported in this thesis is different from conventional impregnated catalysts.

5.2.6. X-ray photoelectron spectroscopy

Figure 5.6 shows XPS spectra of (a) Ti 2p, and (b) V 2p and O 1s core level spectra of TVx materials. Ti $2p_{3/2}$ core level appears at a BE around 459 ± 0.2 eV for all TVx materials. This is in good agreement with the BE reported for Ti^{4+} in literature reports. [25] Indeed Ti $2p_{3/2}$ BE increases gradually from 458.8 eV for TiO_2 to 459.2 eV for TV15. V $2p_{3/2}$ core level is observed around 517±0.1 eV for all TVx materials, indicating the oxidation state of V to be 5+. Indeed this observation suggests that the charge compensation requires extra oxygen to be present in the lattice. We do not want to rule out the presence of extra oxygen in the lattice. However, it is to be noted that the isolated V^{5+} reported on supported system, such as V/Al_2O_3, displays a BE of 517.5 ± 0.2 eV for V $2p_{3/2}$ core level and bulk V_2O_5 shows the same at 517 eV. However, V^{5+} in TiO_2 crystal lattice is bound to behave considerably

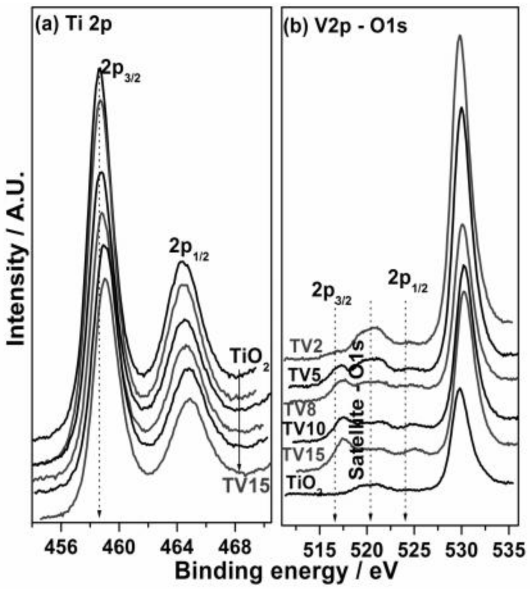

Figure 5.6. X-ray photoelectron spectra of (a) Ti 2p (b) V 2p and O 1s core levels of TVx materials. A shift in BE with increasing V-content suggests a charge redistribution in the titania lattice framework.

different, due to charge redistribution within the lattice. In this sense, the BE observed for V $2p_{3/2}$ core level for TVx materials at 517 eV should be considered as that of an oxidation state between 4+ and 5+. Indeed a significant increase in Ti $2p_{3/2}$ BE with increasing V-content suggests a decrease in electron density on Ti, which is attributed to the above charge distribution within the lattice. O 1s core level BE increases from 529.8 eV for TiO_2 to 530.4 for TV15. A linear increase in BE with incresing V-content, indeed, supports that there is a charge redistribution within the lattice system due to V-incorporation in the lattice.

Table 5.2. Surface atom percent of fresh and spent $Ti_{1-x}V_xO_2$ catalysts

Catalyst	Ti in Fresh (spent)[a] catalyst (%)	V in Fresh (spent)[a] catalyst (%)	O in Fresh (spent)[a] catalyst (%)	V/Ti ratio Fresh (spent)
TV2	26 (15.9)	0.3 (3.6)	72.5 (47.9)	0.01 (0.23)
TV5	25.2 (10.8)	0.9 (3.7)	72.1 (47)	0.04 (0.34)
TV8	24.4 (10.3)	2.9 (4.4)	71.1 (50.1)	0.12 (0.43)
TV10	22.8 (12.6)	3.5 (5.5)	70.9 (55.7)	0.15 (0.44)
TV15	22.1 (10.8)	4.7 (6.1)	71.7 (55)	0.21 (0.56)
TiO_2	26.2 (19.2)	-	72.4 (55)	-

[a] Carbon percentage on spent catalyst is 100 – (Ti% + V% + O%); spent catalyst was recovered after 12 h of reaction at 500°C.

Surface atom percentage calculated from XPS results, are shown in Table 5.2. Although V-content on the surface increases with increasing nominal V-concentration, it is lower than the input V amount. This is, in part, attributed to the loss of V in the combustion synthesis. Introduction of V into the bulk of titania crystal lattice, as observed in XRD, Raman analysis and EDX, suggests a large amount of V should be available in the bulk. This is further supported by a relatively smaller decrease in surface Ti- content. It is also to be noted that the surface oxygen percentage varied little with increasing V-content.

5.3. Catalytic activity

5.3.1. Effect of EB flow and oxygen flow

EB to styrene ODH reaction with oxygen has been used as a probe reaction to explore the catalytic activity of the prepared TVx materials. This is primarily to explore the influence of V^{5+} introduced in TiO_2 lattice framework. Environmentally benign O_2 is used as an oxidant. [26] However caution must be exercised due to the exothermic nature of the reaction with combustible reactant and products in the presence of oxygen. Reactions were carried out at relatively low temperature, compared to conventional endothermic reaction, and at atmospheric pressure. Feed (EB) and O_2 flow variation

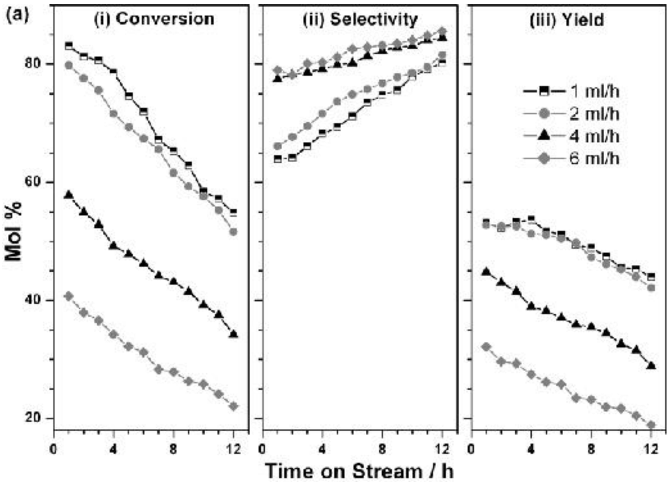

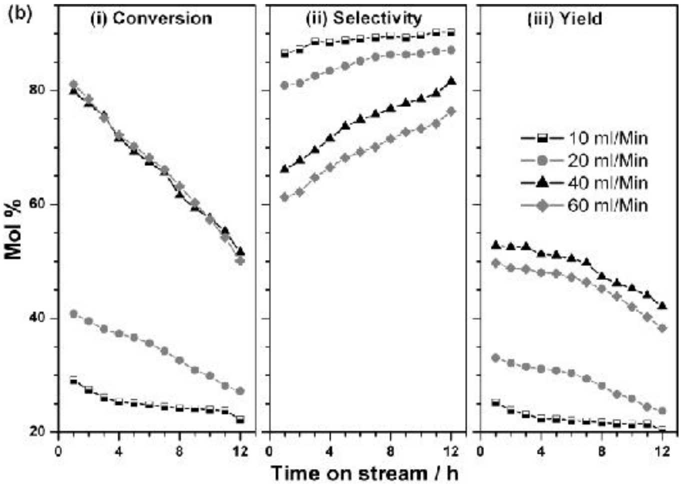

Figure 5.7. Catalytic activity dependence of (a) EB flow at a fixed O_2 flow of 40 ml/Min, and (b) O_2 flow at a fixed EB flow of 2 ml/h with TV10 catalyst at 500°C. Reasonably stable yield is observed due to the opposite changes observed with conversion and selectivity.

measurements was carried out separately in order to optimize the reaction conditions to get the maximum styrene yield. Figure 5.7a and 5.7b shows feed as well as O_2 flow variation, respectively, with TV10 catalyst at 500°C. O_2 flow was fixed at 40 ml/min for all EB flow variation measurements, and EB flow was fixed at 2 ml/h for all O_2 flow variation measurements. Maximum conversion and yield was observed with very low EB flow, such as 1 ml and 2 ml/h. Conversion decreases with increasing EB flow rate due to reduction in contact time between the reactant and active sites which in turn results in lower yield. Lower EB flow leads to somewhat lower selectivity. It may be due to the decomposition of some amount of styrene due to longer contact time. Based on these observations, 2 ml/h EB flow is kept as an optimum flow rate to attain the maximum styrene yield for further studies.

EB conversion and styrene yield increases with increasing O_2 flow from 10 to 40 ml/min (Fig. 5.7b). However, on further increase in O_2 flow (60 ml/min), selectivity and yield decreases although conversion remains high. Optimum styrene selectivity is observed with 40 ml/min O_2 flow. Higher than 40 ml/min flow leads to some decomposition of styrene and hence styrene selectivity is reduced. Interestingly, coke deposition is very minimum at 40ml/min O_2 flow. This observation was further confirmed by TG/DTA analysis of the spent catalysts which will be discussed in later section. In view of this optimization all further reactions were carried out at 40 ml/min O_2 flow and EB flow of 2 ml/h in order to get the maximum styrene yield.

5.3.2. Effect of Reaction Temperature

Temperature of the reaction is one of the important parameter which affects the selectivity and yield of the desired product. The effect of reaction temperature as a function of time on stream (TOS) on EB conversion and styrene yield is shown in Figure 5.8 with TV10 catalyst. Following points are worth highlighting. (i) EB conversion increases with increasing reaction

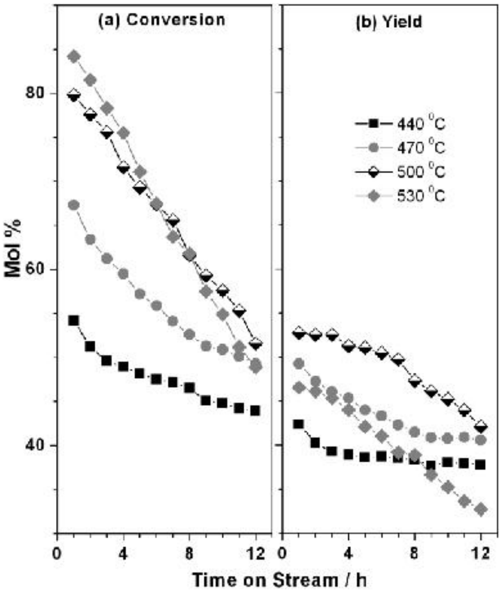

Figure 5.8. (a) Effect of temperature on the conversion and (b) yield of the reaction with TV10 catalyst using 2 ml/hr EB flow and 40 ml/min O_2 flow.

temperature. However, stable conversion is observed up to 470°C, and the conversion decreases fast as the temperature increases as a function of TOS. (ii) Stable styrene yield is observed up to 500°C and the yield also increases from 440 to 500°C. Further increase in temperature, decreases the yield as a function of TOS. (iii) In spite of high EB conversion in the initial hours, a decrease in styrene selectivity at 530°C indicating a possible decomposition of styrene. (iv) The highest styrene yield is observed at 500°C. Therefore 500°C is chosen as an optimum reaction temperature to achieve the maximum yield of styrene. Apart from the above points, relatively stable EB conversion and stable styrene yield at 440 and 470°C is worth noting. At higher time on stream there is an increasing convergence in the value of conversion and stable yield has been observed between 440 and 500°C. It is well known that stable product yield have definite advantages at large scales production, especially at lower temperatures.

5.3.3. Effect of vanadium content and time on stream

Temperature dependent EB conversion and styrene yield with all TVx catalysts at TOS = 5 h is shown in Figure 5.9. This shows a volcano type activity pattern with V-content and the maximum activity has been observed with TV10 catalyst. Pure TiO_2 gives very low styrene yield. EB conversion and styrene yield increases with increasing V incorporation and attains the maximum with TV10 catalyst. Among all TVx catalysts, TV15 gives low yield of styrene.

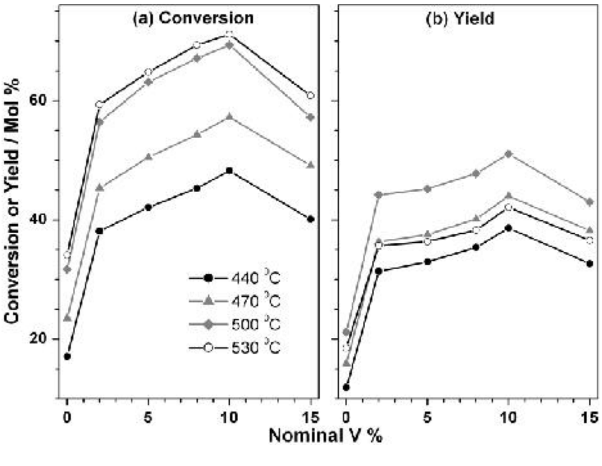

Figure 5.9. Catalytic activity dependence of EB to styrene reaction on nominal V-content at different temperatures. Data collected at TOS = 5 h is given for (a) conversion, and (b) yield. 10% nominal V-containing titania shows the best performance under present experimental conditions.

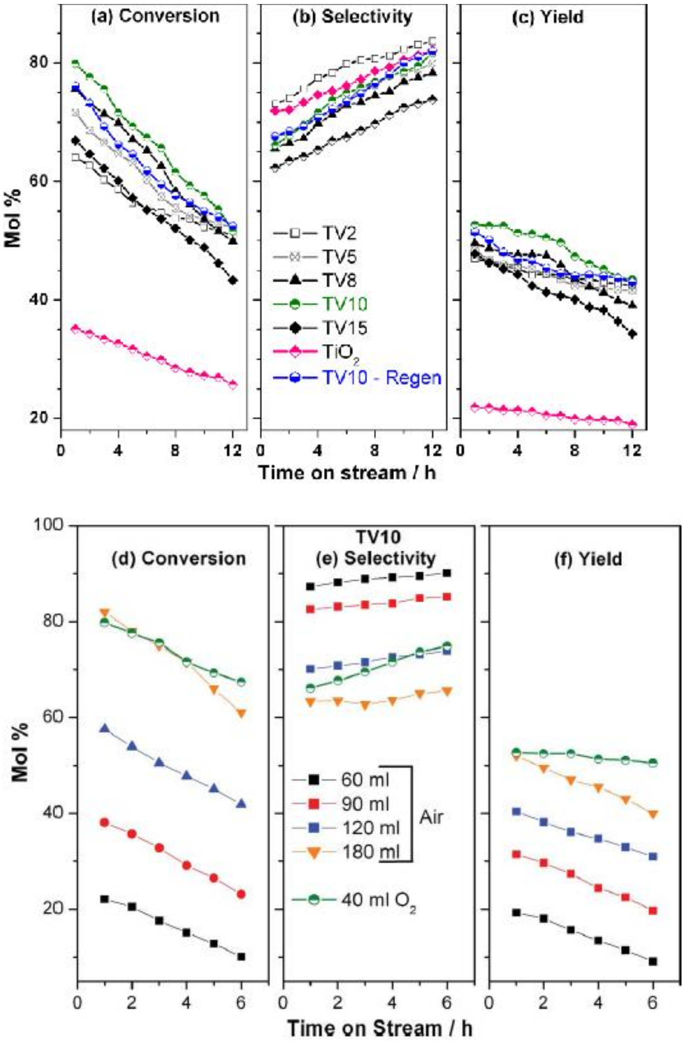

Figure 5.10. Time on stream dependence of catalytic activity of TVx catalysts under optimized conditions (500°C, EB = 2 ml/h and O_2 = 40 ml/h) for (a) conversion of EB, (b) selectivity and (C) yield of styrene. TV10 regenerated (after 4h of reaction) with 20 min. O_2 treatment at 500°C fully recovers and displays the activity that of fresh TV10. A distinct change in catalytic activity observed with TVx compared to pure titania highlights the importance of V for ODH reaction. (d–f) TOS dependence of catalytic activity of TV10

catalyst under optimized conditions (500°C, EB = 2 ml h^{-1}), but in air at different flow rates (60 to 180 ml min^{-1}) and compared with that of O_2 = 40 ml min^{-1}.

Optimum EB flow (2 ml/h), reaction temperature (500°C) and oxygen flow (40 ml/min) was fixed in order to understand the influence of V-content towards the EB to styrene ODH reaction. Figure 5.10 shows the catalytic activity of TVx materials for ODH reaction of EB at 500°C. Pure TiO_2 displays 2-3 times lower conversion and yield than that of any TVx materials, highlighting the necessity of V for the present ODH reaction. However, selectivity is comparable to that of best performing TV2 catalyst. Generally the EB conversion increases with increasing V-content from 2 to 10%, on further increase in V-content leads to a decrease in EB conversion. Irrespective of the V-content, initial high conversion of EB observed keep on decreases linearly with time. In contrast to the above, the styrene selectivity linearly increases with TOS and irrespective of V-content. Hence styrene yield is relatively constant over the reaction time of 12 h. Among all catalysts, TV10 shows higher EB conversion as well as styrene yield. The decrease in EB conversion is more pronounced at high vanadium incorporated (TV15) catalyst. Moreover the surface area of these catalysts reaches the value of around 40 m^2/g within 2 h of reaction. Therefore change in the ODH activity is mainly due to the difference in the V content in $Ti_{1-x}V_xO_2$ catalysts. Apparently at high vanadium concentration, probability of one V^{5+} finding another V^{5+} in the near neighbour environment is high, and chances of polymeric vanadyl type species cannot be ruled out. Hence it is concluded that incoporation of vanadium ions more than 10 % is detrimental to styrene yield. Therefore conversion and yield also decreases with TV15 catalyst. It is observed that the selectivity is more in the case of lower vanadium incorporated catalyst (TV2).

Interestingly, the activity of the catalysts after 12 h on TOS can be regenerated by simply passing oxygen for 20 min at 500°C (Fig. 5.10). Little amount of coke deposited during the reaction can be burnt off by oxygen. Although the total amount of coke deposited is small, it increasingly blocks the active sites on the surface, and hence a reduction in activity. On regeneration the catalyst shows similar trend in conversion and yied, as that of fresh catalyst, confirms the coke deposition is exclusively limited to the surface.

To evaluate the feasibility of the EB to styrene ODH in air atmosphere, above reactions has been repeated under the same conditions with TV10 at different air-flow rates. Results obtained are shown in Fig. 5.10 (d–f). EB conversion and styrene yield increases linearly with increase in air-flow rate from 60 to 180 ml min^{-1}. Indeed increase in the above rate is proportional to the oxygen content in air. However, compared to molecular O_2, a relatively fast decline in conversion and yield in fewer hours of reaction time underscores a relatively fast deposition of coke. Further, selectivity remains around a constant value and it is in contrast to an increasing selectivity in O_2 atm. It is also to be noted that the TOS = 1 h activity is the same for 40 ml min^{-1} of O_2 and 180 ml min^{-1} of air. It is expected that the same activity might be obtained under air or air + O_2 atmosphere as that of pure O_2 by employing fluid catalytic cracking (FCC) reactors and changing the contact time suitably. This would also decrease the hazardous nature of the reaction. However more studies are necessary to confirm the above aspects.

Although the styrene selectivity is high, benzene is one of the significant side product observed along with minor amount of toluene and styrene oxide. No other secondary products were observed. Table 5.3 shows the selectivity of the above side products with TV10 at TOS = 10 h at different temperatures. Decrease in selectivity of styrene and benzene at higher temperatures (530°C) is due to the increasing total oxidation of reactant and products to CO_2.

Table 5.3. Temperature dependence of products selectivity (mol %) with TV10 catalyst

T / °C	Styrene	Benzene	Toluene	Styrene oxide
440	85	12.5	1.5	<1
470	82	11.2	1	<1
500	80	10	1	<1
530	64	8.2	1	<1

[a]Data collected at TOS = 10 h

5.4. Physicochemical analysis of Spent Catalysts and its correlation to activity

XRD, thermogravimetry and differential thermal analysis (TG/DTA), XPS and Raman spectra of the spent catalysts have been recorded in order to explore the structure activity relationship. Catalysts that were subjected to optimized reaction conditions for 12 h of reaction at 500°C have been analyzed for the above study, unless otherwise specified. Figure 5.11a shows the XRD for the spent catalysts along with fresh TiO_2. All of the spent catalysts were completely converted into the rutile phase. Even after 1 to 2 h of reaction also the catalysts shows > 90 % of the rutile phase (Fig. 5.11a). This underscores the total phase change of TiO_2 to rutile occurs at the beginning of the reaction within first 2 h. However, this anatase to rutile phase conversion does not affect the activity of the catalysts.

Commonly active phase will get segregate out under these reaction conditions. However, there is no peak observed for V_2O_5 phase even with TV15 after this highly exothermic reaction conditions. This observation strongly supports the incorporation of active V species into titania lattice. Hence these $Ti_{1-x}V_xO_2$ catalysts are highly recyclable. A simple calcination of fresh catalysts at 500°C for 5 h leads to about 15% rutile, indicating the accelerated anatase to rutile phase conversion is due to the exothermic nature of the reaction. In fact rutile phase conversion is observed with reaction carried out even at 440°C underscores the phase conversion is due to the exothermic nature of the reaction.

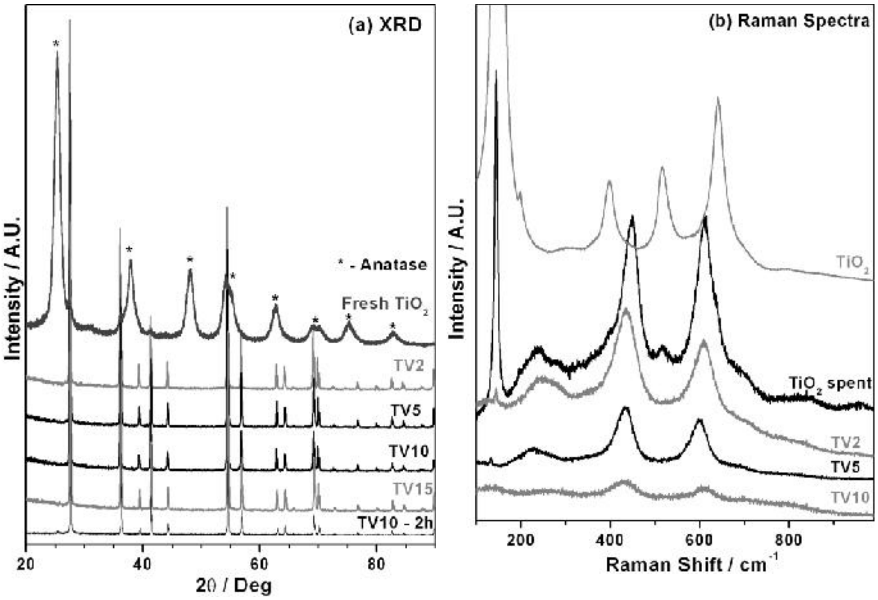

Figure 5.11. (a) Powder XRD patterns, and (b) Raman spectra of spent TVx catalysts after 12 h of reaction at 500°C. Fresh TiO_2 catalyst spectrum is given for comparison purposes.

Mesoporosity of TVx materials was analyzed by low angle XRD and N_2 adsoption-desorption studies of spent catalyst. Mesoporosity is completely lost after the reaction. It is mainly attributed to the exothermic nature of the ODH reaction. Surface area also significantly reduced with the spent catalyst. After reaction for 12 h, all TVx catalysts exhibits a low surface area between 35 to 40 m^2/g. Compared to anatase, formation of highly dense rutile phase is the main cause [27] for the loss of mesoporosity as well as reduction in surface area. Interestingly, from the reaction point of view, it is to be stated that the above changes seems to be essential for stable styrene yield at reaction temperature between 440 and 500°C. In other words, reactivity is retained at the cost of textural properties, such as high surface area, pore volume, mesoporosity and rutile phase change.

Figure 5.11b shows the Raman spectra of the spent catalysts along with fresh TiO_2.

Raman features of anatase phase fully disappears and the new features that appear correspond to that of rutile phase. [15] Raman spectra confirm the phase transformation of TiO_2 from anatase to rutile due to the reaction. None of the Raman features of vanadium oxide (Fig. 5.5a) is observed for the spent catalysts strongly emphasize that there is no segregation of active phase due to the reaction. Hence there is no significant decrease in the styrene yield with TVx catalysts. This conclusion emphasizes the efficacy of the SCM procedure, which effectively incorporates active vanadium into the support TiO_2 lattice and prevents any agglomeration and segregation due to the exothermic reaction.

XPS spectra were recorded for the spent catalysts, and the results are shown in Figure 5.12. XPS results of TV10 (fresh) catalyst is also plotted for comparison. A comparison of BE of Ti 2p, V 2p and O 1s core levels of fresh TV10 catalyst to that of spent TVx catalysts reveals a decrease in BE of all of the core level features. However, the extent of variation changes for all three elements. BE of Ti $2p_{3/2}$, V $2p_{3/2}$ and O 1s core level decreased by 0.8, 0.6 and 0.5 eV, respectively, compared to fresh TV10 catalyst. In addition there is a significant change in intensity of all three core levels observed, as seen in Fig 5.12. A glance at the spectra in Fig. 5.12 suggests a marked decrease in the intensity of O and Ti after the reaction; however the intensity of V apparently looks similar for fresh and spent catalysts. To explore more on the surface composition surface atom percentage was calculated from XPS results and the photo ionization cross section of different element core levels, [28] and the results are given in Table 5.2. It is worth highlighting the following three important observations: (1) A sizeable decrease in Ti and O atom % on the surface at the cost of soft coke which is characterized by graphitic carbon around 284 eV. (2) A significant increase in the

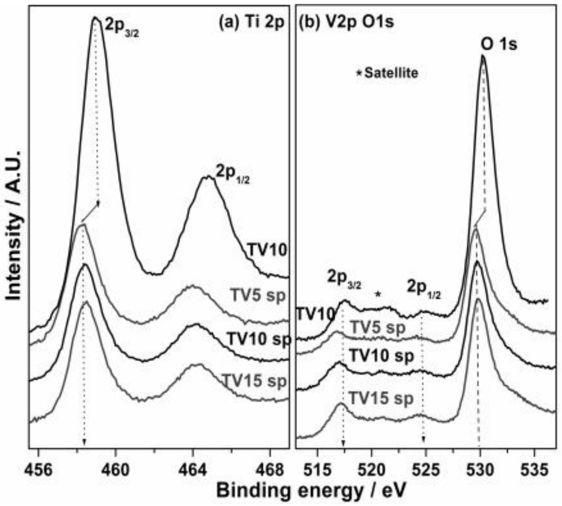

Figure 5.12. X-ray photoelectron spectra of (a) Ti 2p (b) V 2p and O 1s core levels of spent TVx materials. A shift towards lower BE with increasing V-content is observed with all core levels suggesting a change in the electronic structure of TVx due to phase change from anatase to rutile.

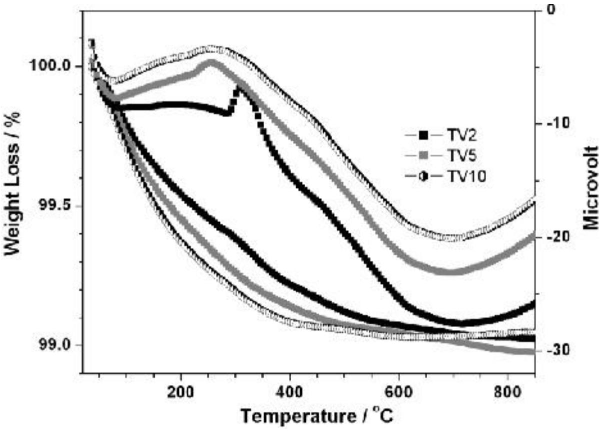

Figure 5.13. TG-DTA spectra of spent catalysts (after 12 h reaction at 500°C).

surface V % is observed for all spent TVx catalysts, compared to fresh TVx materials. However the percent increase in surface V-content after the reaction is much higher for TV2 and TV5 than the other compositions (TV8- TV15). (3) Even with TV10 and TV15, the surface V content does not exceed 6 atom % highlighting that the vanadium is ionically distributed and not agglomerated. Indeed no V_2O_5 phase has been observed in

XRD and Raman spectra of spent catalysts supports this conclusion. Resumption of original catalytic activity after regeneration by burning coke demonstrates the integrity of catalyst and without V_2O_5 segregation. (4) A decrease in BE of all the core level features suggest a change in the electronic structure of the TVx materials, and it is attributed to the phase change to rutile.

Thermal analysis (TG-DTA) results of spent catalysts are shown in Figure 5.13. All the spent catalysts hardly show a weight loss of around 1%. Surface coke content measured from XPS results varied between 19% for spent TiO_2 to 38% for spent TV5. It is also to be noted that higher V-containing spent catalysts (TV10 and TV15) shows a surface coke content between 26 and 28%. Very small amount of weight loss observed in TG-DTA of spent catalysts highlights the deposition of coke is likely to be exclusively on the surface. Indeed a simple calcination in air for just 20 min. at 500°C removes all coke and original activity is restored, supports the above conclusion. Also a minimum coke percentage observed in Fig 5.13 is mainly due to an optimum flow of oxygen throughout the reaction which prevents bulk coke formation. This is in contrast to most of the earlier reports that reports a high coke deposition on the V-based catalysts. [29,30]

5.5. Conclusion

Vanadium incorporated wormhole mesoporous nanocrytalline titania catalysts were prepared by simple solution combustion method. Incorporation of vanadium ions in the titania lattice framework was confirmed by XRD, Raman, FT-IR and XPS techniques. ODH of EB to styrene was carried out with molecular oxygen at relatively low temperatures ($\leq 530^{\circ}C$) to evaluate the catalytic activity of the TVx catalysts. Compared to pure TiO_2, all TVx catalysts shows 2-3 times higher catalytic activity demonstrates the importance of V for ODH reaction. Among the TVx catalysts, 10% nominal vanadium incorporated titania shows the stable yield towards styrene. Side products selectivity decreases enormously with increasing time on stream toward total styrene selectivity. A simple regeneration of the spent catalysts by heating in oxygen for 20 min restores the original activity. After 12 h reaction also there is no formation of V_2O_5 phase in any of the TVx catalysts. Due to the exothermic nature of the reaction, anatase phase titania converts completely to rutile phase within 2 h of reaction, and it is the rutile phase responsible for the stable yield due to its stability under exothermic conditions. Vanadium ion incorporation beyond 10 % leads to a decrease in EB conversion and styrene yield, due to a possible increase in near neighbour V-V interaction that leads to more total oxidation. Comparable catalytic activity has been observed in air atmosphere indicates the possibility of enhancing the green chemistry and green engineering aspect of the reaction, by employing FCC reactor. It is to be underscored the reactivity is retained at the cost of textural properties and phase change to rutile which is essential for the reaction. However the present set of TVx catalysts should be explored for other ODH and oxidation reactions at relatively lower temperatures, so that textural properties also could be retained for even better catalytic activity.

It is to be underscored the reactivity is retained at the cost of textural properties and phase change to rutile which is essential for the reaction. Some of the 24 principles of green chemistry and green engineering has been adopted in the present work, such as catalyst preparation by simple method in a short time, recyclability of catalyst, reaction temperature is relatively decreased (compared to the commercial process) and successful incorporation of ionic vanadium in the titania lattice framework to avoid agglomeration and hence unwanted secondary reactions.

5.6. References:

1. J. Liu, Y. Fu, Q. Sun, J. Shen, Microporous and Mesoporous Materials **116** (2008) 614.
2. G.Y. Popova, T.V. Andrushkevich, E.V. Semionova, Y.A. Chesalov, L.S. Dovlitova, V.A. Rogov, V.N. Parmon, *J Mol Catal A-Chem.*, **283** (2008) 146.

3. A. Dinse, B. Frank, C. Hess, D. Habel, R. Schomäcker, *J Mol Catal A-Chem* **289** (2008) 28.
4. H. Zhao, S. Bennici, J. Shen, A. Auroux, *Appl. Catal. A:Gen.*, **356** (2009) 121.
5. M. D. Argyle, K. Chen, A. T. Bell, E. Iglesia, *J. Phys. Chem. B.*, **106** (2002) 5421.
6. P. Mars, D.W.van Krevelen, *Chem. Eng. Sci. (Special Suppl.)* **3** (1954) 41.
7. M. P. Woods, B. Mirkelamoglu, U. S. Ozkan, *J. Phys. Chem. C* **113** (2009) 10112.
8. N. Mimura, I. Takahara, M. Saito, Y. Sasaki, K. Murata, *Catal. Lett.* **78** (2002).
9. B. M. Reddy, P. Lakshmanan, S.Loridant, Y. Yamada, T. Kobayashi, C. L.Cartes, T. C. Rojas, A. Fernández *J. Phys. Chem. B* **110** (2006) 9140.
10. T. Blasco, J.M. López Nieto, *Appl. Catal. A:Gen.***157** (1997) 117.
11. J. Choi, C. B. Shin, T. J. Park, D. J. Suh. *Appl. Catal. A:Gen.*, **311** (2006) 105.
12. S. Djerad, L. Tifouti, M. Crocoll, W. Weisweiler. *J. Mol. Catal. A: Chem.*, **208** (2004) 257.
13. K. Bhattacharyya, S. Varma, A. K. Tripathi, S. R. Bharadwaj, A. K. Tyagi, *J. Phys. Chem. C* **112 (**2008) 19102.
14. W. Li, X. Li, J. Feng, *Catal. Lett*. **130** (2009) 575.
15. S. Basu, M. Mapa, C. S. Gopinath, M. Doble, S. Bhaduri, G.K. Lahiri, *J. Catal.* **239** (2006) 154.
16. N. Maity, P. R. Rajamohanan, S. Ganapathy, C. S. Gopinath, S. Bhaduri, G. K. Lahiri, *J. Phys. Chem. C* **112** (2008) 9428.
17. S.S. Kim, T. R Pauly, T. Pinnavaia, *Chem. Commun*. (2000) 835.
18. Z. Zhang, T. Pinnavaia, *J. Am. Chem. Soc.* **124** (2002) 12294.
19. K.S.W. Singh, *Pure Appl. Chem.*, **57** (1985) 603.
20. D. G. Kulkarni, A. V. Murugan, A. K. Viswanath, C. S. Gopinath, *J. Nanosci. Nanotech.*, **9** (2009) 371.

21. K. Sivaranjani, C. S. Gopinath *J. Mater. Chem*. **21** (2011) 2639.

22. J. C. Yu, L. Zhang, Z. Zheng, J. Zhao, *Chem.Mater*. **15** (2003) 2280.

23. A. Christodoulakis, M. Machli, A. A. Lemonidou, S. Boghosian, *J. Catal.* **222** *(*2004) 293.

24. R. S. Zeferino, M. B. Flores, U. Pal, *J. Appl. Phys*. **109** (2011) 014308.

25. M. Sathish, B. Viswanathan, R. P. Viswanath, C. S. Gopinath, *Chem. Mater*. **17** (2005) 6349.

26. M.P. Woods, B. Miekelamoglu, U.S. Ozkan, *J. Phys. Chem. C* **113** (2009) 10112.

27. D. A. Bulushev, L. Kiwi Minsker, V. I. Zaikovskii, O. B. Lapina, A. A. Ivanov, S. I. Reshetnikov, A. Renken, *Appl. Catal. A:Gen*. **202** (2000) 243.

28. C.S. Gopinath, T. Raja, *J. Phys. Chem. B* **105** (2001) 12427.

29. U.G. Nielsen, N.-Y. Topsoe, M. Brorson, J. Skibsted, H.J. Jakobsen, *J. Am. Chem. Soc*. **126** (2004) 4926.

30. B. M. Reddy, K. N. Rao, G. K. Reddy, P. Bharali, *J. Mol. Catal. A Chem.* **253** (2006) 44.

Chapter 6

Conclusions and Future Outlook

6. Conclusions and Future Outlook

This chapter summarizes the present thesis work and describes the conclusions and possible future implications drawn based on the work.

Chapter 1 provides a brief introduction about heterogeneous catalysis. It demonstrates the structure, properties and applications of TiO_2 in various fields especially in photocatalysis, photovoltaics and selective oxidation reactions. It gives broad literature knowledge about the tuning of band gap of TiO_2 through cation and anion doping. It also explains the importance of disordered mesoporosity and noble metal loading on the photocatalytic activity of TiO_2 especially in the case of water splitting reactions. Basic principles of dye sensitized solar cells and its significance is discussed elaborately. Also this chapter describes the role of isolated V sites on the selective oxidation reactions especially in oxidative dehydrogenation of ethylbenzene.

Simple SCM has been employed to prepare hetero atom (N or V) incorporated disordered mesoporous TiO_2 and nano Au/$TiO_{2-x}N_x$ composites. **Chapter 2** mainly addresses the detailed procedures involved in the materials preparation methods. We employed urea as fuel, to avoid any carbon impurities. During combustion process, in situ generation of NH_3 occurs due to urea decomposition, and this acts as nitrogen source as well as creates a reduction atmosphere. Nascent nano Ti_xO_y clusters ($x/y > 1$) with plenty of defects are very likely to interact vigorously with ammonia to produce $TiO_{2-x}N_x$ materials. Smoldering or voluminous type of combustion occurs depending on the urea/Ti ratio. In this system, smoldering combustion with plenty of gases evolution (NH_3 and CO_2) is a slow process and also the combustion temperature does not increases rapidly which leads to the formation of nanoparticles with disordered mesoporosity. $Ti_{1-x}V_xO_2$ materials were also prepared by SCM method. Incorporation of V in TiO_2 lattice framework has been achieved by this method. Incorporating V in TiO_2 lattice provides isolated V sites which is necessary for selective oxidation reaction. Electronically integrated nano Au clusters with multifunctional, disordered mesoporous $TiO_{2-x}N_x$ (Au-NT) nanocomposites are also prepared by simple one pot SCM method. Theory and experimental procedures involved in various physicochemical and spectroscopic characterization techniques were discussed.

Chapter 3 is divided into two parts **- Part A** and **Part B**. **Part A** deals with detailed studies on structural, spectroscopic and electronic structure of disordered mesoporous $TiO_{2-x}N_x$ materials through various methods. In $TiO_{2-x}N_x$ materials, the structural phase and the extent of mesoporosity mainly depends on urea/Ti ratio. PXRD, N_2 adsorption-desorption isotherm studies and TEM results reveals the presence of disordered mesoporosity in $TiO_{2-x}N_x$ materials. Nanocrystalline anatase phase with high surface area (234 m^2/g), and type-IV H_3-mesoporosity is observed with UT10. Further, the presence of electrically interconnected nanoparticles in UT10 is confirmed by HRTEM. Along with PXRD, Raman spectroscopy also confirms the presence of nanoparticles. The change in electronic property, especially the optical band gap due to nitrogen doping, was clearly observed in UV-vis absorption spectra for $TiO_{2-x}N_x$ materials. XPS indicates the presence of anionic type of nitrogen with O-Ti-N linkages in $TiO_{2-x}N_x$. The impedance measurements of $TiO_{2-x}N_x$ materials were made to explore the resistance at different interfaces in the DSSC assembly. This measurement indicates that there is efficient charge transfer within UT10 material as compared to other UTx materials. Moreover it also suggests a good necking between the individual particles in UT10 confirming EINP, along with TEM. CPP measurement shows that the produced current is significantly higher for UT10 and this is mainly due to the presence of better connectivity between the UT10 nanoparticles. We believe SCM could be extended to different materials of interest, particularly for solar energy harvesting applications, to prepare electrically interconnected particulates with a possible tuning of optical band gap properties.

Part B brings out the applications of $TiO_{2-x}N_x$ materials in various fields. This material shows highest activity towards dye degradation and selective p-anisyl alcohol oxidation reaction under direct sunlight as well as with laboratory light source. Disordered mesoporosity with high surface area, electrically interconnected nanocrystalline particles, N-doping and smaller particle size are the major reasons for higher efficiency. Likely the charge carrier recombination is low with UT10 which gives the best activity. $TiO_{2-x}N_x$ also shows excellent activity towards DSSC. It gives the efficiency of around 7 % with high J_{sc} and V_{oc}. The present study throws light on the importance of textural properties for fast electron transfer and hence higher efficiency of DSSC. More studies in this direction, such as further optimization of textural properties, is likely to increase the efficiency further. It is expected that such electrically interconnected nanocrystalline titania would be potential candidates for water splitting with a noble metal. Further studies are in progress to improve efficiency and catalytic activity through surface modifications by different preparation strategies and adopting light harvesting protocols.

Chapter 4 describes the H_2 generation by visible light driven photocatalysis by electronically integrated nano Au clusters with multifunctional, disordered mesoporous $TiO_{2-x}N_x$ (Au-NT) nanocomposites. All of the prepared materials have been thoroughly characterised. Low angle XRD, N_2 adsorption isotherm and TEM results confirms the mesoporous nature of Au-NT nanocomposite materials. SPR features of nano gold in these composite materials bring more visible light absorption between 500 and 750 nm. Thus more number of visible light photons could be harvested by using xAu-NT nanocomposites. HRTEM images reveal the presence of disordered mesoporosity along with electrically interconnected nanoparticles in all xAu-NT nanocomposites. The intensity of PL emission bands of N-TiO_2 decreases exponentially after introduction of very small amount of gold (0.01 to 0.05 Au-NT). This result indicates the recombination of charge carriers is effectively reduced after Au introduction in N-TiO_2. XPS studies have been carried out in order to know more about the electronic integration aspects of xAu-NT. It confirms the presence of cationic nanogold clusters at surfaces and in pores. Thus a polarized pathway is available for charge separation, especially to store electrons in Au clusters. Photocatalytic WSR was carried out in order to evaluate the efficacy of the above Au-NT nanocomposites under simulated sun light with aqueous methanol solution. Among all, 0.05Au-NT shows the highest H_2 evolution rate than other compositions. 150 µmol H_2/h was generated with 100 mg of 0.05Au-NT. In PEC measurements, compared to titania and $TiO_{2-x}N_x$, xAu-NT displays a four folds increase in photocurrent generation. Systematic studies on PL lifetime measurement would reveal the role of electronic integration in suppressing the defects. Further this highly efficient material can be explored in the field of DSSC, ambient CO oxidation and propene epoxidation reactions.

Chapter 5 addresses oxidative dehydrogenation of ethylbenzene to styrene with vanadium incorporated mesoporous nanocrystalline titania ($Ti_{1-x}V_xO_2$) and molecular oxygen between 440 and 530°C. Incorporation of vanadium ions in the titania lattice framework was confirmed by XRD, Raman, FT-IR and XPS techniques. High ethyl benzene conversion and stable styrene yield has been observed with 10% nominal V-containing rutile phase titania at 500°C. However, stable but relatively lower styrene yield has been observed with 2 and 5% V-containing catalysts between 440 and 500°C. Highest selectivity is observed with lower vanadium content. In order to understand the structure activity relationship, spent catalysts were analyzed by all physico-chemical methods. Although there is a phase change from anatase to rutile $Ti_{1-x}V_xO_2$ within 1 h of reaction, higher activity is primarily attributed to the ionic V^{5+} in $Ti_{1-x}V_xO_2$ lattice, which prevents agglomeration to V_2O_5. It is to be underscored the reactivity is retained at the cost of textural properties and phase change from anatase to rutile, which is essential for the reaction. Indeed, the present set of TVx catalysts should be explored for other ODH and oxidation reactions at relatively lower temperatures, so that textural properties also could be retained for even better catalytic activity.

List of Publications

1. Structure, Electronic Structure, Optical, and Dehydrogenation Catalytic Study of $(Zn_{1-z}In_z)(O_{1-x}N_x)$ Solid Solution.

   Maitri Mapa, **Kumarsrinivasan Sivaranjani**, Deu S. Bhange, Biswajit Saha, Purushottam Chakraborty, Annamraju Kasi Viswanath and Chinnakonda S. Gopinath, *Chemistry of Materials* **22** (2010) 565.

2. Porosity driven photocatalytic activity of wormhole mesoporous $TiO_{2-x}N_x$ in direct sunlight.

   Kumarsrinivasan Sivaranjani and Chinnakonda S. Gopinath, *Journal of Materials Chemistry* **21** (2011) 2639.

3. Molecular oxygen-assisted oxidative dehydrogenation of ethylbenzene to styrene with nanocrystalline $Ti_{1-x}V_xO_2$.

   Kumarsrinivasan Sivaranjani, Akrati Verma and Chinnakonda S. Gopinath, *Green Chemistry* **14** (2012) 461.

4. Toward a Quantitative Correlation between Microstructure and DSSC Efficiency: A Case Study of $TiO_{2-x}N_x$ Nanoparticles in a Disordered Mesoporous Framewok.

   Kumarsrinivasan Sivaranjani, Shruti Agarkar, Satishchandra B. Ogale and Chinnakonda S. Gopinath, *Journal of Physical Chemistry C* **116** (2012) 2581.

5. γ-$Al_{2-x}M_xO_{3\pm y}$ (M = Ti^{4+} through Ga^{3+}): Potential Pseudo-3D Mesoporous Material with Tunable Acidity and Electronic Structure.

   Thomas Mathew, **Kumarsrinivasan Sivaranjani**, Edwin S. Gnanakumar, Yusuke Yamada,Tetsuhiko Kobayashi, and Chinnakonda S. Gopinath, *Journal of Materials Chemistry* **22** (2012) 13484.

6. A simple one pot synthesis of nano gold – mesoporous silica and its oxidation catalysis.

    A. C. Sunilsekhar, **Kumarsrinivasan. Sivaranjani**, Chinnakonda. S. Gopinath and C. P. Vinod, *Catalysis Today* (in press)

7. Disordered mesoporous V/TiO_2 system for ambient oxidation of sulfides to sulfoxides.

    Sanjay Singh Negi, **Kumarsrinivasan Sivaranjani**, Anand Pal Singh and Chinnakonda S Gopinath, *Applied Catalysis A: General* (communicated)

8. Mesoporous $TiO_{2-x}N_x$ + Nano Au: An Electronically Integrated Nanocomposite for Solar H_2 Generation.

    Kumarsrinivasan Sivaranjani, Sivaraman Rajambal, Kanak Roy, Chinnakonda S. Gopinath, *Energy and Environmental Science* (communicated)

<u>Book Chapter</u>

Role of nanomaterials for visible light driven photocatalytic water splitting.

Sivaraman Rajambal, **Kumarsrinivasan Sivaranjani**, and Chinnakonda. S. Gopinath. *John Wiley Publications, Nanotechnology Book Series* (communicated)